IMAGING MAGNETIC ORDER IN MAGNETO-STRUCTURAL PHASES OF Mn_3O_4

BY

XU WANG

DISSERTATION

Submitted in partial fulfillment of the requirements
for the degree of Doctor of Philosophy in Physics
in the Graduate College of the
University of Illinois at Urbana-Champaign, 2012

Urbana, Illinois

Doctoral Committee:

Professor Russell Gianetta, Chair
Associate Professor Raffi Budakian, Director of Research
Associate Professor Brian DeMarco
Professor Philip Phillips

Abstract

Frustration in A-site spinels due to the competition between complex structure and strong interactions has been the focus of many theoretical and experimental studies recently. Mn_3O_4 is one such material with a three way interplay between complex lattice geometry, strong spin-lattice coupling and magnetic interactions. Mn_3O_4 is known to have two distinct phases below the Neel temperature that differ in both structure and magnetic order, including a tetragonal phase with disordered spins, and at lower temperatures, an orthorhombic phase exhibiting long-range commensurate magnetic order. Using a combination of low temperature magnetic force microscopy and electron backscatter diffraction techniques, we explore this magneto-structural phase transition in Mn_3O_4 at 33K. Novel sub-micron magnetic patterns emerge upon transition, and are aligned with specific crystalline axis directions. These magnetic patterns show variations with temperature and magnetic field. We attribute the magnetic patterns observed to strain-mediated phase separation. Phases are separated by a unique wall type, stabilized by the magneto-elastic coupling in Mn_3O_4. This result and the technique developed enable study of similar phase separation behaviors in related strongly correlated materials.

To my family and my fellow graduate students

and

in memoriam: my cat Turtle April 28, 2004—July 11, 2012.

Acknowledgments

This is most likely the least read section of any thesis unless the reader hails from the funding agency (look for bold font paragraph below), so I will try to keep it short and to the point. Special thanks to:

- My advisor, Prof. Raffi Budakian, who made everything possible
- Prof. S. Lance Cooper, for being a fatherly figure as well as going out of the way to help a collaborating grad student.
- Dr. Min-jung Kim, for all the samples used in this thesis
- Tyler Naibert, who is instrumental in the lithography steps involved in the study
- Kurt Wagner of Wagner Machine Co., for his help with making the microscope parts and showing me the awesome machine tools
- Jim Mabon of Center for Microanalysis of Materials, for his help with EBSD and FIB
- Members of the basement gang, i.e. Budakian Lab, Mason Lab and DVH Lab—hey, we lived through this together
- Family and friends for keeping me sane
- My cat Turtle, this one is for you, buddy

This work is supported by the U.S. Department of Energy under Award No. DE-FG02-07ER46453.

Table of Contents

List of Figures

List of Abbreviations

AFM	Atomic Force Microscope, Atomic Force Microscopy
FOFPI	Fiber-Optic Fabry-Perot Interferometer
FPGA	Field Programmable Gate Array
LT-MFM	Low Temperature Magnetic Force Microscope
MFM	Magnetic Force Microscope, Magnetic Force Microscopy
PID	ProportionalIntegralDerivative
PLL	Phase Locked Loop
SFM	Scanning Force Microscope, Scanning Force Microscopy
UHV	Ultra High Vacuum

List of Symbols

B	Detection bandwidth
d	Thickness of a rectangular cantilever
w	Width of a rectangular cantilever
L	Length of the probe
M_S	Sample magnetization
M_T	Tip magnetization
T	Temperature
T_N	Neel temperature
T_i	$i = 1, 2$ Transition temperatures below Neel temperature, numbered in decreasing temperatures
H	Magnetic field
X, Y	Coordinate of the probe tip relative to the sample
x	Position along the cantilever shaft, measured from the base of cantilever
Z	Distance between probe tip, in equilibrium position, and the sample surface
z	Deflection of probe tip
z_{laser}	Deflection of probe at the position where laser is incident
ω	Transducer drive frequency
ω_0	Cantilever resonant frequency (radian)
f	Cantilever resonant frequency
Δf	Frequency shift
k	Cantilever spring constant

k_b	Boltzmann constant
Q	Q factor of the cantilever

Chapter 1

Introduction

1.1 Overview of Strongly Correlated Materials

Strongly correlated materials (SCM) have been a focus of intense study in recent years. In SCM, multiple degrees of freedom, such as spin, charge, lattice and/or orbital, are coupled and simultaneously active [1]. The delicate interplay between coupled interactions result in complex phases of these materials (Fig. 1.1). Competing phases further result in a broad range of interesting phenomena, including notable examples such as colossal magnetoresistance/metal-insulator transitions [2] and high-temperature superconductivity [3]. It has been shown that these phenomena cannot be explained using a single-particle approximation [4, 5] and that many basic properties of various phases are poorly understood [1]. Therefore extensive effort, both experimental and theoretical, have been put into understanding these phenomena as they are scientifically interesting and have great technological potential.

Some SCM behaviors are of particular interest to this thesis. Foremost is the frustration of long range order as the result of competition between interactions, lattice geometry and external perturbations. Long range orders often develop in materials at low temperatures to help lower ground state degeneracy and minimize entropy at T=0K (see, for example, [6] and [7]). However placement of atoms within a lattice and external effects, such as magnetic field and pressure, can frustrate the onset of long range orders even down to T=0K. This makes SCM a desirable specimen for the study of quantum phase transitions, where the quantum phases at T=0K are only accessible by adjusting physical parameters other than temperature (e.g. magnetic field and pressure) [8]. Moreover, various novel low temperature phenomena have been proposed for these frustrated systems and many of them have indeed been observed. Prominent examples are spin liquids [9, 10], spin glasses [11] and spin ice [12] states.

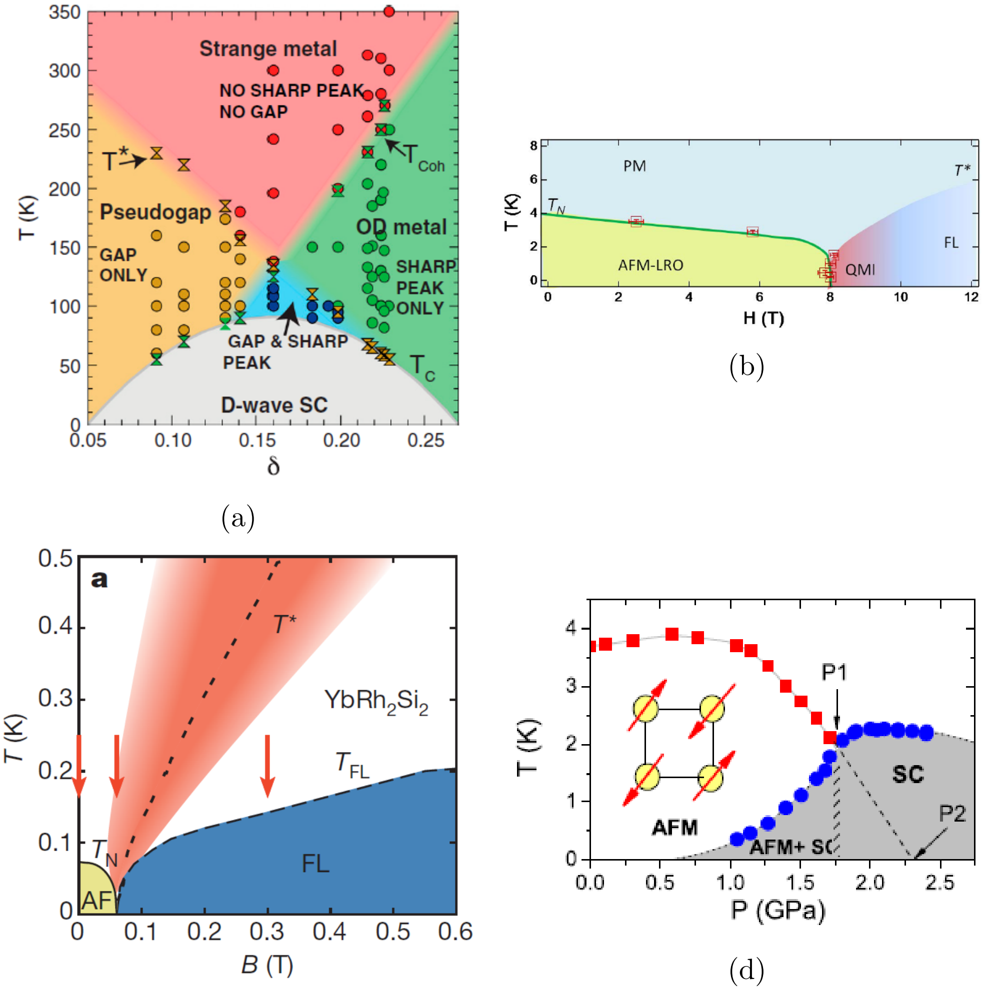

(a)

(b)

(c)

(d)

Figure 1.1: Select phase diagrams of strongly correlated materials: (a): $Bi_2Sr_2CaCu_2O_{8+\delta}$ [13]. (b): $CeCu_2Ge_2$ [14]. (c): $YbRh_2Si_2$ [15]. (d): $CeRhIn_5$ [16].

A few electronic phenomena are associated with long range order (or the frustration thereof): charge order (CO), charge/spin density waves (CDW) and electronic phase separation. Charge ordering and charge/spin density waves are both spontaneous self-organization of charges. Charge ordering is the organization of charges in periodic arrays in a lattice [17], with stripes and checkerboards being common patterns [18] (Fig. 1.2). Charge/spin density waves are a periodic modulation in the density of charges/spins [19].

While charge ordering and charge density waves are considered distinct electronic phases, electronic phase separation involves two or more phases of the SCM, spatially separated but co-existent in said material. (As a higher order effect, in systems where CO or CDW are also present, phase separation occurs at a larger length scale [24, 25].) This behavior is believed to be the result of competition between involved phases, a manifestation of the underlying competition between interactions responsible for these phases. An example of electronic phase separation is the manganese oxide $\mathrm{R}_{1-x}\mathrm{A}_x\mathrm{MnO}_3$, where R is a rare earth and A a divalent ion [25]. A ferromagnetic metallic phase and an anti-ferromagnetic, charge ordered phase coexist in this perovskite due to the competition between double exchange interaction (ferromagnetic phase) and Jahn-Teller interaction (anti-ferromagnetic phase) [25].

On the flip side of competition between interactions, the strong coupling between interactions can lead to a multitude of interesting behaviors as well, such as multiferroic (resulting from ferromagnetic and ferroelectric couplings, [26]), magnetoelastic (spin-orbit coupling and external strain, [27]), magnetodielectric [28] and magnetothermal [29] effects. Many strongly correlated materials have already found their ways into practical applications, with many more proposed applications currently under research. These materials are often transition metal oxides with pyrochlore, perovskite or spinel structures[24, 25, 30].

$\mathrm{Mn}_3\mathrm{O}_4$, or, more precisely, $\mathrm{Mn}^{2+}\mathrm{Mn}_2^{3+}\mathrm{O}_4$ is a binary spinel. Despite its simple composition, $\mathrm{Mn}_3\mathrm{O}_4$ exhibits a rich mix of quantum phases at low temperatures—the result of a three-way interplay between geometric frustration, strong spin-lattice coupling and external magnetic field[32, 33]. $\mathrm{Mn}_3\mathrm{O}_4$ has been found to be magnetodielectric [28, 31], as well as magnetoelastic [33, 31]. The magnetoelastic properties of $\mathrm{Mn}_3\mathrm{O}_4$ is a relatively recent discovery with significant contribution from Dr. Minjung Kim at the University of Illinois at Urbana-Champaign using Raman scattering [32]. Past studies on $\mathrm{Mn}_3\mathrm{O}_4$ utilized bulk magnetic/electric measurements [34], as well as resonance [35], diffraction (X-ray [32, 33] and neutron [36]) and scattering [32, 33] techniques. While much insight has been gained from these studies, little has been learned of the microscopic behavior of this magnetoelastic material due to the absence of experimental studies capable of providing information with the necessary nanometer-scale spatial resolution.

1.2 The Spinel Mn_3O_4

Structurally, Mn_3O_4 has a tetragonal lattice (space group $I41/amd$) at room temperature with lattice constants $a = b = 5.76\mathring{A}$, $c = 9.48\mathring{A}$ [37]. The basic building block of Mn_3O_4 are $Mn^{2+}O_4$ tetrahedra and $Mn^{3+}O_6$ octahedra (Fig. 1.4a). Two other lattice structures are known at other temperatures: cubic above approximately 1417K [38] and orthorhombic below 33K [32].

Mn_3O_4 is a paramagnet down to a Neel temperature of $T_N = 42K$, at which point it becomes a Yafet-Kittel type ferrimagnet [36]. The Mn spin orientations in the ferrimagnetic phase are complex. Overall, the net moment is parallel to [110]. The Mn^{2+} spins align with [110] axis, while Mn^{3+} are pairwise canted in the opposite direction (Fig. 1.4b). The canting angle with respect to $[\bar{1}\bar{1}0]$ varies with site (doubling octahedral sites vs non-doubling octahedral sites) and temperature. All Mn spins lie in the plane normal to $[1\bar{1}0]$ axis, with slight out-of-plane deviations on doubling octahedral sites [36]. The Mn^{3+} at octahedral sites form a corner-sharing network of tetrahedra. Combined with the Mn^{3+} spin coupling, the geometric arrangement produces inherent geometric frustration [39].

The geometric frustration and strong spin-lattice coupling produces further phase transitions below the Neel point [36, 32, 33, 39, 40, 41, 42] . At $T_1 = 39K$, an incommensurate spin structure develops and debate is still ongoing regarding whether the spin structure in this phase is sinusoidal or spiral [42, 41, 33]. The magnetic ordering transitions from incommensurate to commensurate, cell-doubling[1] order at $T_2 = 33K$. X-ray diffraction and Raman

---

[1] The unit cell in the term "cell-doubling" refers to the unit cell defined by tetragonal lattice above T_2.

scattering has found that the transition at T_2 is both magnetic and structural, where γ, the angle between [100] and [010] axis directions, decreases, distorting the tetragonal lattice into a orthorhombic ($Fddd$) lattice [32, 33].

Applying external magnetic field produces fascinating phase diagrams, including the field-induced structural phase changes. When a field is applied parallel to [110] axis, the transition from incommensurate phase to commensurate phase occurs at higher temperature until incommensurate phase is completely suppressed (Fig. 1.5) [32, 33].

Applying the field transverse to the magnetic easy axis produces a more complex phase diagram (Fig. 1.6). Three phases exist below T_1: 1) the commensurate phase with orthorhombic lattice in low temperature and low field. 2) A spin disordered phase with tetragonal lattice in intermediate field. And 3) in high field, a commensurate phase with orthorhombic lattice, but with both magnetic moment and lattice distortion along $[1\bar{1}0]$ (i.e. transverse to the magnetic easy axis in absence of any field) [32, 33]. It is important to note that all these phases in both field directions are both magnetic and structural—commensurate order associated with the orthorhombic lattice, and spin disordered/incommensurate state associated with tetragonal lattice. Kim et al [33] further proved that the transitions between these states can be driven by field, pressure and temperature.

1.3 Magnetic Microscopy of Phase Transistions

As mentioned earlier, microscopic electronic/charge patterns have been observed in SCM due to long range order and coupling of multiple degrees of freedom, as well as due to phase separation (see sec. 1.1). The investigation into the equivalent behavior in frustrated magnetic spinels such as Mn_3O_4 would prove interesting and shed insight into the inner workings of the spin system.

Self-organization of (structural) phases into tunable nanocheckerboard pattern has already been observed in high temperature synthesis of the Mn-doped $CoFe_2O_4$ spinel, which shares similar lattice structure as Mn_3O_4. Further, the high temperature phases of Mn_3O_4 exhibit phase separation behavior between tetragonal and cubic lattice [43]—hinting at possible phase separation at the low temperature structural transition at T_2. Since low temperature phases of Mn_3O_4 are magneto-structural, the structural phase separation would produce a spatial separation of magnetic behaviors, making magnetic imaging the tool of choice for this thesis study.

Magnetic imaging methods commonly employed include magnetic force microscopy [44], scanning quantum interference device (SQUID) studies [45], Lorentz microscopy [46], Hall probe microscopy [47], Kerr microscopy [48] and resonance techniques [49]. Magnetic force microscope (MFM) is arguably most widely used imaging method [50], noted for its simplicity, high resolution, high data throughput and relaxed sample requirement. For the study at hand, MFM is advantageous because of the ease with which it can be used in low temperature implementation.

1.4 Thesis Organization

First we will introduce the technique and instrument of low temperature magnetic force imaging in Chapter 2. Chapter 3 details the preparation procedure of Mn_3O_4 samples as well as the material characterizations at room temperature. Results from magnetic imaging are then presented in Chapters 4.

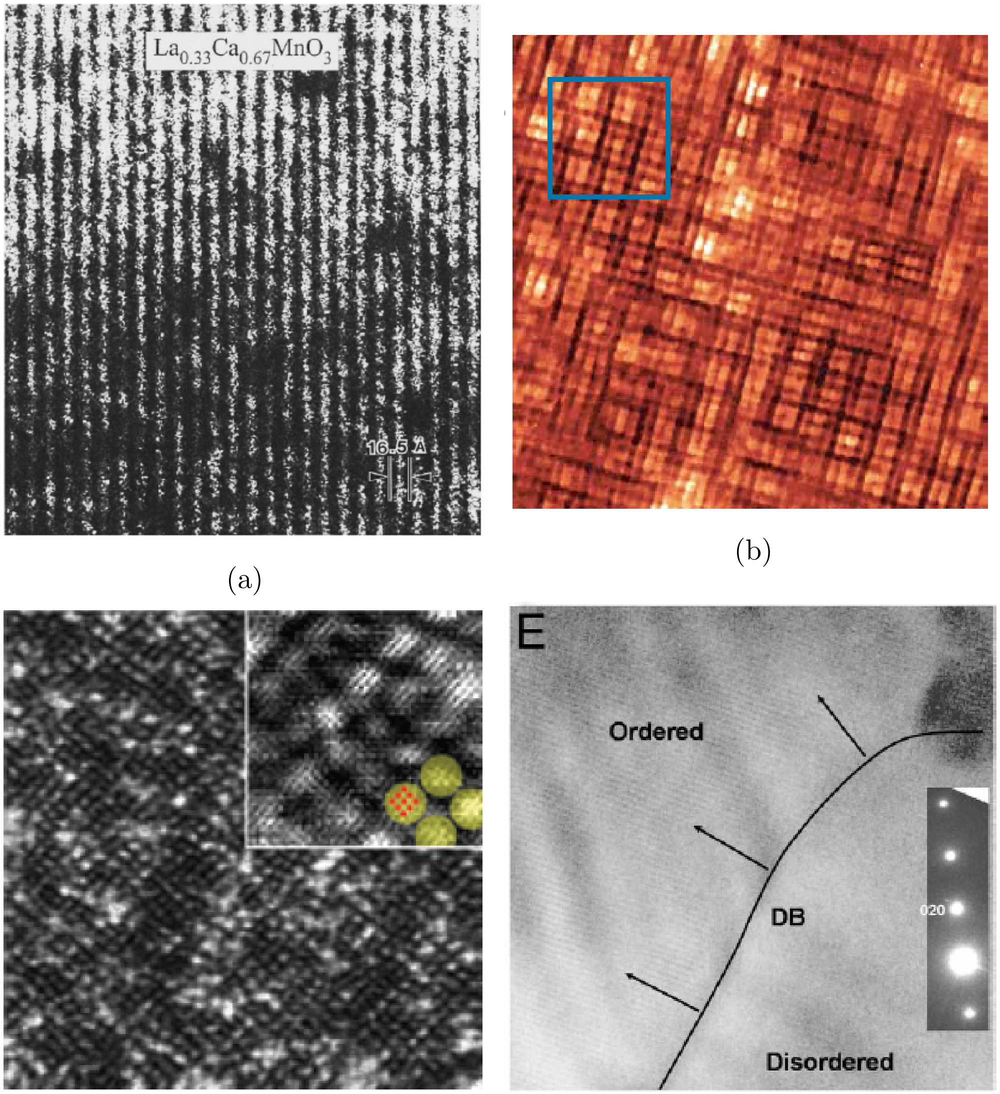

(a) (b) (c) (d)

Figure 1.2: Patterns formed by self-orgainzation of charges, through charge ordering, charge density wave and electronic phase separation: (a) Charge ordered stripe formation in $La_{1-x}Ca_xMnO_3$ [20]. (b) Charged ordered checkerboard pattern in $Ca_{2-x}Na_xCuO_2Cl_2$ [21]. (c) Charge density wave pattern in cuprate superconductor [22]. (d) Ordered-disordered phase separation in manganite[23].

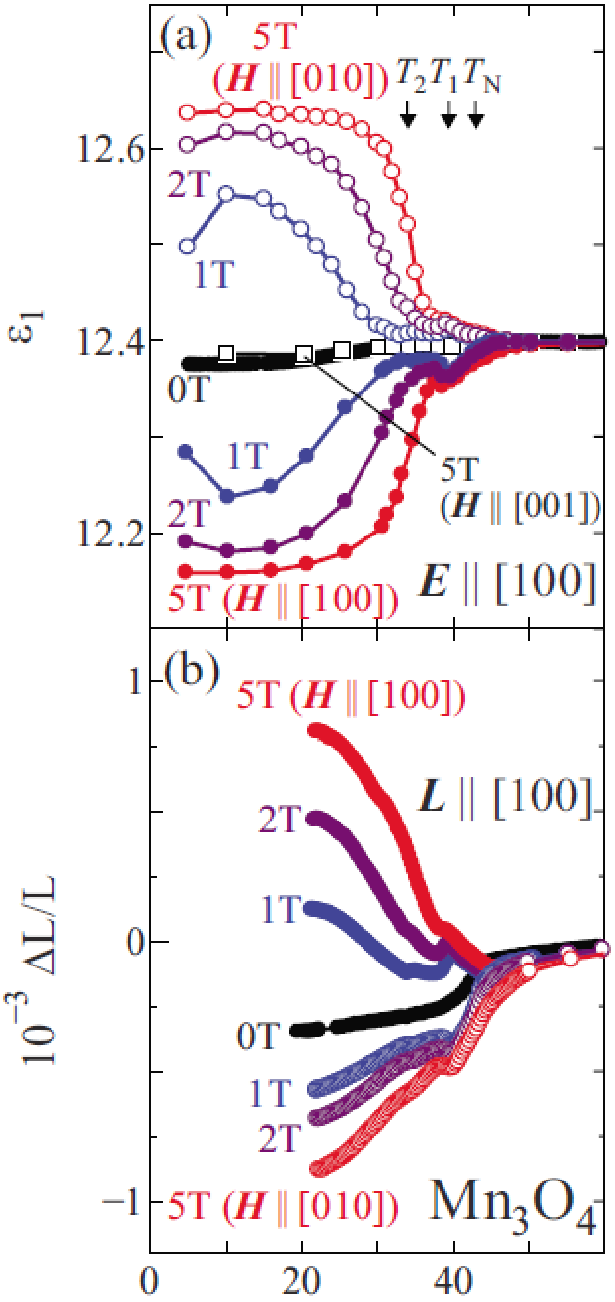

Figure 1.3: Magnetodielectric behavior (a) and magnetoelastic behavior (b) in Mn_3O_4 [31].

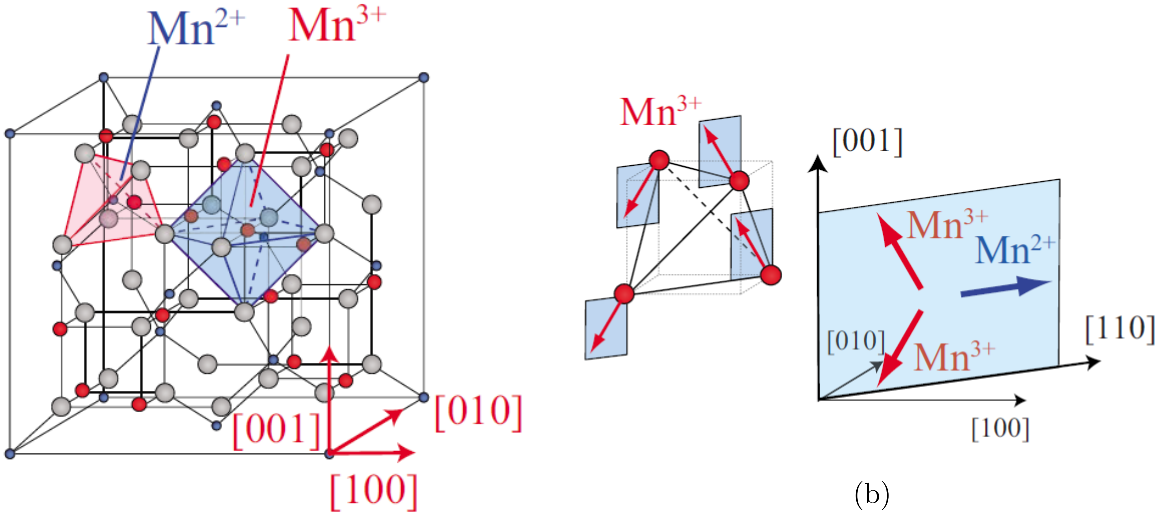

(b)

(a)

Figure 1.4: Lattice and spin structure of Mn_3O_4 [28]. (a) Unit cell in the tetragonal phase (33K to 1417K). (b) Spin orientations in ferrimagnetic phase.

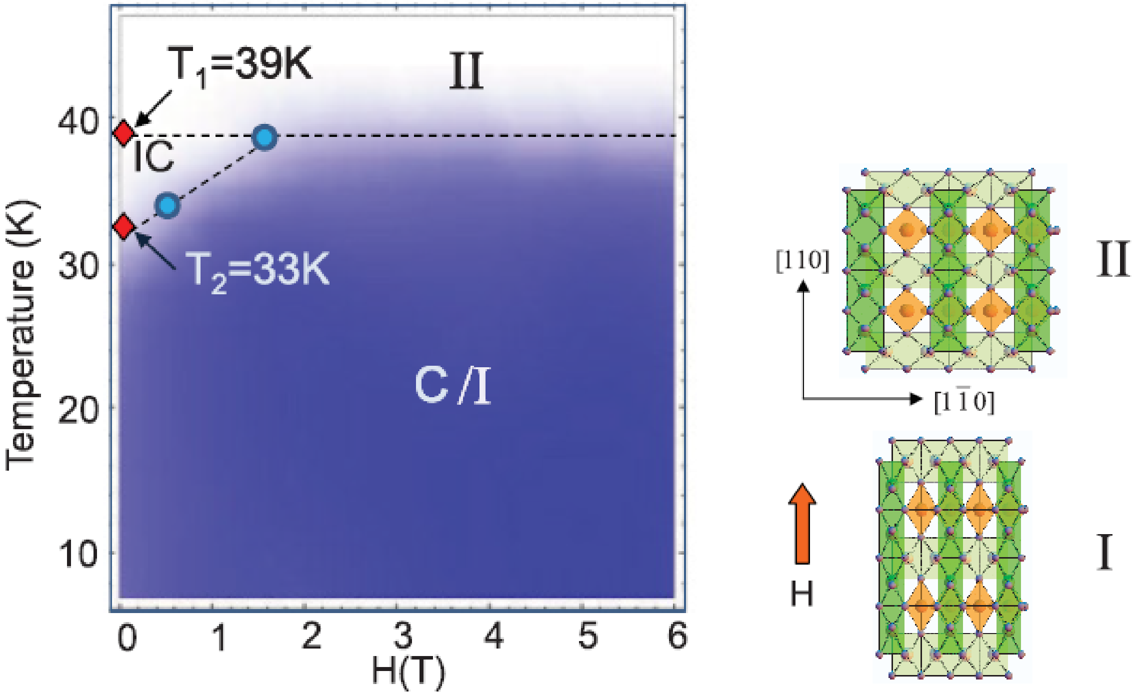

(a)

(b)

Figure 1.5: Phases of Mn$_3$O$_4$ with magnetic field parallel to the magnetic easy axis [110]$_{tetragonal}$. C=commensurate order, IC=incommensurate order [32, 33]. (a) Phase diagram. (b) Lattice structure, viewing along [001]$_{tetragonal}$ axis. Orange diamonds are tetrahedral sites (Mn^{2+}) and green diamonds are octahedral sites (Mn^{3+}).

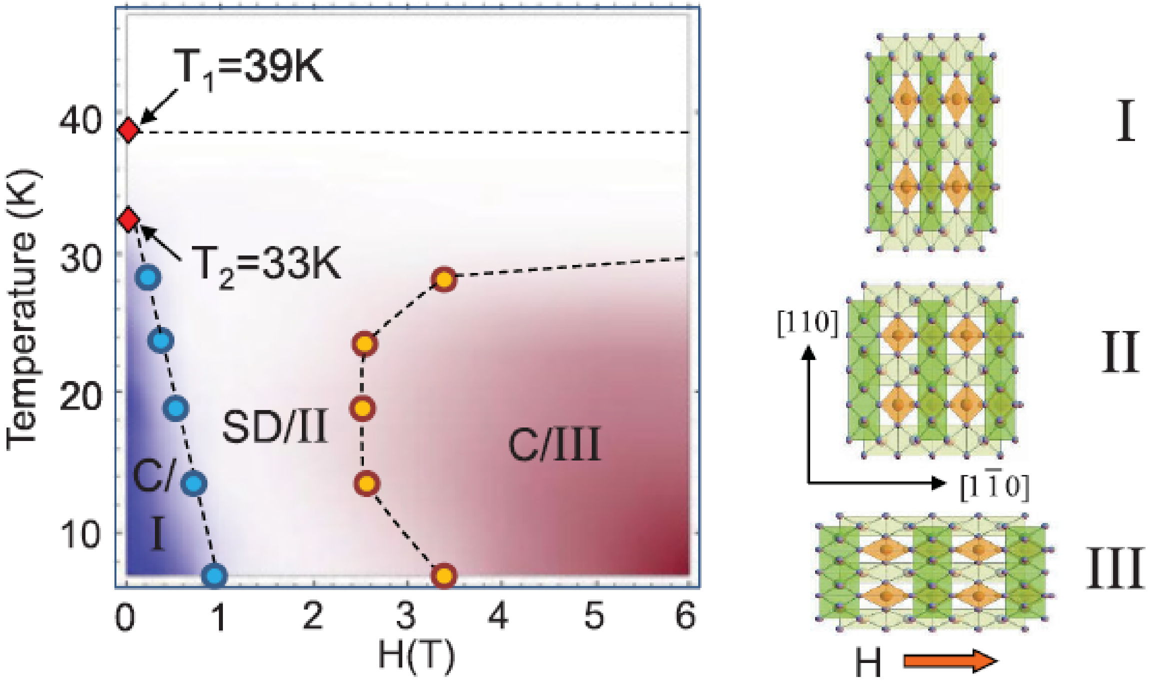

(a) (b)

Figure 1.6: Phases of Mn_3O_4 with magnetic field parallel to $[1\bar{1}0]_{tetragonal}$, transverse to the magnetic easy axis. C=commensurate order, IC=incommensurate order, SD=spin disordered [32, 33]. (a) Phase diagram. (b) Lattice structure, viewing along $[001]_{tetragonal}$ axis.

Chapter 2

Low-Temperature Magnetic Force Microscope

Investigation of the *magneto-structural* phases of Mn_3O_4 naturally comprises of two major components: the structural component is obtained through Electron Backscatter Diffraction (EBSD, Sec. 3.2), and the magnetic component through Low Temperature Magnetic Force Microscopy (LT-MFM). A sample preparation process developed to enable the cross-referencing of these two data components is also presented in Chapter 3. This chapter covers the design, construction and operation of the magnetic force microscope.

2.1 Scanning Force Microscopy Overview

Magnetic Force Microscopy (MFM) falls under the broad umbrella of Scanning Force Microscopy (SFM)[1], microscopes that analyze samples with physical probes through an interaction force between the sample and the probe [51, 44]. An image of the sample surface properties could be obtained by rastering—scanning—the probe across sample surface and monitoring the variation in force. The first SFM, the Atomic Force Microscope (AFM) was developed in 1986 by Binnig, Quate and Gerber [52] where interatomic force between the closest sample atom and probe atom is detected by measuring the deflection of a conducting cantilever using a Scanning Tunneling Microscope (STM). Since then, SFM has exploded into a large range of techniques. MFM specifically images through magnetostatic force and was first demonstrated in 1987 by Martin and Wuckramasinghe [53], [44].

---

[1] Even though Atomic Force Microscopy (AFM) is the more widely used term, I believe SFM more accurately describe the range of force microscope that exist today. In this dissertation the term "AFM" specifically refers to an SFM that detects interatomic forces.

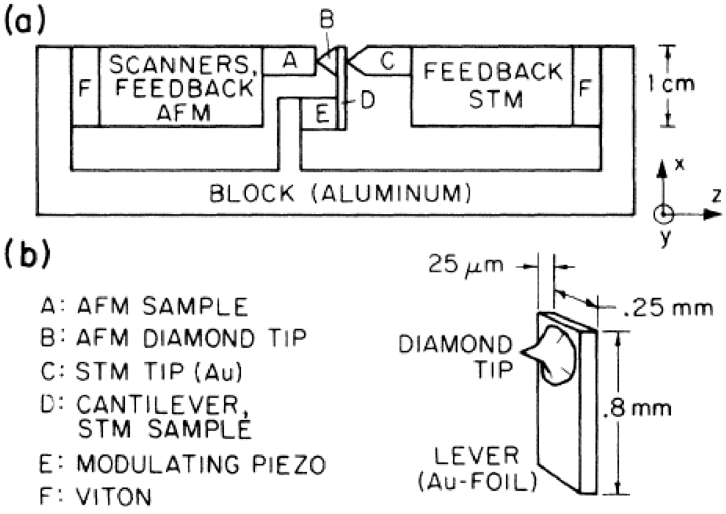

Figure 2.1: Schematic of the first AFM built by Binnig et al [52]

In its simplest form, the SFM operates by first bringing the tip to within the range of the interaction force being analyzed. Cantilever deflection is effected by the force, and detected through a deflection sensor. This mode of operation has been termed static or contact mode [54]. A spatially resolved map of the force response can be constructed by rastering the tip across sample surface (see Fig. 2.2).

Since its inception, SFM has diversified into a wide range of applications. Probing mechanisms now employed include magnetostatic force [53], electrostatic force [55], casimir force [56], piezoelectric coupling [57], etc. For various static mode force measurements the reader is referred to the review by Butt, Capella and Kappl [54] for further reading. Microscopy techniques also increased in their complexity and sensitivity, as exemplified in magnetic resonance force microscopy (MRFM) [58], an MRI-on-a-tip technique with single electron level sensitivity [59].

According to Rugar and Hansman, scanning force microscopes generally contain the following components, regardless the type of force being sensed [51]:

- *A sharp tip mounted on a soft cantilever spring*
- *A way of sensing the cantilever's deflection*

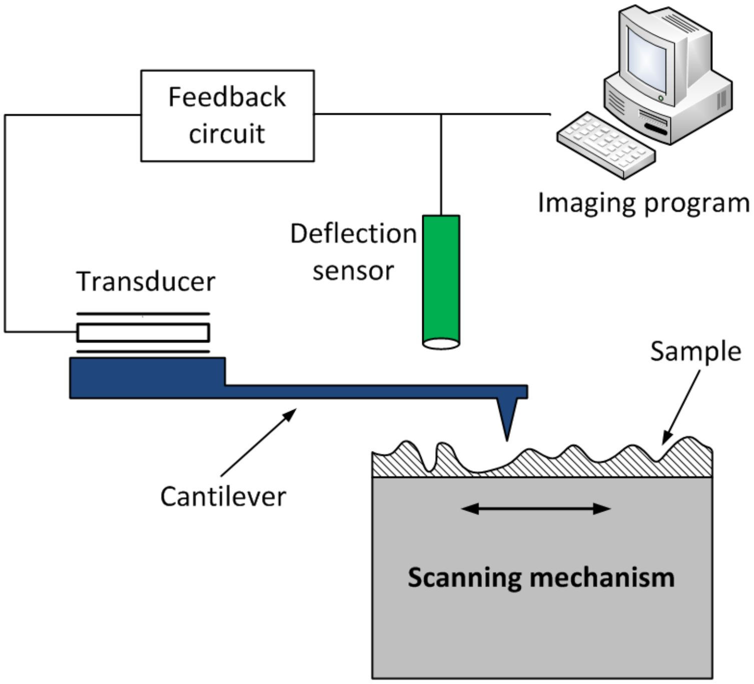

Figure 2.2: Schematic of a basic SFM setup, following Rugar and Hansman [51].

- *A feedback system to monitor and control the deflection (and, hence, the interaction force)*
- *A mechanical scanning system (usually piezoelectric) that moves the sample with respect to the tip in a raster pattern*
- *A display system that converts the measured data into an image*

The following sections are structured following this list of components, with the addition of special considerations given to operating at cryogenic temperatures and in vacuum.

2.2 Low Temperature Considerations

In order to operate at temperatures relevant to the current investigation (generally below 42K), some design considerations must be given to the temperature effects on various components of the microscope. First, components of the microscope must match in thermal expansion rate to a level where alignment between components are not compromised during cool down. This is especially important with regard to the probe itself. Films deposited on the probe shaft can produce differential contraction that result in severe bending of the cantilever, rendering the probe unusable. Secondly, the large amount of piezoelectric elements used in the scanning system (Sec. 2.3.5) also poses a problem. As temperature decreases the piezoelectric coefficients decrease (see, for example, [60]), resulting in reduced scanning and movement capabilities. This effect needs to be countered either by careful calibration or with the use of control parameters inside scanning system. A reference standard for imaging is also extremely beneficial.

As temperature approaches cryogenic level, gases begin to liquefy or freeze. Therefore the LT-MFM must operate in vacuum where liquid or solid depositions on the probe and sample are minimized. Due to the lack of heat transfer from gas molecules, in order to maintain desired sample temperature, microscope operation must minimize heat generation. Moreover, the absence of air damping combined with low temperature result in a higher Q factor in the cantilever than in air [61], which discriminates toward certain detection protocols (see Sec. 2.3.4). Finally, in vacuum environment, electric charge dissipation on insulators such as Mn_3O_4 is extremely difficult, and can result in unwanted tip-sample effects. Surface treatment is therefore needed to alleviate the possibility of contact charging.

2.3 Instrumentation

2.3.1 Pressure, Temperature and Magnetic Field Control

The LT-MFM in this thesis operates at a base temperature of $4K$ and in a vacuum of 10^{-6} to 10^{-8} torr. Low temperature is achieve by mounting the microscope head in a vacuum insert and placed in a cryostat. The microscope head remains in vacuum at all times, while staying in thermal contact with liquid helium-4 through a high thermal conductance mounting flange (Fig. 2.3).

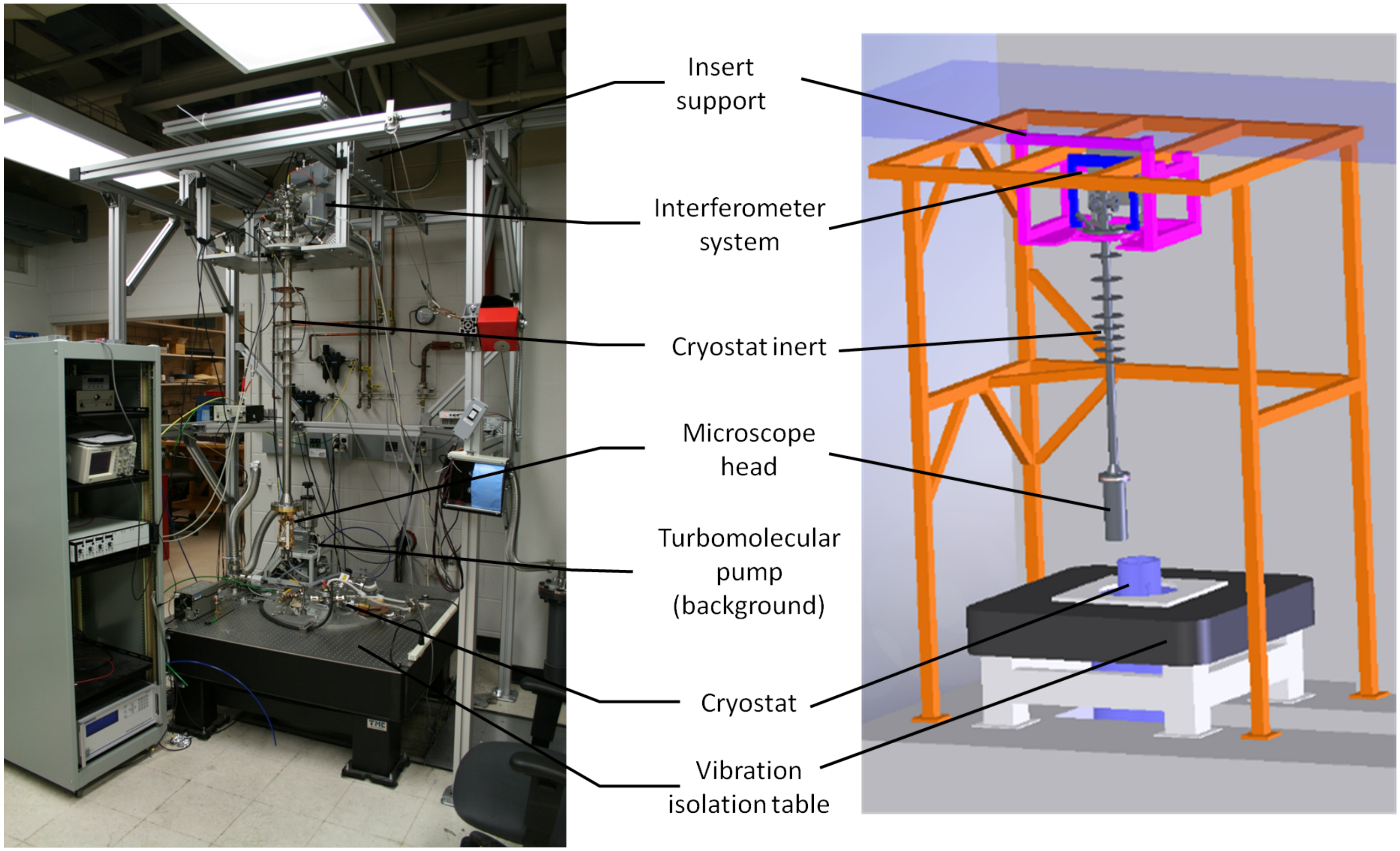

Figure 2.3: Overview of the LT-MFM setup, with photo and simplified engineering model shown side by side. In the photograph, the cryostat insert (counterpart in engineering view: grey) is shown lifted from the cryostat (light blue) and secured onto a sliding platform (magenta, mounted on support structure, orange) for preparation work. The vibration isolation table (table top, black. isolators, white) has a large bore in the middle. The cryostat rests on a large aluminum collar with most of its volume extending through the bore into a ditch in the floor. Vacuum plumbing is secured to the vibration isolation table. When the microscope reaches base temperature, the turbomolecular pump is turned off to reduce mechanical noise. Vacuum is then maintained by cryopumping action. Part of the electronics, including attocube controller and superconducting magnet power supply are housed in a electrical rack next to the cryostat. Other control electronics and computer are placed in another room.

The cryostat is manufactured by Cryomagnetics (Indiana, IN), with a 60 liter capacity and houses a 6 tesla superconducting magnet. The vacuum insert is of our own design. The top of the insert houses all feedthroughs, the laser interferometer and detector assembly (see Sec. 2.3.3) and pump port. The bottom of the insert houses the microscope head. The stainless steel tube connecting the two parts provides mounting points for baffles to improve thermal isolation for the cryostat. Vacuum is generated by a Pfeiffer turbomolecular pump (Pfeiffer Vacuum GmbH, Asslar, Germany) and monitored by a Pfeiffer cold cathode gauge as well as a residual gas analyzer (RGA100, Stanford Research Systems, Sunnyvale, CA).

When in place, the insert extends from the cryostat collar seal to the bottom of cryostat "belly". Toward the bottom, an oxygen-free high conductivity (OFHC) copper flange comes into direct contact with the liquid cryogen and serves as the platform to mount the microscope head (while maintaining vacuum tightness). This mounting flange positions the head in the homogeneous field of superconducting magnet. The enclosure at the cold end of insert has a spring loaded plunger that mates to an indentation at the bottom of cryostat, to prevent modes of vibration in the cryostat insert when it is hanging free from the top. The cryostat insert is almost entirely constructed from stainless steel for good vacuum compatibility. Microscope mounting flange and microscope head are made from gold plated OFHC copper for better thermal conduction.

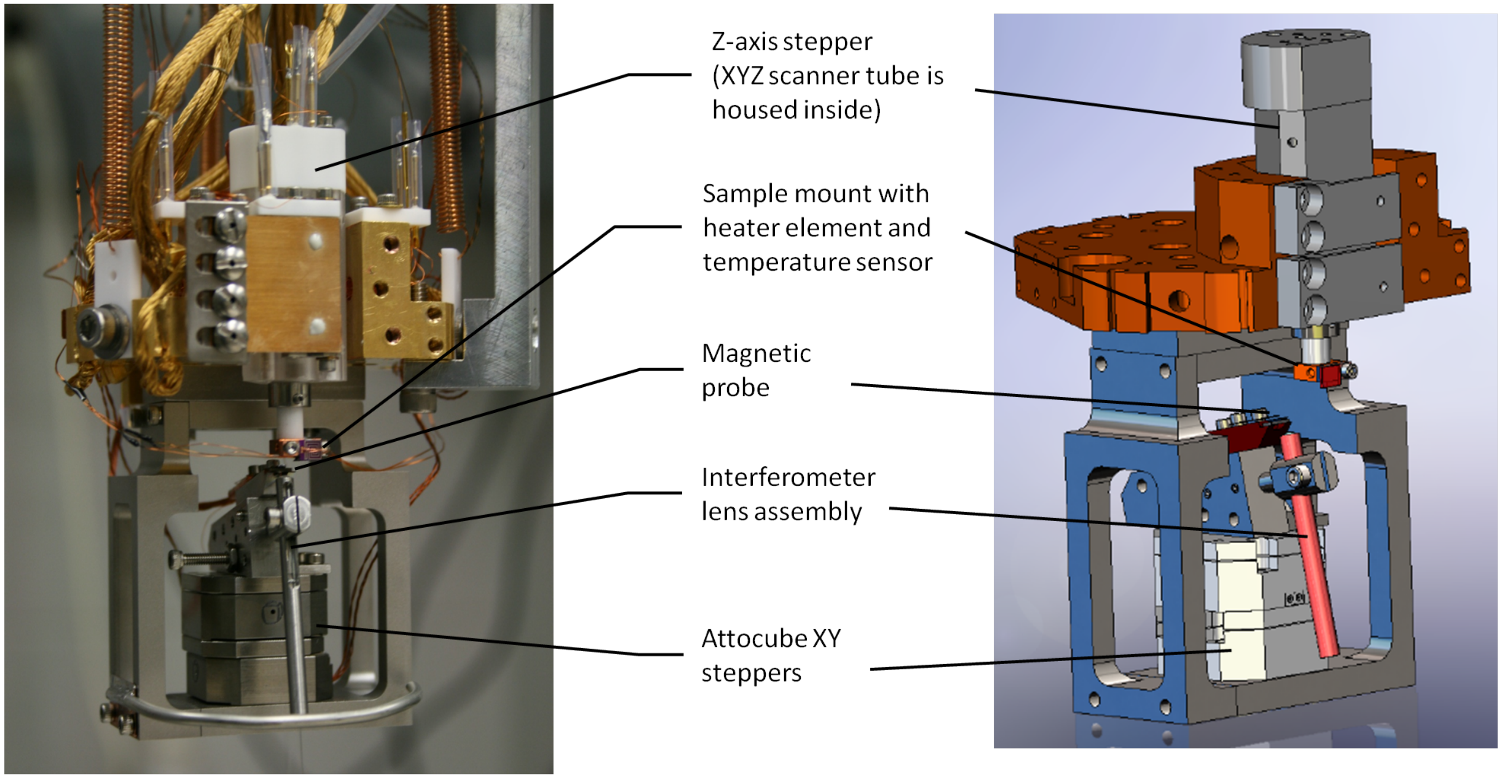

Figure 2.4: Assembly at the bottom of the cryostat insert, photo and simplified engineering model side by side. Springs can be seen suspending the microscope from its mounting flange to isolate the microscope from mechanical vibrations.

There are usually two temperature sensors in use in this MFM setup. A Lakeshore silicon diode temperature sensor (DT-470) is mounted directly onto microscope head for base temperature measurement. A Lakeshore Cernox temperature sensor is mounted directly on the sample stage for accurate sample temperature measurement (see Fig. 3.2).

The sample stage is modular, consisting of with an OFHC sample mount, a machinable ceramic post and attachments such as temperature sensors. Sample temperature is controlled in closed loop by a Lakeshore 325 Cryogenic Temperature Controller, using the Cernox sensor as input and a platinum heating pad (also mounted onto sample stage) as the output.

The sample mount is intentionally kept small and has a high thermal conductivity, while the ceramic post and the piezoelectric scanning tube have poor thermal conductivity. The purpose of this combination is twofold. First, to achieve homogeneity in temperature. The thermal resistance effectively isolates the sample stage from the rest of the microscope, while the sample stage is maintained at a constant temperature of choice. It has been shown using multiple temperature sensors that the temperature difference between extreme ends of the sample stage is less than 0.1K in the range of temperatures relevant to this thesis study. The small thermal mass also reduces the amount of heat needed to modulate sample temperature. Typically, less than 4mW of heating power is needed to maintain a 70K sample temperature at a base temperature of 4K.

2.3.2 Magnetic Force Probe

Because the probe is the force sensor and, for dynamic measurements adopted for this dissertation, also the frequency determining element of the detection circuit, its mechanical properties, both static and dynamic, are responsible for the performance of the microscope. Essential mechanics of an oscillating rectangular cantilever probe is presented below before actual probe is described in detail. SFM probes are also commonly available as triangular or V shaped cantilevers. Analysis on these cantilevers are more complex and falls outside the scope of this dissertation. For treatment of the triangular type, the reader is referred elsewhere [62].

Cantilever Mechanics

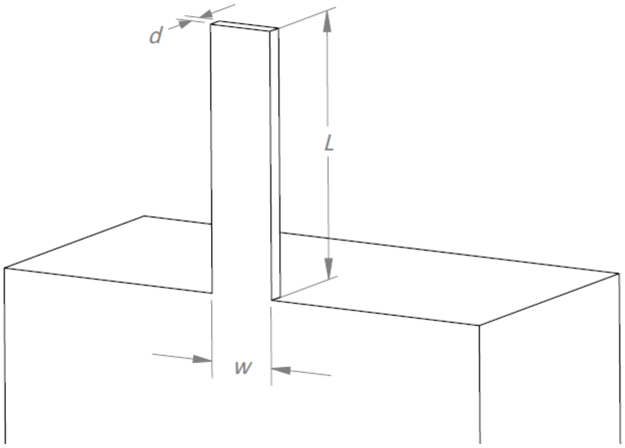

Figure 2.5: A basic cantilever beam made of a single material, typically single crysal silicon or silicon nitride.

Begin with a rectangular cantilever of length L, width w, and thickness d (Fig. 2.5). Further assume that the cantilever and its base are made of a single material of Young's modulus E. the spring constant of the cantilever k is then [54, 63]:

$$k = \frac{Ewd^3}{4L^3} \tag{2.1}$$

When excited at its base by a time dependent force $F_0 \sin(\omega t)$, the cantilever is a driven damped harmonic oscillator described by the time dependent equation of motion [54, 51]:

$$m^* \frac{d^2 z}{dt^2} + \gamma \frac{dz}{dt} + kz = F_0 \sin(\omega t) \tag{2.2}$$

with the resonant frequency ω_0 given by [54]

$$\omega_0{}^2 = \frac{k}{m^*} \tag{2.3}$$

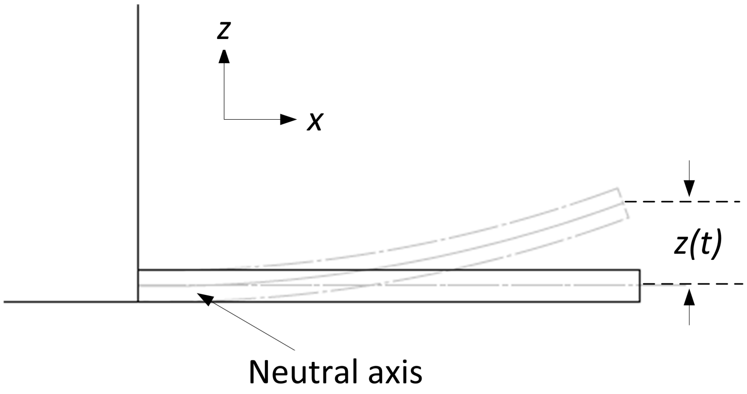

Figure 2.6: Side view of the cantilever beam deflection.

where $m^* = 0.2427 m_{cantilever}$ is effective mass of the cantilever,[2] and $\gamma = \omega_0/Q$ is the damping coefficient [54].

Solution to the equation of motion is

$$z(t) = z_0 \sin(\omega t + \phi) \tag{2.4}$$

Amplitude of oscillation z_0 follows [54, 51]:

$$z_0(\omega) = \frac{F_0/m^*}{\sqrt{(\omega_0^2 - \omega^2)^2 + (\omega\omega_0/Q)^2}} \tag{2.5}$$

The maximum amplitude is reached at frequency [51]

$$\omega_{max} = \omega_0 \sqrt{1 - \frac{1}{4Q^2}} \tag{2.6}$$

In practice, cantilevers in vacuum of 1^{-3} torr or better often have large Q to the order of 10^4 to 10^8 so that $\omega_{max} \approx \omega_0$ [54].

---

[2] Should the probe have a tip at the end of cantilever beam normal to the surface, as most modern commercial probes do, mass of the tip m_{tip} is added to the effective mass $m^* = 0.2427 m_{cantilever} + m_{tip}$. [54]

Probe Preparation

Due to the nature of frequency modulated detection scheme (see Sec. 2.3.4), force resolution of the probe is optimized by having a small k, large Q and large ω_0. Further, a sharp tip is beneficial for imaging purposes as spatial resolution of the magnetic contrast is limited by tip radius. Taking consideration of relevant experimental factors, the Aspire CCS Conical Contact Mode Short Cantilever (Nanoscience Instruments, Phoenix, AZ) is chosen as the basis for our custom magnetic probes. This cantilever is made of single crystal silicon without any coatings to prevent undesirable low temperature behaviors. Crucial parameters of this cantilever are [3]: $L = 210\mu m$, $w = 42\mu m$, $d = 0.9\mu m$, $k = 0.1N/m$, $\omega_0 = 28kHz$, $Q \approx 4\times 10^6$ at $4K$.

In order to produce signal contrast, the minimum requirement for a magnetic force probe is to exhibit a magnetostatic interaction with the sample [44]. It is therefore necessary to deposit magnetic material on a silicon SFM probe. Commercial MFM probes are usually coated fully on tip side with magnetic material, which in our experience could cause cantilever bending during cool down due to differential contraction. We instead developed processes to produce probes with targeted magnetic deposition. The magnetic coating, regardless of the deposition method outlined below, is a tri-layer of 3nm of titanium (adhesion layer), 20nm iron-cobalt (70-30 ratio by weight), and capped with 5nm gold to prevent oxidation.

Probes for low field (less than 20kG) use are coated in a e-beam evaporator (Temescal, Livermore, CA) with a razor blade shadowing the shaft of the cantilever. Only the free end and the tip of the probe is exposed to the flux of deposition materials (Fig. 2.7a). This method produced sharp tips with minimal effect on other cantilever parameters. However, the deposition on the flat surface of the cantilever still produces unwanted cantilever bending in high field (in the range of 30∼50kG) to affect proper imaging.

---

[3] Values listed are typical values specified by manufacturer with the exception of Q. L is the distance from base of the cantilever to the position of elevated tip. The measured values of k by thermal spectrum range from 0.3 to $0.5N/m$. Q is typical value measured by ring down at 4K. See Sec. 2.3.4.

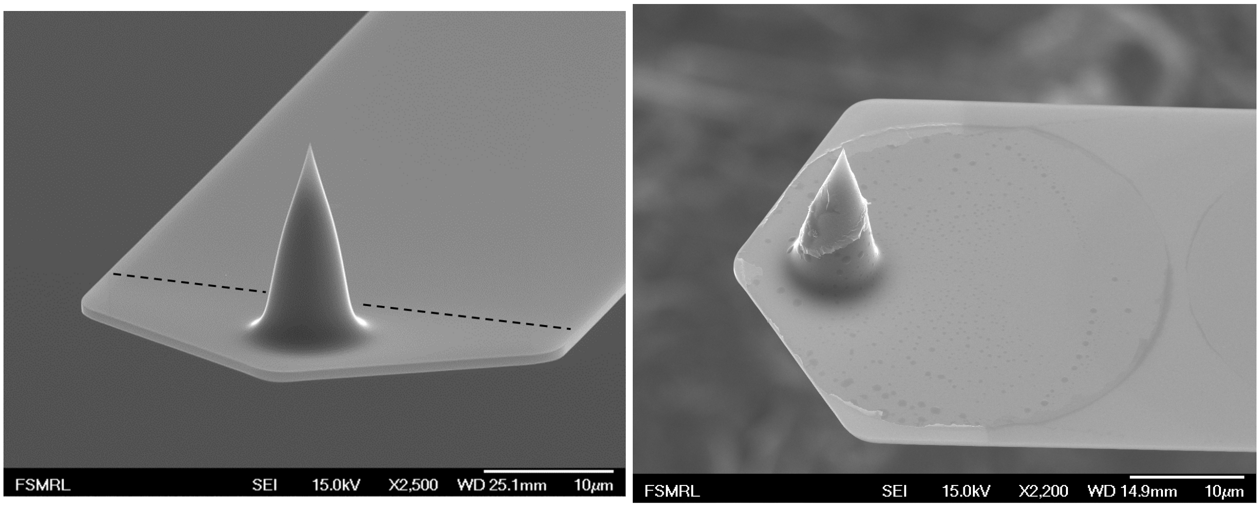

(a) (b)

Figure 2.7: Scanning electron micrograph of Aspire CCS probes: (a) Coated using the shadowed blade method. Dashed lines are added to show the edge of coated film. (b) Coated by liftoff process. Coating can be seen on the tip and near corners of the cantilever.

For high-field use, a more complex coating process is developed[4]. This process is essentially a lift-off procedure. The cantilever is first coated with photoresist AZ5214E (Clariant GmbH USA, Somerville, NJ). Photoresist on the tip is then dissolved by dipping the cantilever in small droplets of diethyl phthalate (approximately $50\mu m$ in diameter) formed on a polydimethylsiloxane-coated surface. Magnetic tri-layer coating is then deposited on the top portion of cantilever using the shadowed deposition method. After deposition, unwanted material is removed by lift-off in acetone and isopropanol alcohol. This liftoff process, while producing a partially coated probe (Fig. 2.7b), does slightly lower the Q of the cantilever due to the residues left by various solutions.

2.3.3 Deflection Detection

Common Deflection Detection Methods

The first deflection detector in AFM was an STM [52]. Soon other methods such as piezoelectric/bimorph sensing, capacitive sensing and optical sensing were developed. Among

---

[4] This process is developed by Tyler Naibert.

them optical sensors are favored for vacuum operation due to their large bandwidth [44]. Most commercial SFMs now use the ”laser bounce” detection method, as shown in (Fig. 2.8). However, laser bounce requires the photodiode situated next to the probe, increasing the overall size of the in-vacuum, cryogenic portion of the microscope.

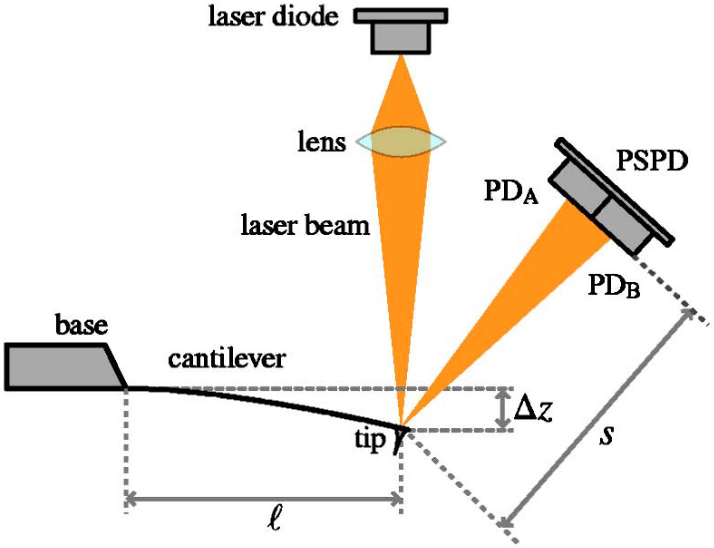

Figure 2.8: Example of a beam bounce deflection sensing SFM [64]. The photodiode (PSPD) is situated close to the cantilever in order to receive reflected photons. This detection method is not used due to the complexity of in-vacuum components. The interferometer system used in this thesis is presented in Fig. 2.9 and Fig. 2.10.

In contrast, an interferometer, specifically a fiber-optic FabryPerot interferometer (FOFPI), requires only a optical fiber to be passed into the vacuum space. This interferometer operates on the optical path difference between the the cleaved end of a single-mode optical fiber and the reflecting surface on a silicon cantilever [65].

Fiber-Optic Fabry-Perot Interferometer Setup

We use a fiber-coupled diode laser from OKI (PL5109L-5A 5mW 1510 nm DFB Laser, OKI Optoelectronics, Japan) as the 1560nm laser source, powered by a laser diode driver from Thorlabs (LDC 240C, Thorlabs, Newton, NJ). Typical current supplied to the laser diode is 17mA. To reduce optical feedback noise and interference noise [64] the source current is modulated by a 200mHz RF signal generated by a voltage controlled oscillator (ZX95-400, Mini-Circuits, Brooklyn, NY) and attenuated by 5dB (Attenuator, Mini-Circuits, Brooklyn, NY, USA).

The output of the laser diode is coupled to the input port of a 99:1 directional coupler (FFC-X142PB1XX-SFO572, JDS Uniphase, Milpitas, CA USA) as shown in Fig. 2.9. The intensity of laser that enters this directional coupler can be adjusted by how tightly the output (of the laser diode) and input (of the directional coupler) are screwed together.

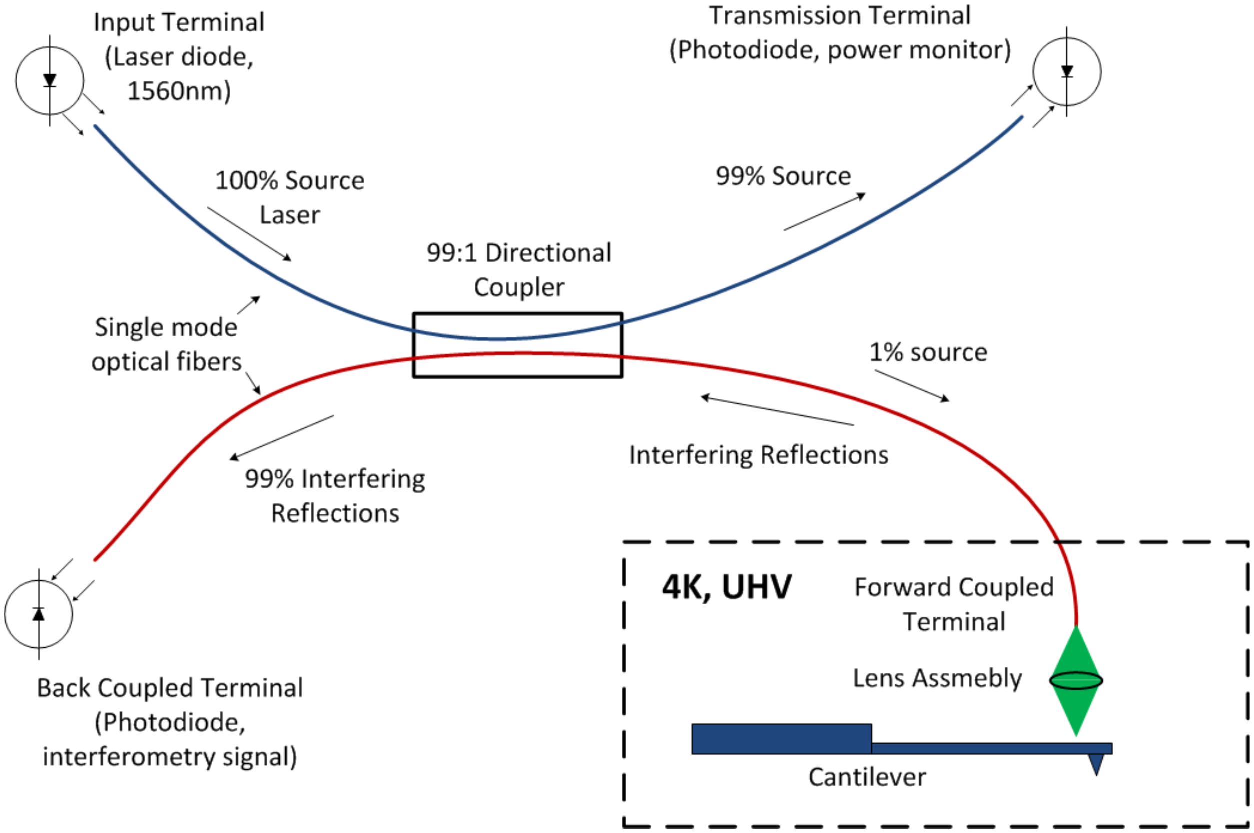

Figure 2.9: Schematic of the fiber-optic Fabry-Perot interferometer using a 1560nm laser and a 99:1 directional coupler. This interferomety setup is particularly well suited for vacuum and cryogenic operations due to the small in-vacuum package as well as minimal need for vacuum feedthroughs.

The directional coupler has two optical fibers, resulting in four terminals: input, transmission, forward coupled and back coupled [66]. 99% of the incoming laser is transmitted down the same optical fiber to a reference photodiode, generating a voltage signal representative of the overall laser power. 1% of the laser is coupled to the other optical fiber in the directional coupler, traveling in the forward coupled direction toward the cantilever. At the end of the forward coupled fiber, the cleaved end of the optical fiber reflects part of the laser, while the rest exits the optical fiber. Part of the light reflected back from the cantilever surface (focused by the lens on its way back) re-enters the optical fiber and interferes with the end-reflected light. The resulting light travels down toward the back coupled terminal, where a photodiode convert the interference light into a voltage signal.

In order for the forward terminal to reach the cantilever inside the vacuum space, the optical fiber is fed through a Swagelok compression fitting with a machined Teflon ferrule inside[5], per [67]. Once inside the vacuum space, the fiber is passed through a smooth stainless steel tube to the microscope head at the end of the cryostat insert. This end of optical fiber is first stripped of the coating layer, then cleaved using a commercial optical fiber cleaver (S323, FITEL, Japan). This cleaved surface reflects approximately 4% of the incident light when it is smooth.

A lens assembly (Fig. 2.10) at the end of the optical fiber is used to achieve longer working distance and focus the light onto the reflecting surface of cantilever. The lens assembly consists of a machined stainless steel tube with a 14mm long, 129μm ID, 1mm OD borosilicate ferrule (BD ACCU-GLASS, St. Louis, MO) epoxied inside using Epotek H74 (Billerica, MA). The ferrule has a tapered end, allowing the stripped, cleaved optical fiber to be inserted. Once in place and secured by epoxy, the end of the fiber is in focus of a lens with 1.6mm focal length (350450C00 coating:10238, LightPath, Orlando, FL) epoxied to the end of the stainless steel tube using TorrSeal (Varian Inc, Fort Lauderdale, FL). This lens focuses the light to the cantilever placed 1.6mm away. The light is incident normal to the cantilever surface. To reduce reflections from the sample surface, the cantilever (together with the lens assembly) is tilted 12° relative to the sample surface.

---

[5] Teflon and Swagelok are trade names that are used here for identification purposes only.

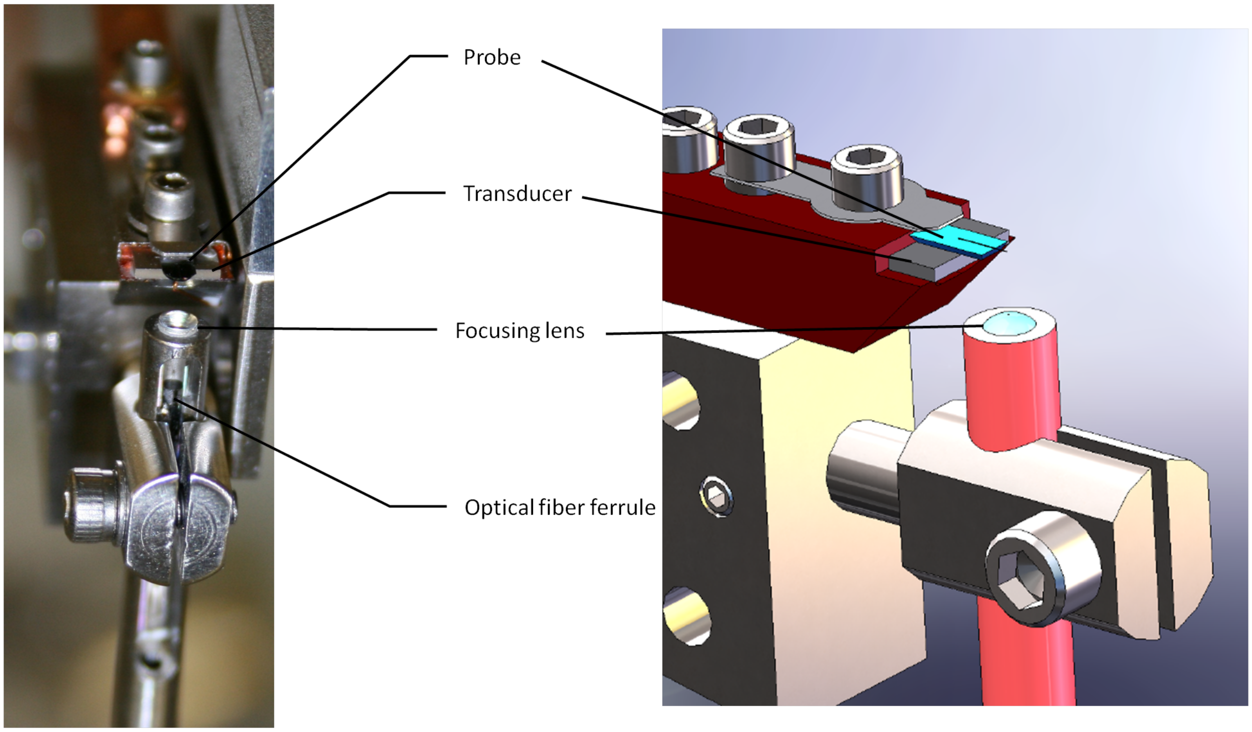

Figure 2.10: Lens assembly for the FOFPI and cantilever mount assembly, photo and simplified engineering model side by side. Lens to cantilever alignment is made possible by a rotating-sliding lens holder. Lens tube (pink) is clamped to a smooth stainless steel rod, which allows the clamp to rotate around the rod axis, providing the adjustment transverse to the cantilever (Y). Adjustment along cantilever shaft axis (X) is done by pushing the rod with a 0-80 screw (out of view) and securing the rod in position with two set screws. To adjust the focus, we loosen the clamping mechanism and slide the lens tube in-out.

Interferometry and Signal Conversion

Assuming for the time being that the laser is incident on the free end of the cantilever. Any deflection, z, of the cantilever produces a change in path difference between the fiber-reflected light (of intensity I_f) and cantilever-reflected light (of intensity I_c). This change in path difference results in a sinusoidal response to deflection in the well known formula

$$I(z) = I_f + I_c + 2\sqrt{I_f I_c}\cos(\frac{4\pi(z+Z)}{\lambda}) \tag{2.7}$$

where λ is the laser wavelength and capital Z is the distance between the end of the fiber and the cantilever in its equilibrium position. This intensity is detected by detector circuit to produce an analog voltage signal V proportional to I. We denote the maximum value and minimum value of the voltage signal V_{max} and V_{min} respectively.

To deduce magnitude of deflection from this voltage signal, we exploit the fact that deflection is generally small compared to laser wavelength. By fine-tuning the wavelength (through temperature adjustment on the laser diode body) so that $Z = \lambda(n + \frac{1}{4})/2$, deflections small compared to λ allows expansion of the cosine function about 0, giving V as a linear function of z:

$$V(z) = \frac{V_{max} + V_{min}}{2} + \frac{2\pi z(V_{max} - V_{min})}{\lambda} \tag{2.8}$$

V_{max} and V_{min} can be easily measured by changing laser wavelength to produce interference fringes and take measurement of the voltage signal at extrema.

Cantilever Oscillation Modes and Amplitude Estimation

In order to accurately measure the deflection at the probe tip, the laser is best focused at the end of the cantilever, exactly at base of the tip on the opposite side of cantilever. However this arrangement produces several problems in actual experiments, especially when the probe is near sample at low temperatures. Undesirable effects include sample surface reflection affecting interference pattern and sample heating from incident and scattered laser. Therefore it is advantageous to place the laser down the shaft of cantilever, some distance away from the tip. This necessitates calculating the tip displacement from the displacement of another point on the cantilever shaft.

Let us take a moment to look at the shape of an oscillating cantilever. As a driven damped harmonic oscillator, the cantilever has multiple eigenmodes of oscillation, the first 4 of which are shown in Fig. 2.11. The fundamental mode is used for imaging in this thesis and the cantilever shape in this mode is described by [68]:

$$c(x) = \frac{1}{2}\{[\cos(\kappa_1 x) - \cosh(\kappa_1 x)] + \frac{-\cos(\kappa_1 L) - \cosh(\kappa_1 L)}{\sin(\kappa_1 L) - \sinh(\kappa_1 L)}[\sin(\kappa_1 x) - \sinh(\kappa_1 x)]\} \quad (2.9)$$

Here x is the distance from the the base of the cantilever to the point of interest on the shaft of cantilever. $c(x)$ gives the fractional vertical displacement at position x, compared to the displacement at free end of the cantilever i.e. $c(0) = 0$ and $c(L) = 1$. The coefficient κ_1 is such that $\kappa_1 L = 1.8751$ [68].

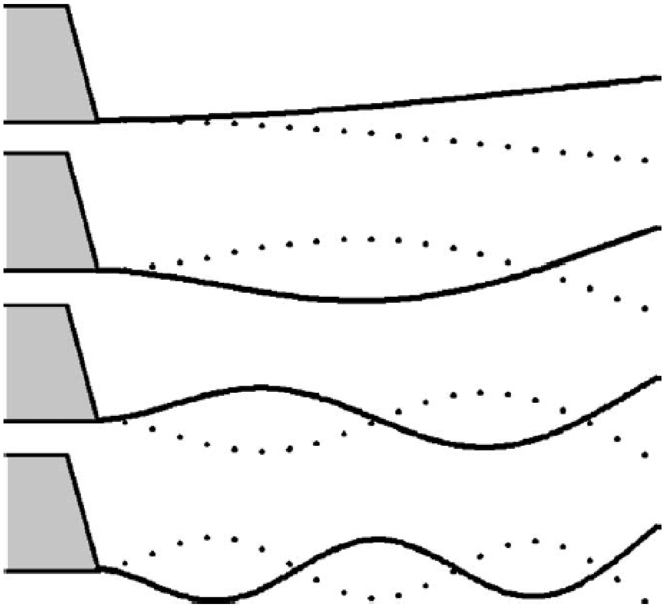

Figure 2.11: First four modes of a rectangular cantilever [54], scaled for identical amplitude at the free end.

In order to estimate the deflection of the cantilever tip, we measure x before each experiment optically using a calibrated microscope (Olympus SZ1145TR, Olympus, Japan). The deflection at the laser incident point z_{laser} is used together with $c(x)$ to calculate the tip displacement $z_{tip} = z_{laser}/c(x)$.

2.3.4 Feedback Control, Frequency Detection and Noise Considerations

Dynamic Force Detection

As SFM techniques evolve out of its infancy, it is found that static mode is often plagued by a force noise following a $1/\omega$ spectral distribution and low frequency vibration issues (see Fig. 2.12) [69, 70]. Moreover non-contact forces, for example electrostatic or magnetostatic forces [44] inherently require a non-contact force measurement. Non-contact force detection, using oscillating cantilevers and hence dynamic in nature, were developed for these applications. In static mode, cantilever spring constant is the relevant probe parameter and detection sensitivity relies on cantilever deflection detector [54]. In contrast,dynamic force detection involves the entire frequency response spectrum of the particular cantilever (see Eq. 2.5 and Fig. 2.12).

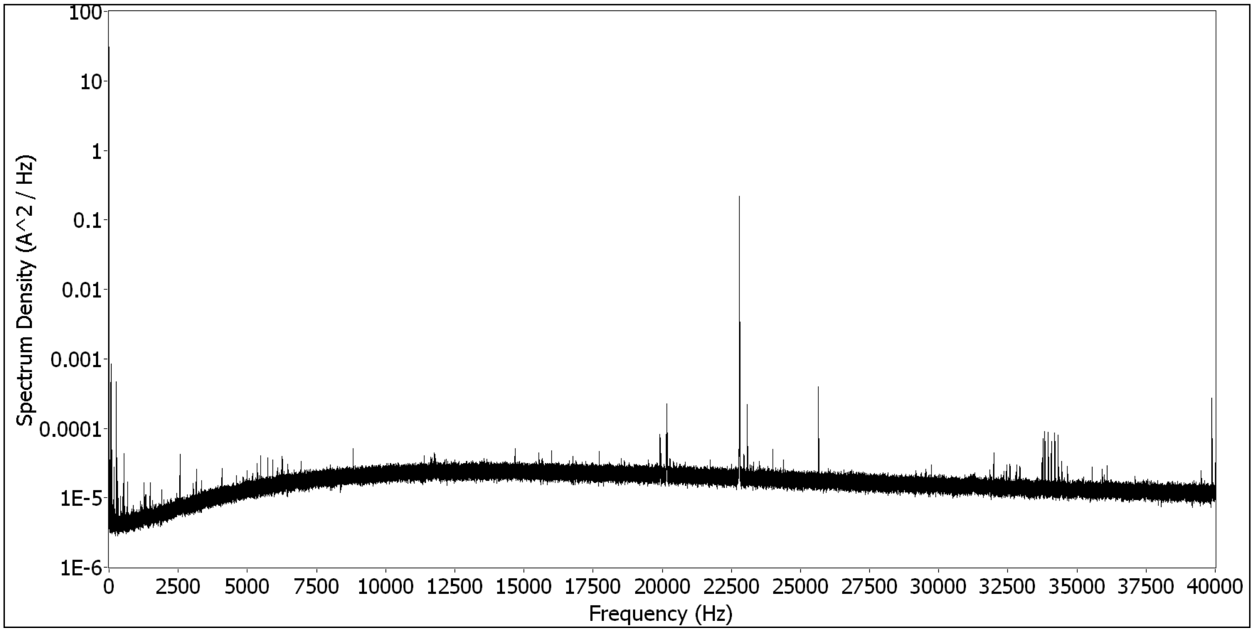

Figure 2.12: Thermal spectrum of an undriven cantilever in UHV at 77K from DC to 40kHz. Resonance frequency is 22.7kHz. Note the sharp rise of noise floor near DC.

There are two common dynamic force detection schemes: amplitude modulation (AM) and frequency modulation (FM) [61, 44]. AM works on the principle of oscillating the cantilever at a set frequency slightly off resonance. This places the cantilever on the slope of resonance peak in the spectrum (Fig. 2.13). As the force modulates the resonant frequency of the cantilever, the resonance peak shifts in frequency space, allowing the SFM to demodulate the force signal as a change in steady state oscillation amplitude [61].

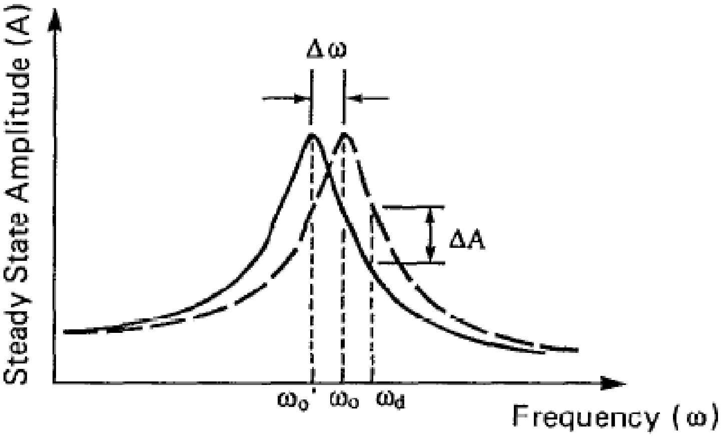

Figure 2.13: Force detection by AM and FM methods [61]. In AM, the cantilever is driven at frequency ω_d. Resonant frequency shift of $\Delta\omega$ results in an amplitude change ΔA. FM detection, on the other hand, tracks the frequency peak directly by always driving the cantilever on resonance.

In vacuum below approximately 10^{-3} torr, air damping becomes very small and cantilever Q increases, resulting in a very narrow resonance peak. The sharp slopes of the narrow peak limits the usable bandwidth of the cantilever, often to the order of less than 1Hz [61].

Force Feedback Loop

FM detection is adopted in order to maintain usable bandwidth and take advantage of the increased Q in vacuum. Instead of exciting cantilever off-resonance, the cantilever is alway excited at its own (instantaneous) natural frequency and the force signal is read out directly from cantilever frequency shift. This “self-oscillation” is achieve by feeding back the cantilever displacement signal back to the cantilever driving transducer [61, 71, 72] (Fig. 2.14). The displacement signal from the interferometer is first amplified and band-pass filtered between 1kHz and 30kHz by an SRS SR560 amplifier (Stanford Research Systems, Sunnyvale, CA). This filtered signal is used to produce two separate drive signals:

- In-phase drive: the filtered displacement signal is amplified by a variable gain amplifier, which is controlled by a PID program in a Field Programmable Gate Array (FPGA, PXI-7833, National Instrument, Austin, TX). The PID program automatically varies the gain for this in-phase component to maintain the self-oscillation amplitude at a user-specified level.
- Out-of-phase drive: the filtered displacement signal is phase-shifted by π and amplified by a variable gain amplifier at user discretion.

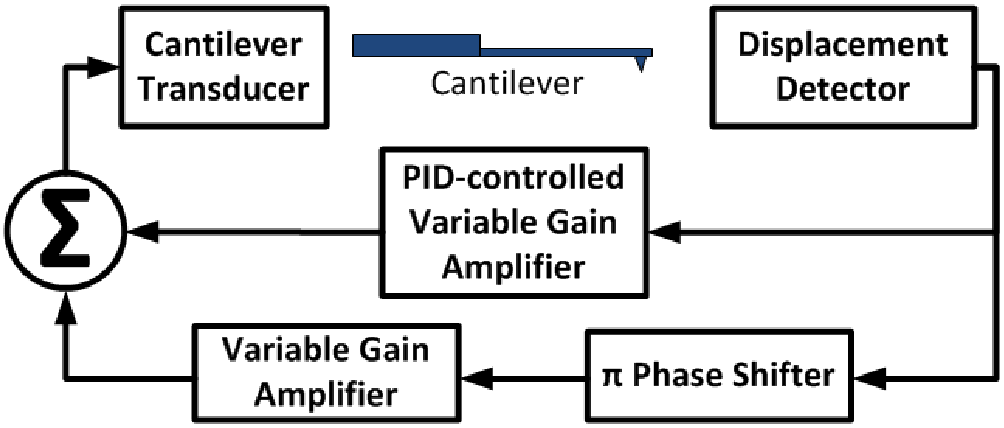

Figure 2.14: Schematic of the feedback loop in cantilever self-oscillation system. Oscillation amplitude is controlled by the PID-algorithm that controlls the in-phase component of the drive signal.

These two drive signals are then summed and sent to the transducer (piezoelectric ceramic, EBL, East Hartford, CT) to excite the cantilever. This feedback scheme produces exceptional force sensitivity and cantilever motion stability [72]. The Q of the cantilever is measured by driving the cantilever at a constant amplitude, then abruptly turn off the drive signal to the transducer. Cantilever transient is recorded and fitted to an exponentially decaying sinusoidal oscillation. The Q factor is related to the decay time by [63]:

$$Q = \frac{\omega_0 \tau}{2} \tag{2.10}$$

Frequency Readout

A phase locked loop (PLL) is employed to determine the cantilever frequency (Fig. 2.15). The filtered displacement signal is digitized by FPGA. The digital signal is then sampled, using a square wave generated by a local oscillator (Agilent 33220A Function Generator, Agillent, Santa Clara, CA) as trigger, an even number of samples per period of oscillation. Samples from the first and second halves of the oscillation were summed respectively. The difference between the sums (half-sum-difference) is the phase comparator result. This half-sum-difference is entered into a PID algorithm that produces a voltage signal to the frequency modulation input to the local oscillator, with a set point of zero. This feedback loop matches the frequency of the square wave to the displacement signal, by adjusting the square wave frequency to produce a half-sum-difference of zero (zero phase difference). The local oscillator frequency is then read out by FPGA program as frequency data.

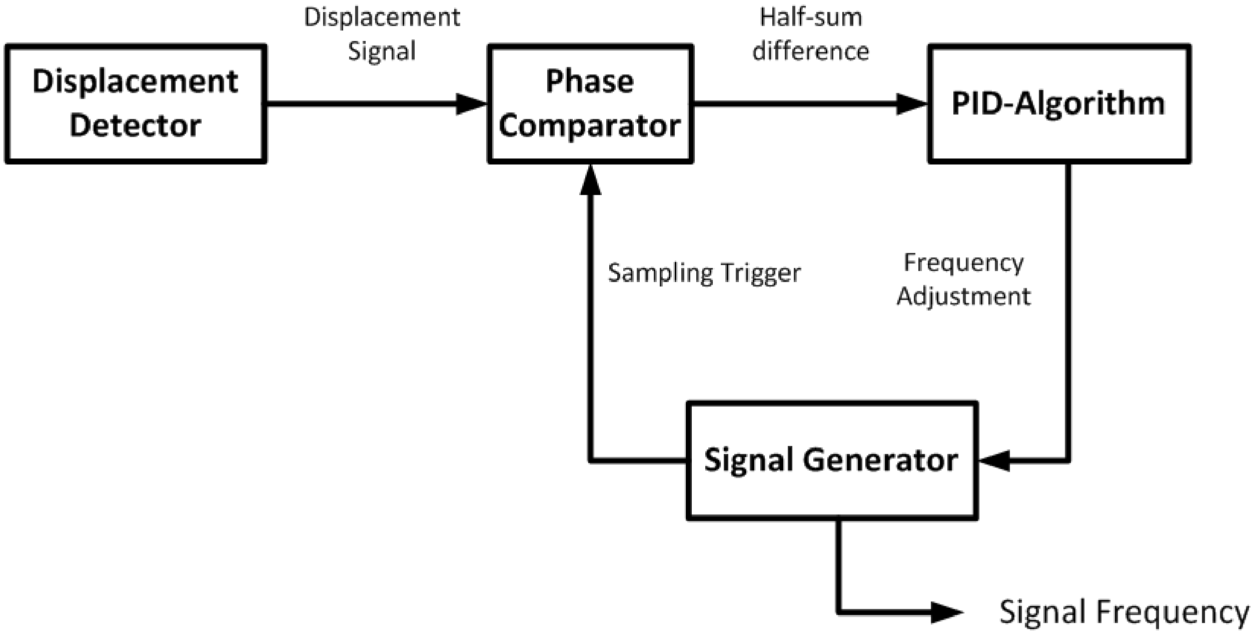

Figure 2.15: Schematic of the frequency readout using a phase locked loop.

Force Sensitivity and Noise Considerations

The noises that limit the sensitivity of an FM SFM are, according to Albrecht et al [61]:

- *Thermal vibrations of the cantilever*
- *Noise in the displacement sensor*
- *Noise generated in the oscillation control amplifier and other electronics*

Assuming for the moment that the SFM is thermally limited [72]. From equipartition theorem [61],

$$\frac{1}{2}m\omega_0^2\langle z_{th}^2\rangle = \frac{1}{2}k\langle z_{th}^2\rangle = \frac{1}{2}k_bT \tag{2.11}$$

where $\langle z_{th}^2\rangle$ is the mean-square displacement at the end of the cantilever due to thermal excitation and k_b the Boltzmann constant. This equation is the basis of measuring the cantilever spring constant, as $\langle z_{th}^2\rangle$ can be easily measured with an undriven cantilever at a known temperature.

The minimum detectable force gradient in FM detection is then [61] :

$$\delta F_{min} = \sqrt{\frac{4kk_bTB}{\omega_0 Q\langle z_{osc}^2\rangle}} \tag{2.12}$$

where B is the detection bandwidth and $\langle z_{osc}^2\rangle$ is the mean-square oscillation amplitude at the end of cantilever. It is apparent that to achieve the highest force resolution, the probe should have a low spring constant k, a high frequency ω_0, a high Q, a large oscillation amplitude[6] and operate at a low temperature T.

---

[6] However, a large oscillation amplitude generally increases the average sample-tip distance, hence producing lower SNR.

2.3.5 Position control, Vibration isolation and Imaging

Position Control and Vibration Isolation

Relative motion between the probe and sample is realized by a combination of commercial and home-built positioners. XYZ rough positioning is handled by steppers and XYZ scanning by a piezoelectric tube scanner.

The probe and lens assembly is mounted on an XY positioning stage from attocube (ANPx101/RES, attocube systems AG, Munchen, Germany) paired with an attocube ANC300 stepper controller. The attocubes provide 5mm range for each axis with a usable resolution of approximately 1μm. attocube's Daisy program provides computerized XY stepper control.

The Z stepper is separate from XY stepper. The stepper body is a sapphire triangular prism held in a V-channel by six stacks of piezoelectric ceramic elements. Each stack correspond to an analog voltage channel of an NI PXI-6733 (National Instrument, Austin, TX) board, amplified by a Trek PZD700 high voltage amplifiers (Trek Inc, Medina, NY). Z stepper operates by increase the voltage slowly across piezoelectric stacks, shearing them and moving the prism in one direction by the amount stacks are sheared. One by one, the voltage across each stack switches to opposite polarity in a step function. This voltage polarity switch shears piezoelectric stack in the opposite direction. Inertia of the heavy stepper prism body and the friction from other 5 stacks hold the prism body stationary during the polarity switch of each stack. After all stacks have completed the switch, the voltage across stacks is ramped down to zero slowly. The prism by now have "inchwormed" in one direction by twice the sheared distance.

The sample stage is attached upside-down to one end of an XYZ piezoelectric scanning tube (EBL Products, East Hartford, CT). The scanning tube is then attached to the Z stepper prism. The XYZ scanner is powered by three analog voltage channels on another PXI-6733 analog output board, amplified by a custom voltage amplifier. The scanning tube provides approximately 10μm$\times10\mu$m scan range in XY at 77K, which decreases to 4μm$\times4\mu$m at 4K. Z motion and scanning are manipulated by a program written in Labview (National Instrument, Austin, TX) environment.

Measures were taken to isolate the microscope from outside vibration during imaging and other operations. As a first step, the cryostat is mounted onto a floating vibration isolation table which filters out most mechanical vibrations from the environment. The cryostat insert is anchored at both ends when inserted into the cryostat, preventing vibration amplification due to cantilevering. Inside the cryostat insert, the microscope head is suspended by springs from the mounting flange.

Imaging

A typical imaging session begins by magnetizing the magnetic probe in desired direction in 3T field. The probe is then put into self-oscillation at a set amplitude–typically 25nm. After noting the cantilever frequency far from the sample, the probe is then brought close to the sample surface by the Z stepper. The resonant frequency of the probe and its first derivative with respect to Z serve as indicators of proximity. On the initial coarse approach, the stepper is stepped a number of steps before stopping to check for proximity. Because of the temperature effect on piezoelectrics, different voltages and step numbers are used for coarse approach: 4 steps at 150V peak voltage at room temperature; 5 steps at 200V at 77K and 6 steps at 300V at 4K. These values ensure the probe does not crash into the sample. Coarse approach ends when cantilever frequency shift is greater than 0.2Hz from the initial frequency far from sample.

A fine approach is then performed, where the Z stepper and XYZ scanner together perform an inchworm motion: the XYZ scanner is extended, along Z, at a particular XY position, and proximity test ($df/dZ > 0.05Hz/nm$) is performed along the extension at equal intervals, typically 4nm. Stepper would step closer to the sample surface (using the stepping configurations discussed above) if proximity test fails throughout the full range of extension. This process is then repeated until proximity test returns true. The Z axis value of the scanner is recorded and this is the reference height for this particular XY position.

A surface tilt map is then obtained by doing fine approaches without stepping at 9 positions, with self-oscillation amplitude set to scan values (25nm and 8nm being most often used): four extreme corners of desired rectangular scan area, the mid point of the four edges, and the center. These values are stored and used to create a reference surface through two dimensional linear interpolation. This reference surface is an approximation of the topography of the desired scan region, ∼100nm above the sample surface.

The ideal scan height (the distance between tip and surface) depends on the self oscillation amplitude. Scan heights of 140nm for 25nm amplitude and 120nm in the case of 8nm are usually used when 20nm tall location markers are within scan area. The probe is rastered across reference surface, while maintaining constant distance from the surface with the help of interpolated reference surface contour, by simultaneous output via analog voltage channels to the XYZ scanner. Frequency data is recorded synchronous to the rastering to produce the MFM image using a Labview program.

Magnetic Contrast

Majority of the interaction comes from the very apex of the tip [73] with the weighting factor falling off rapidly farther from the apex. The magnetic contrast in images can be approximated by first modeling a solid tip of bulk material, and the magnetic contrast of a thin film probe can be estimated by applying the superposition principle.

Assuming a stray field from the sample with magneziation M_S being [74]

$$H(r) = -\int_{sample\ volume} \nabla \bullet M_S(r'') \frac{r - r''}{|r - r''|^3} dV'' + \int_{sample\ surface} \hat{z} \bullet M_S(r'') \frac{r - r''}{|r - r''|^3} dS'' \quad (2.13)$$

The force acting on a volume element in the tip dV' is, then, [74]:

$$dF_{mag} = \nabla[M_T(r') \bullet H(r + r')]dV' \tag{2.14}$$

Taking the component normal to cantilever surface, and integrate over tip volume, we have the magnetic force derivative for arbitrary sample magnetization and arbitrary cantilever orientation [74]:

$$F'_{mag} = \int_{tip} \sum_{i=x,y,z} \sum_{j=x,y,z} \sum_{k=x,y,z} n_j n_k M_T, i(r') \times \frac{\partial^2 H_i(r + r')}{\partial r_j \partial r_k} dV' \tag{2.15}$$

However, the exact formulation of the magnetic vector field from the tip is extremely difficult to obtain (high resolution electron holography often employed). For reasonably satisfactory interpretation, a common approach is to model the probe as a point dipole and treat the tip moment and effective tip-sample separation as free parameters to be fitted to existing data [44].

The detected force component is along z as the cantilever only deflects in this direction. The force gradient detected by FM is therefore [74]

$$F'_{mag} = \frac{dF_{mag,z}}{dz} = m_x \frac{\partial^2 H_x}{\partial z^2} + m_y \frac{\partial^2 H_y}{\partial z^2} + m_z \frac{\partial^2 H_z}{\partial z^2} \tag{2.16}$$

Here H_i are components of the stray field from sample and m_i the tip dipole moment. A perfect dipole aligned with z axis would result in the force gradient $F'_{mag} = m_z \frac{\partial^2 H_z}{\partial z^2}$. This is a good enough approximation for samples where magnetization is mostly aligned in the z axis (Fig. 2.17b). Longitudinally recorded media serves as a good example of the MFM signal of horizontally magnetized materials (Fig. 2.17a). The reader is referred elsewhere for experimental results of longitudinal media [74], perpendicular media [75], treatment of force calculations [73, 74] and computer simulation [76] results.

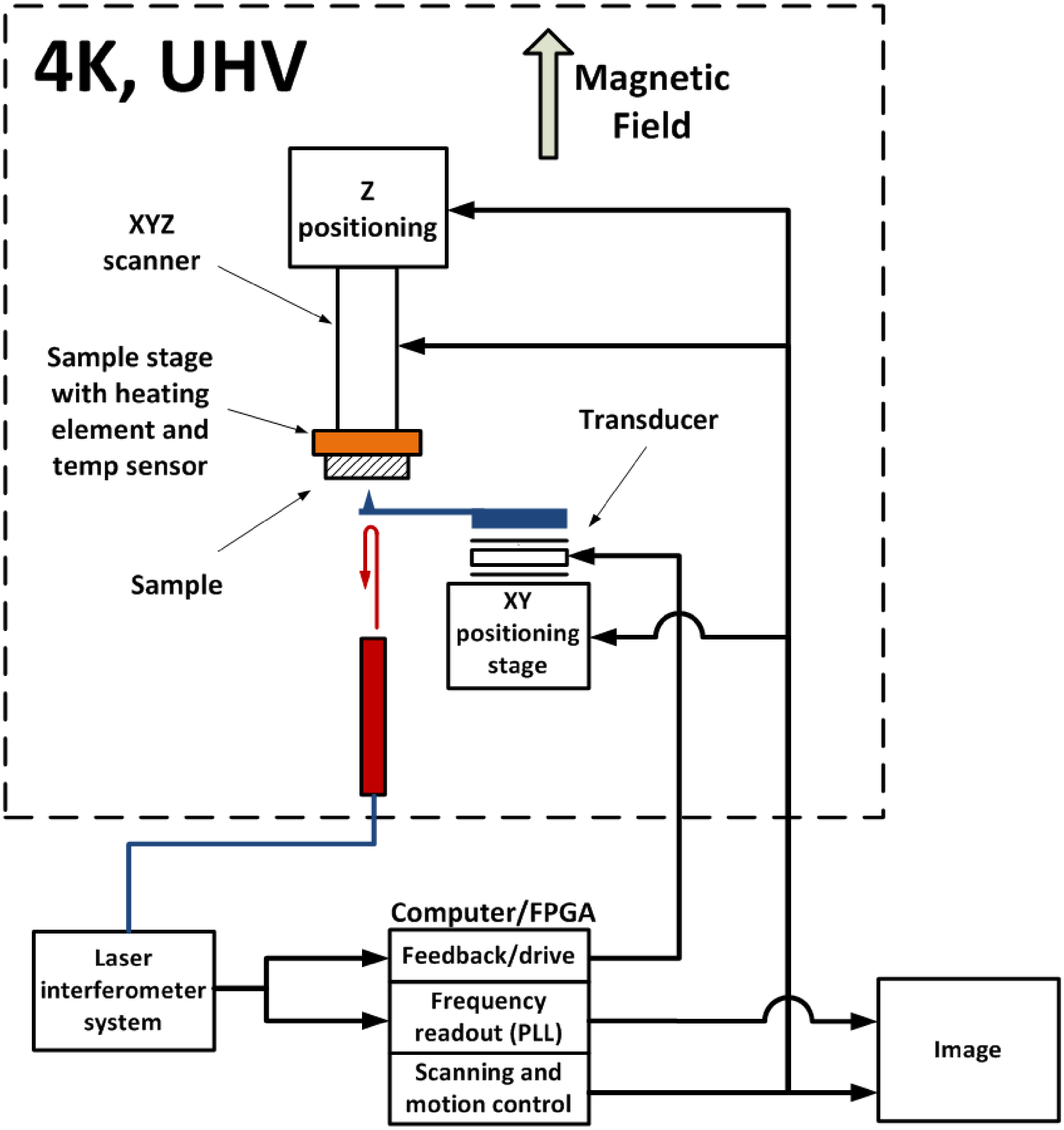

Figure 2.16: Overview of the MFM operation. See Fig. 2.9, Fig. 2.14, and Fig. 2.15 for schematics of individual subsystems.

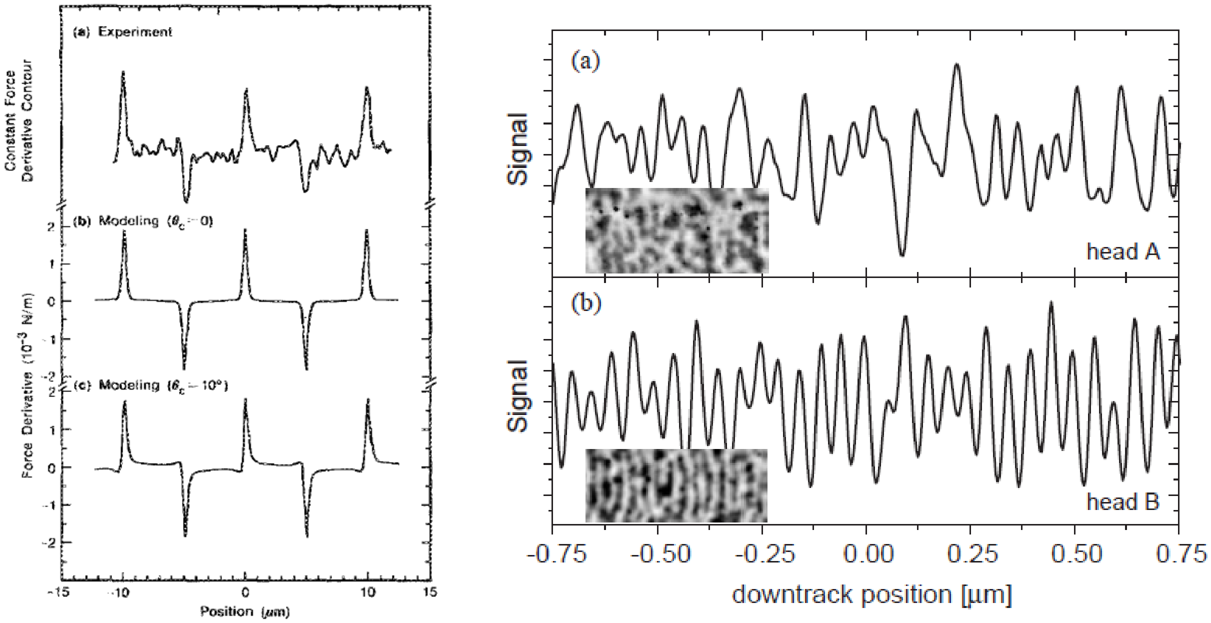

(a) (b)

Figure 2.17: Force gradient of longitudinal recording media (a) [74] and experimental MFM signal from perpendicular recording media (b) [75].

Chapter 3

Sample Preparation and Crystal Lattice Mapping

The Mn_3O_4 samples used in this thesis study were grown as a single crystal by Dr. Min-jung Kim using a floating zone technique at the Frederick Seitz Materials Research Lab of the University of Illinois at Urbana-Champaign (Fig. 3.1). Physically, Mn_3O_4 is a black, insulating, paramagnetic crystal with a tetragonal lattice (space group I41/amd) at room temperature [43].

Figure 3.1: Single crystal Mn_3O_4 grown by Dr. Min-jung Kim [33]. All samples used in this thesis are diced from this crystal. (a) Crystal as grown. (b) A fractured piece with surface normal to [110] mounted on an aluminum holder.

This chapter describes the procedure to produce sample crystals with a smooth, strain-free surface with appropriate surface treatment, and room temperature characterization through electron backscatter diffraction (EBSD).

3.1 Sample Preparation

3.1.1 Polishing

Pieces of single crystal Mn_3O_4 normal to [110] and [1$\bar{1}$0] are identified in a Philips X'pert X-ray diffraction system (Philips/PANalytical Inc, Westborough, MA). They are then diced to appropriate size, approximately $1mm \times 2mm$. Diced crystals are cast into Stycast 1266 (Emerson and Cuming, Billerica, MA). The encapsulated sample is polished using increasingly fine sandpaper (300 grit, 600 grit, 1200 grit, 1500 grit. McMaster, Chicago, IL) then increasingly fine alpha alumina slurry (1μm, 0.3μm, 0.1μm, 0.05μm. Buehler, Lake Bluff, IL). The last step is chemo-mechanical polishing in 0.02μm Buehler MasterPolish slurry to remove surface strain. Encapsulated sample is then thoroughly cleaned in isopropyl alcohol with brief sonication. The polished, encapsulated sample is then sputter coated with 1nm of gold-palladium. This layer serves two purposes: as a charge-dissipating layer and as an adhesion layer for the patterning process to follow.

3.1.2 Patterning

A well polished sample is very smooth and lacks identifying features for location purposes under an SFM or an SEM. To provide both location information and serve as a distance standard, a matrix of location markers were lithographically patterned onto the sample using a standard lift-off process. The encapsulated sample is coated with Poly(methyl methacrylate) resist. The pattern is written into the resist by electron beam lithography using a Raith E-line (Raith USA, Ronkonkoma, NY). 20nm of titanium is then deposited. After a lifted off operation, location markers made of 20nm titanium are left on the surface of the sample. After cleaning the sample, residual Stycast is removed with razor blades. Sample is then mounted onto sample stage using Epotek H20E silver epoxy.

Each location marker matrix is 1mm×1mm in size and contains 100×100 markers, spaced 10μm apart along X and Y axis. Each marker encodes its position within the matrix

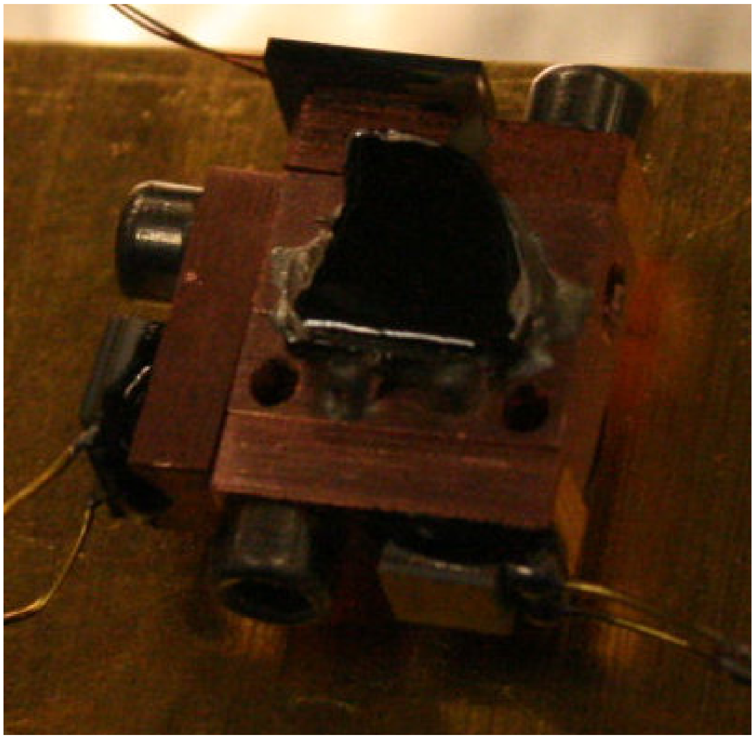

Figure 3.2: Finished [110] orientation sample (black, middle) mounted to sample stage (middle, OFHC copper, red) using silver epoxy H20E. Also attached to the sample stage are Platinum heating element (top) and two temperature sensors (left and bottom). The long edge of the sample stage is 6.35mm long.

(Fig. 3.3), and is visible under both SEM/EBSD and SFM (Fig. 3.3b and Fig. 4.1). Due to the non-magnetic nature of titanium, the marker does not contribute to the magnetic signal. The regular marker interval and regular size make the markers excellent distance calibration. Marker-encoded location information allows correlating magnetic and structural measurements.

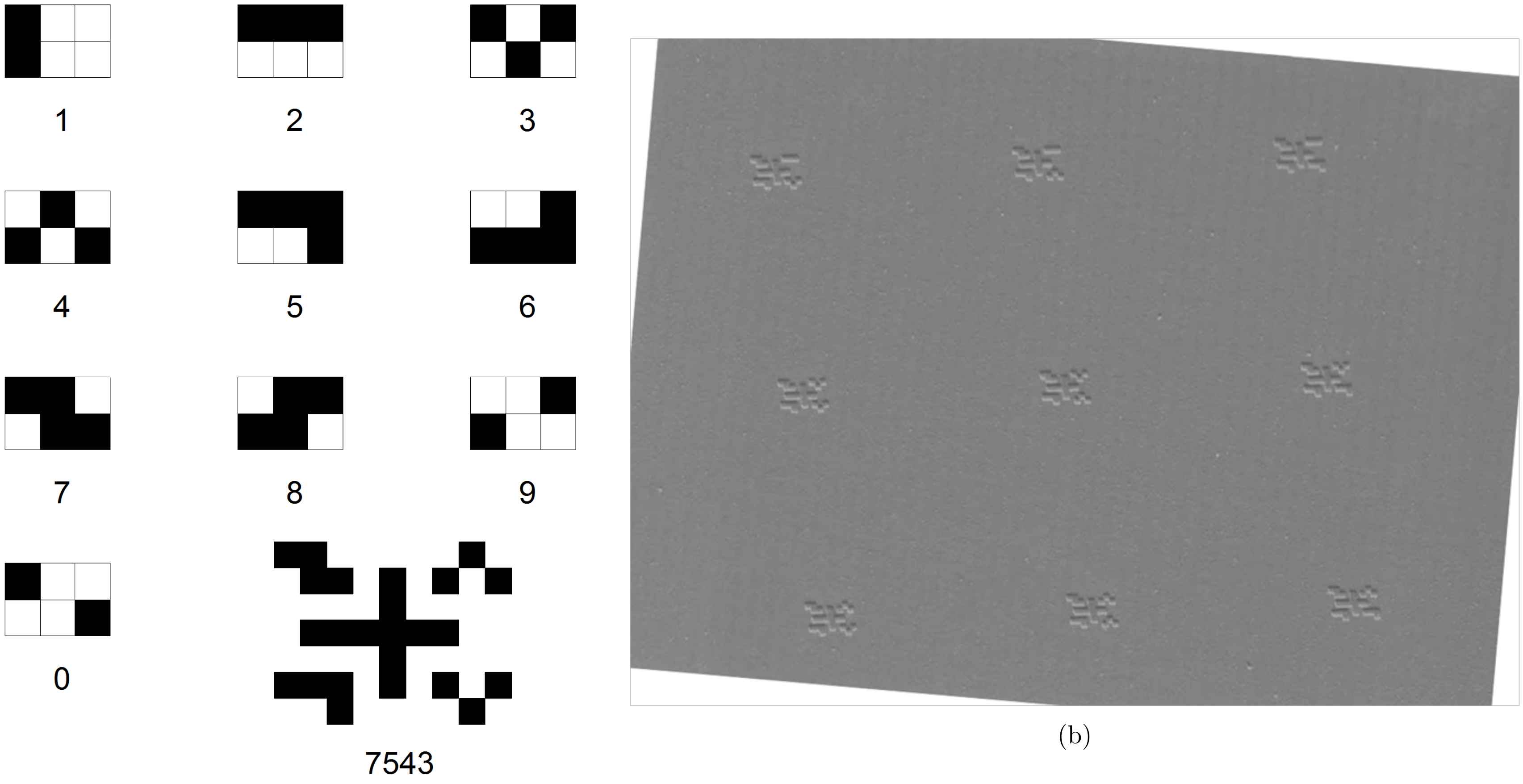

(a)

(b)

Figure 3.3: Location marker system used for sample location indexing. (a) The marker consists of 4 codes lying in the 4 quadrants of a plus sign shape. One arm of the plus sign is elongated to break symmetry. Each code is a 2 × 3 dot matrix (each dot is a 200nm×200nm square) encoding one decimal digit. The marker is read in the order of top left, bottom left, top right and bottom right. The entire marker is $1.8\mu m \times 2\mu m$. Marker 7543 is used as an example. (b) Part of the location marker grid under SEM. Image taken at a tilt of 70° prior to EBSD analysis, and then tilt-compensated. Marker 7543 is on the lower left corner.

3.2 Electron Backscatter Diffraction

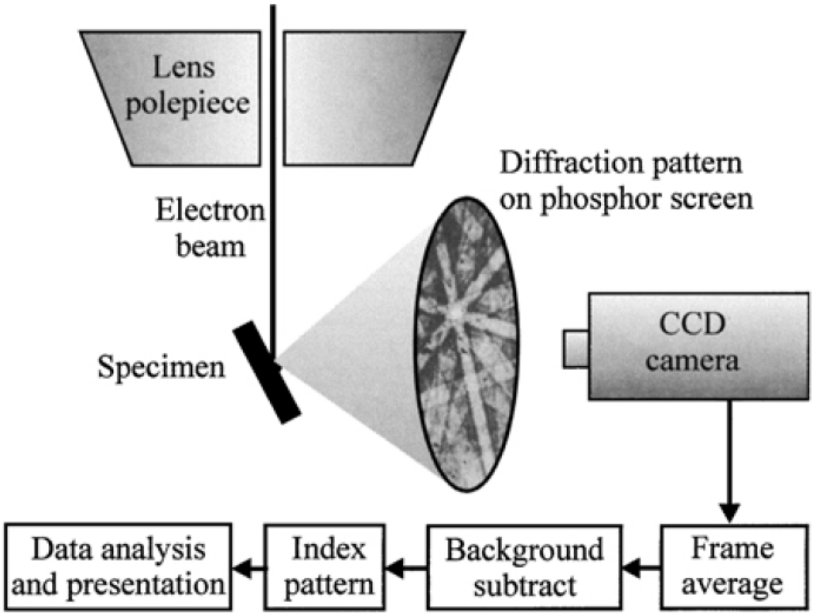

Figure 3.4: Schematic of a typical EBSD setup [77] which correctly represents the JOEL/HKL setup used in this study.

Crystal lattice orientation mapping is often obtained diffraction techniques. Depending on the grain size and requirement for spatial resolution, this is could be done using X-ray diffractometer (XRD), electron backscatter diffraction (EBSD), or transmission electron microscopy (TEM). Commercial X-ray diffraction equipment, such as Philips MRD X'pert, is not sufficient to map the grains in our Mn_3O_4 samples due to its large spot size (often on the order of hundreds of microns to milimeters). Sample preparation for TEM analysis requires thinning the sample to the order of 100nm, which is too small for the grain size of Mn_3O_4, as well as destructive to the magnetic structure. With these considerations we turn to EBSD for grain mapping. Mapping is performed on a JOEL 7000F SEM (JOEL, Japan) with EBSD attachment from HKL (now part of Oxford Instrument, Oxford, UK) (Fig. 3.4).

3.2.1 EBSD Basics

EBSD is carried out on a sample tilted 70° from the horizontal. Incident electrons, usually at 30keV, are diffracted by lattice planes according to the Bragg condition:

$$n\lambda = 2d \sin\theta \tag{3.1}$$

where λ is the wavelength of electron and θ is the diffraction angle. The trajectories of Bragg diffracted electrons for each order n are defined by two cones symmetric to the diffraction plane (Fig. 3.5). Because of the energy associated with the electron beam (a few tens of keV), the Bragg angles are small and the cone angles approach 180°. When these trajectories were intercepted by a flat phosphor screen, these diffracted electron cones illuminate parallel lines, each pair creating the image of a band with bright edges [78] (Fig. 3.6). The collection of multiple electron diffraction bands on the phosphor screen is termed Kikuchi pattern after Seishi Kikuchi [79], unique to the lattice orientation of the sample. This pattern is collected by a camera and stored for computerized orientation indexing. A grain map is produced by rastering the electron beam and indexing the lattice orientation of an array of positions.

Spatial resolution of EBSD grain mapping is limited mostly by the activation volume in the sample by incoming electron beam [78]. Mn_3O_4 is an insulator that usually produce significant charging under SEM. The gold-palladium layer generally eliminates charging problem, but at the same time also blurs the Kikuchi patterns produced by sample proper. Higher beam energies were therefore favored for higher contrast in the Kikuchi pattern. The activation volume of this high energy electron beam limits the spatial resolution on Mn_3O_4 samples to appromiately 200nm. A well polished sample produces grain maps with more than 95% of the pixels indexed with high confidence.

EBSD mapping produces a few undesirable effects on the sample due to the high energy electron beam. Foremost is the disruption of lattice integrity close to the surface after extensive beam dwell time. This could be observed through worsening of Kikuchi patterns

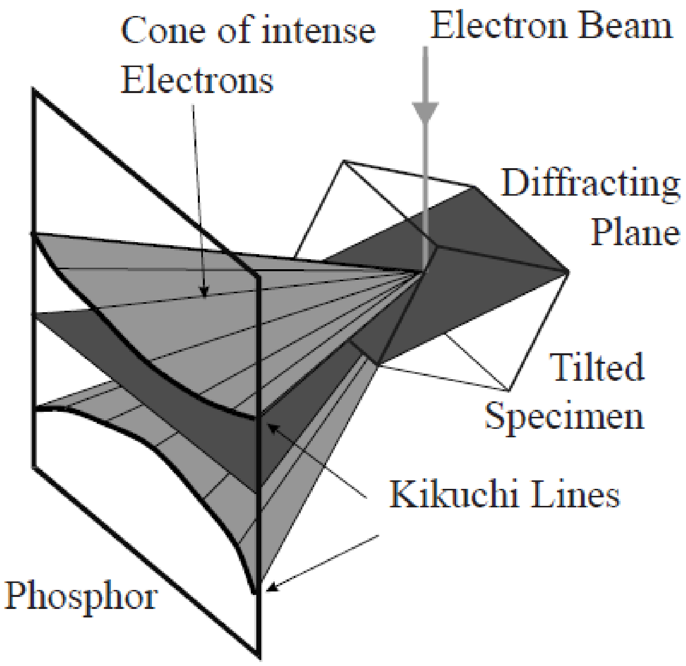

Figure 3.5: Kikuchi band formation from electrons Bragg diffracted by lattice planes [78].

and a lack of magnetic signal in LT-MFM. The carbon deposition from the electron beam also introduces unwanted topographic signal in SFM.

Samples used in this thesis have either [110] axis or [001] axis normal to sample surface in majority of the grains. Due to the symmetry at room temperature, [110] and [$1\bar{1}0$] lattice directions are indistinguishable. Low temperature Raman scattering is performed by Dr. Min-jung Kim to differentiate between the two orientations on a percentage basis. The general grain characteristics are presented below, while detailed EBSD mapping near MFM scan area is presented together with the MFM results in the next chapter. The lattice directions always refer to tetragonal lattice directions.

3.2.2 Grain Characteristics of [110] samples

The [110] sample is predominantly occupied by two twinned orientations (Fig. 3.8), in an approximately 1:1 mix. Grains of these orientations are generally long alternating stripes, with wide ranging dimensions: length ranging from microns to hundreds of microns, and

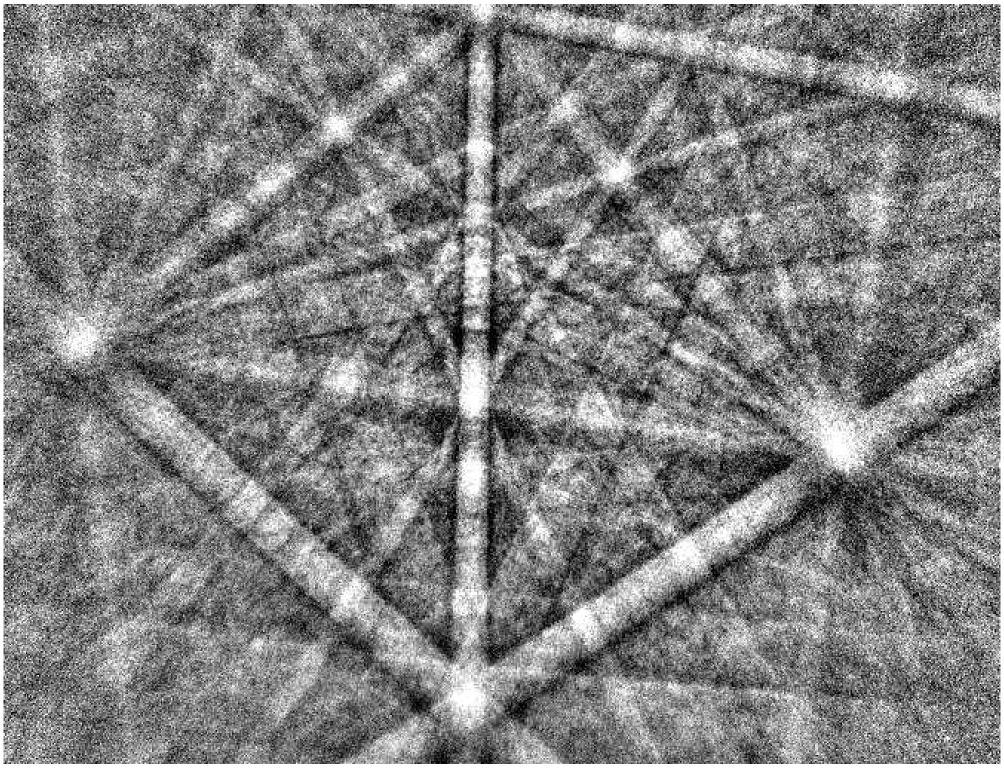

Figure 3.6: Kikuchi patterned generated by Mn_3O_4 (tetragonal lattice, [110] lattice direction normal to sample surface).

widths from hundreds of nanometers to tens of microns. The [110] axes of thse two major orientations have a 7° misalignment with the surface normal. The misalignment between the two orientations is approximately 83°.

3.2.3 Grain Characteristics of [001] samples

The [001] sample is a 2:1 mix of [001] grains and $[1\bar{1}0]$ grains. The grain shape is varied, unlike the [110] sample. Misorientation between neighboring grains is approximately 83°. Because of the symmetry at room temperature, there is ambiguity between ±[100] and ±[010], as thus $[1\bar{1}0]$ grains are identified as [110] in EBSD. Separate Raman measurement by Dr Min-jung Kim indicates vast majority of the non-[001] grains are $[1\bar{1}0]$.

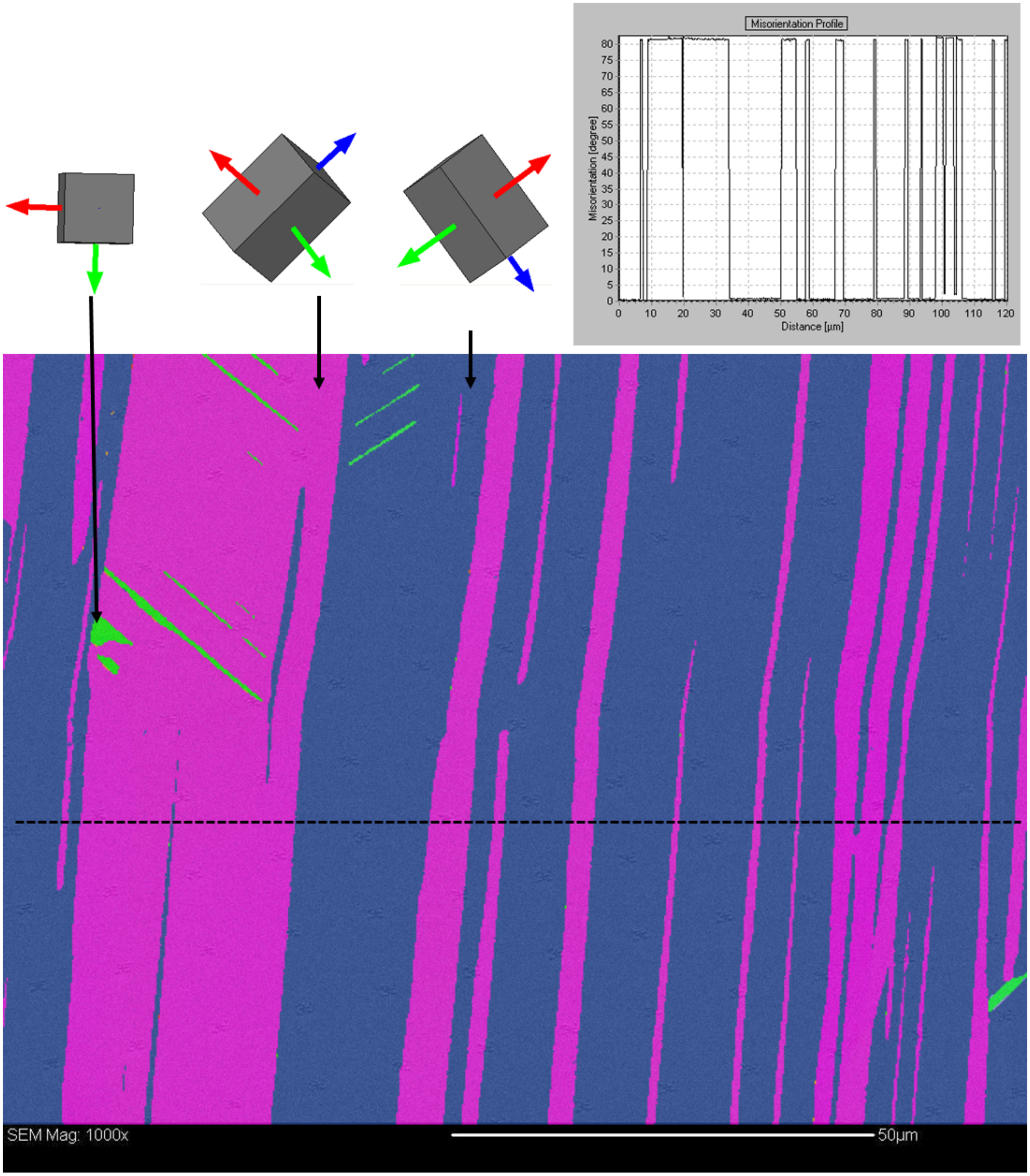

Figure 3.7: Grain map of [110] sample showing the grain structure in a ∼1mm×1mm square. Grain map is overlaid onto an SEM image. Lattice orientation is indicated by a 3D representation of the tetragonal lattice unit cell, with arrows indicating lattice directions (Red arrow: [100]. Green arrow:[010]. Blue arrow:[001]). Two of the orientations have [110] axis aligned with surface normal. A small portion of the sample are [001] grains, and are colored green. Misorientation profile across the dashed line is plotted to show the misorientation between the two major orientations.

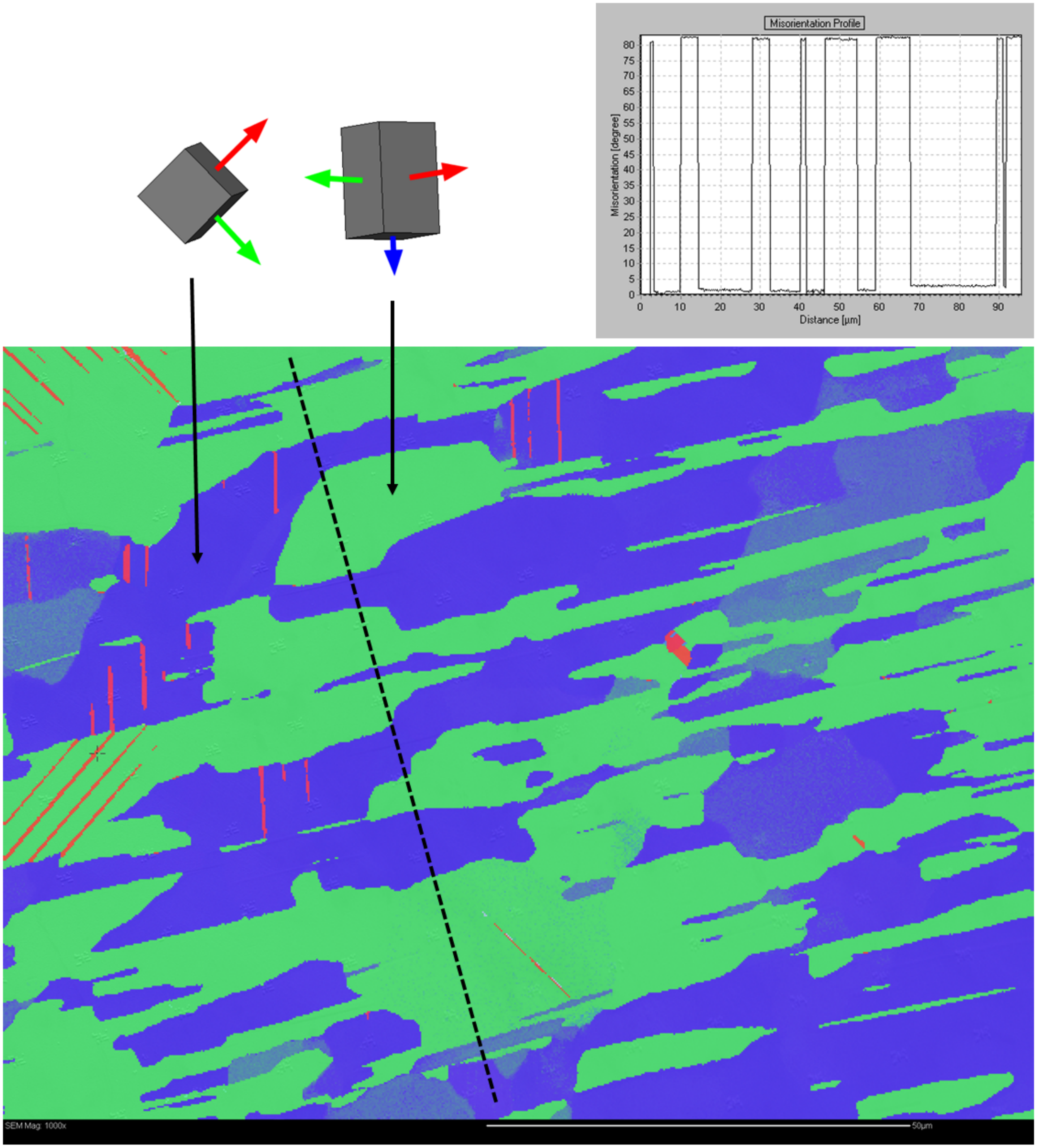

Figure 3.8: Grain map of [001] sample showing grain structure in a ∼1mm×1mm square. Grain map is overlaid onto an SEM image. Lattice orientation is indicated by a 3D representation of the tetragonal lattice unit cell (Red arrow: ±[100]. Green arrow:±[010]. Blue arrow:±[001]). Two major orientations have either [001] or $[1\bar{1}0]$ axis aligned with surface normal with 11.5° deviation. Misorientation profile across the dashed line is plotted to show the misorientation between the two major orientations.

Chapter 4

Magnetic Imaging of Mn_3O_4 Samples

Experimental observations are grouped by crystallographic orientations of the samples. In all cases, the external magnetic field is applied normal to sample surface. The magnetic probe is also magnetized along the same direction. The images of [110] samples—that is, samples with surface normal along [110] tetragonal lattice direction—are colored in a red-white-blue color scale (red=negative frequency shift, white=no frequency shift, blue=positive frequency shift) as the signal can be easily interpreted (see discussion in Sec. 2.3.5). The rest of the images are colored in a blue color scale. Temperature and magnetic field changes are both performed in a smooth ramp profile and at a slow rate ($\leq$ 2K/min cooling and $\leq$ 100G/s respectively).

4.1 [110] Samples

4.1.1 Magnetic Pattern Fformation in Zero Field Cool

In absence of any magnetic field, Mn_3O_4 is a paramagnet above T_N. All measurement sequences in this thesis study begin at a temperature well above T_N (typically 55K at fields less than 10kG, and 70K at higher fields) to remove any hysteretic effects. In this sample state, the LT-MFM operates as an AFM and produces topographical image. Frequency of the cantilever decreases in a roughly exponential manner as the tip approaches sample surface. Scanning the sample at a distance of approximately 140nm, the frequency shift over the entire scan area (with z-axis planar tilt compensation) is generally less than 0.5Hz peak to peak, indicating that outside location markers and occasional residual particles, the sample is highly smooth and flat, in agreement with the SEM images (see Fig. 3.3b). The average frequency of the topographic scan, excluding the marker region, is used as the baseline frequency in subsequent magnetic images of [110] sample because it represents the state of the probe in absence of any magnetic interactions.

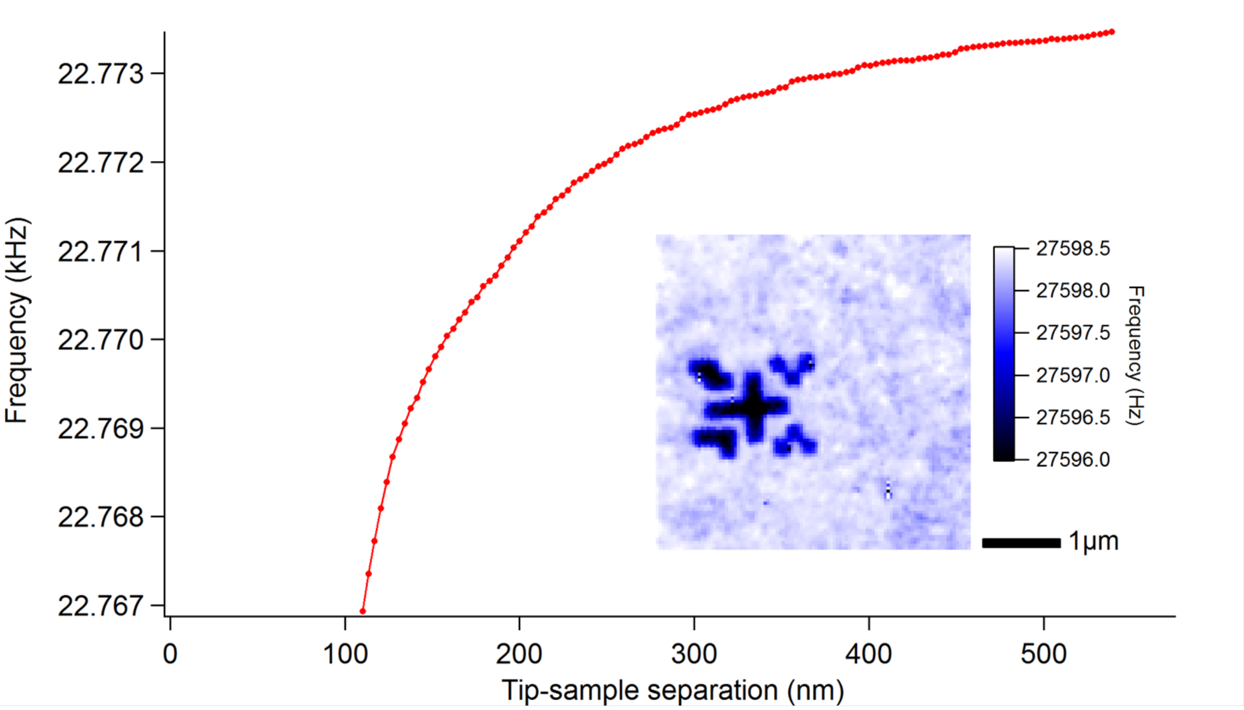

Figure 4.1: Behavior of the probe as AFM, when the sample is above T_N (paramagnetic). Variation of cantilever frequency with respect to tip-surface distance is approximately exponential. Inset: AFM scan of location marker 7534 at 48K.

Upon cooling below T_N, frequency shift begins to bifurcate into positive shift and negative regions (Fig. 4.2). Although a large number of locations were imaged, we will focus on a few locations to demonstrate representative behaviors. In this temperature range, Mn_3O_4 is ferrimagnetic with net magnetic moment normal to sample surface. Due to symmetry, magnetic moment can be either into the surface or out of the surface. The frequency shift as the result of these possible moment vectors are either positive (probe moment and local sample moment are parallel) or negative (antiparallel) [44]. The positive and negative frequency shift regions shown in the magnetic image therefore correspond to magnetic domains of respective magnetization directions. The magnetic domains begin to develop almost immediately below T_N and with spatial variation, persist down to base temperature (4K).

At approximately 27K, stripe features are observed in domains of both polarities. Two distinct stripe orientations are present, even though stripe orientations and domain polarity do not have appreciable correlation. Cross-section of magnetic images reveal that the stripes are modulations on top of the plateau profile of the domains. The stripe pitch varies from tens of nanometers (and possibly smaller, below the spatial resolution of our probe) to hundres of nanometers. Their lengths are not very well defined in ZFC due to the domain boundary crossing the zero-frequency shift level, effectively negating any observable stripe behavior in the neighboring regions. Stripes persist in zero field to base temperature.

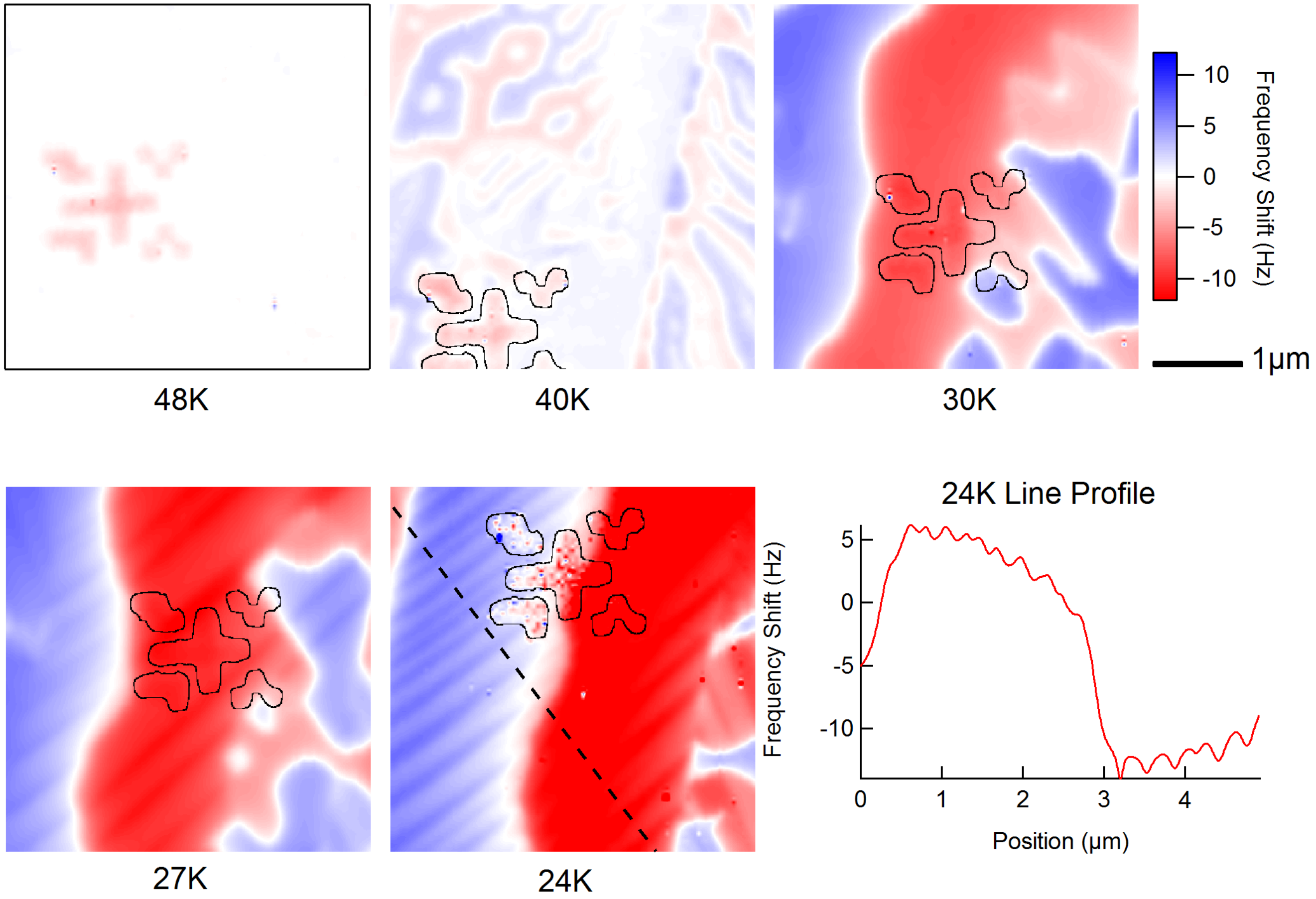

Figure 4.2: Zero field cool sequence of [110] sample, near marke 7534. The marker is outlined in black. Image at 48K is framed in black to separate it from white background. All images share the same color scale. Average frequency from 48K image outside the marker is used as frequency baseline and images are colored according to shifts away from the baseline. In the line profile, magnetic domains correspond to step-like regions of frequency shift, with stripe features modulating in addition to the domain signal.

Side by side comparison between scans taken at different tip-sample distances indicates that frequency shift due to sample surface topography is a much shorter ranged effect than the magnetic interactions (Fig. 4.3). The titanium location markers, which are 20nm thick, become invisible when a second scan is taken at ∼20nm higher, while stripes and magnetic domains remain visible with a small penalty to signal to noise ratio. This confirms that the stripes are magnetic in nature and are not the topographic effect of surface rippling.

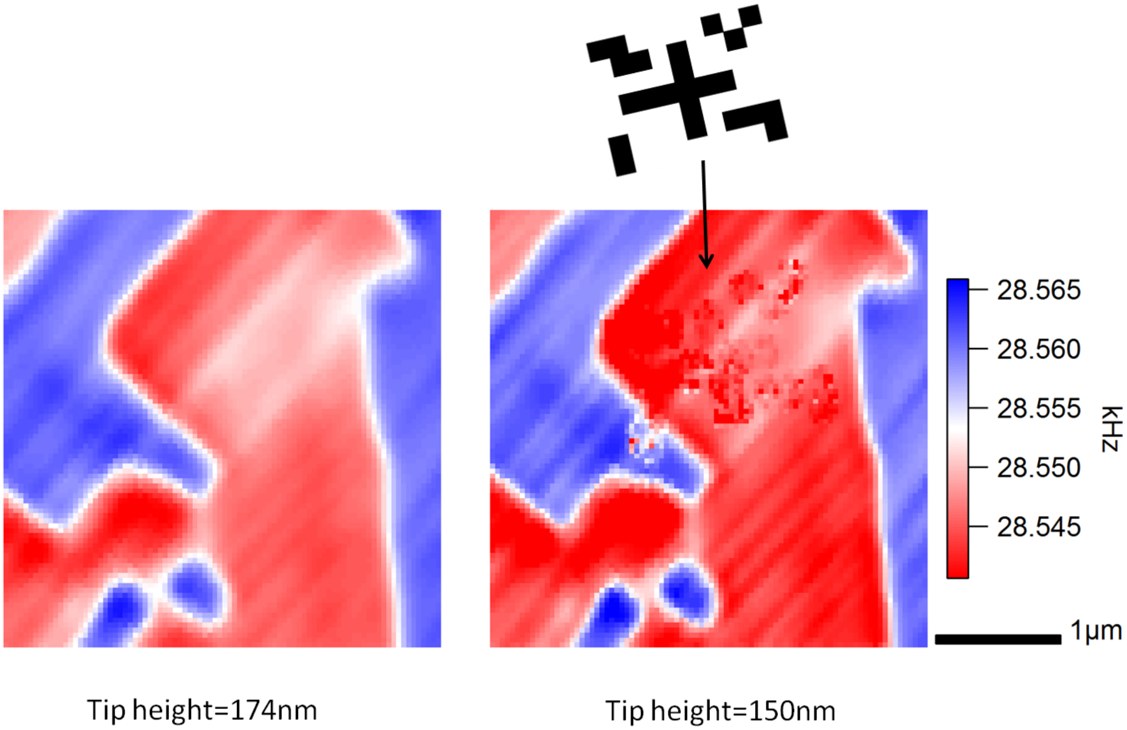

Figure 4.3: Scanning the sample at different tip-sample distances. Response of the LT-MFM to topographical variations (in this case, a location marker) is much shorter ranged than the magnetic signals.

4.1.2 Magnetic Pattern Formation in Field Cool

Stripes can be better observed when the sample is cooled in a small magnetic field, applied normal to sample surface, thus parallel to [110] lattice direction (Fig. 4.4). The presence of magnetic field breaks symmetry to produce a single magnetic domain over the entire sample. As most of the sample-probe interaction occurs at the very tip of the probe, the background moment, as well as the static magnetic field, produces a static background and does not affect the magnetic contrast. The absence of "plateau" frequency shift from the domains and the removal of domain transitions increase signal contrast for stripes significantly, allowing the stripe onset to be observed with greater detail.

In field cool, the stripes eventually developed into a "tweed" pattern, with parallel stripes of two known orientations occupying mutually exclusive regions on the sample surface. Immediately below T_2, the magnetic stripes predominantly nucleate from the boundaries between regions of uniform orientation, then grow in length and density as temperature decreases. Magnetic stripe pattern run diagonally across each region, meeting stripes in the neighboring regions at approximately 83°. Stripes in [110] samples appear to be sinusoidal modulations of cantilever frequency, consistent with signal resulting from perpendicular magnetized sample moment.

Overlaying magnetic image with EBSD grain map using the location marker confirms that the stripe orientations are confined by grain boundaries. Within each grain, stripes follow one of the two major orientations (Fig. 4.5). When compared to the room temperature lattice axes vectors, in grains wider than ∼500nm, stripes are 7° off the [001] lattice direction. This applies only to field cooled images—zero field cooled stripes are in good agreement with [001] lattice direction. Narrower grains show larger variation of stripe angles—possibly due to increased strain as well as stronger boundary effects. The magnetic modulation occurs along the $[1\bar{1}0]$ lattice direction. At boundaries between grains of this size group, stripes meet at ∼83°, coinciding with the lattice misorientation and confirming that the stripes are directly related to the crystalline structure.

Stripes have been observed in vast majority of the grains imaged. In narrow grains less than 500nm wide, the stripes become densely packed and in some cases smoothed over due to spatial resolution limitations. Stripes have been found to extend across the widest grain observed, at 9μm wide (Fig. 4.6). The width of the grain is more than an order of magnitude larger than the stripe pitch (≤400nm in this grain). Stripes can also be seen to develop in the middle of the grain, away from any boundaries. We therefore believe the stripes are not merely a boundary effect, although they seem indeed affected by boundary conditions (as evidenced by the growth of stripes out of grain boundaries commonly observed).

While isolated stripes exist (see Fig. 4.7), most grains have regularly spaced stripes. Stripe pitch generally increases with grain size, reaching a maximum at approximately ∼500nm pitch size. Smaller grains have pitches reaching at or below probe resolution of 70nm.

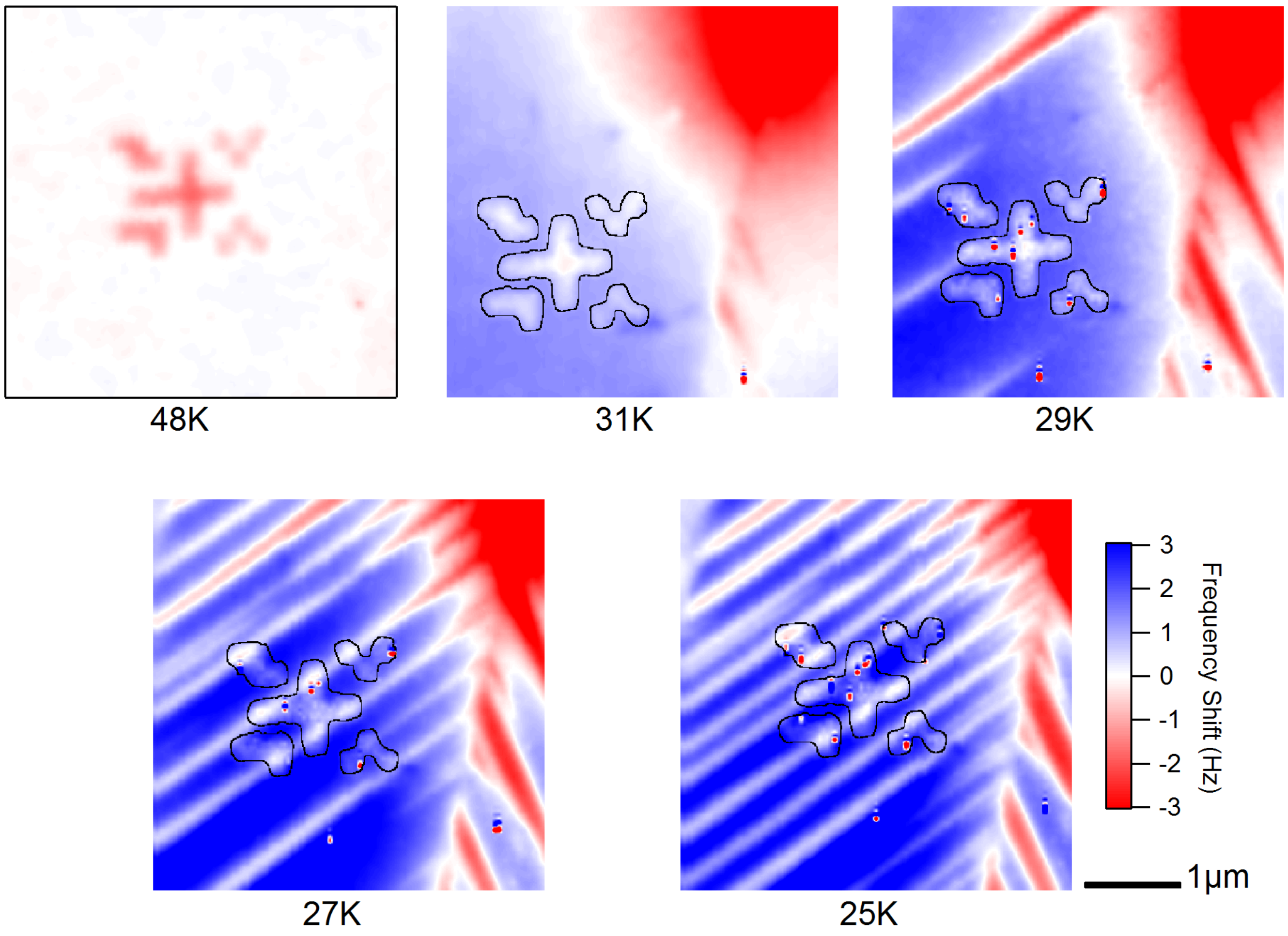

Figure 4.4: Field cool sequence of [110] sample near marke 7534 in 1500G magnetic field. Magnetic field is normal to sample surface and parallel to [110] lattice direction Stripes are seen nucleating from well-defined boundaries soon after T_2.

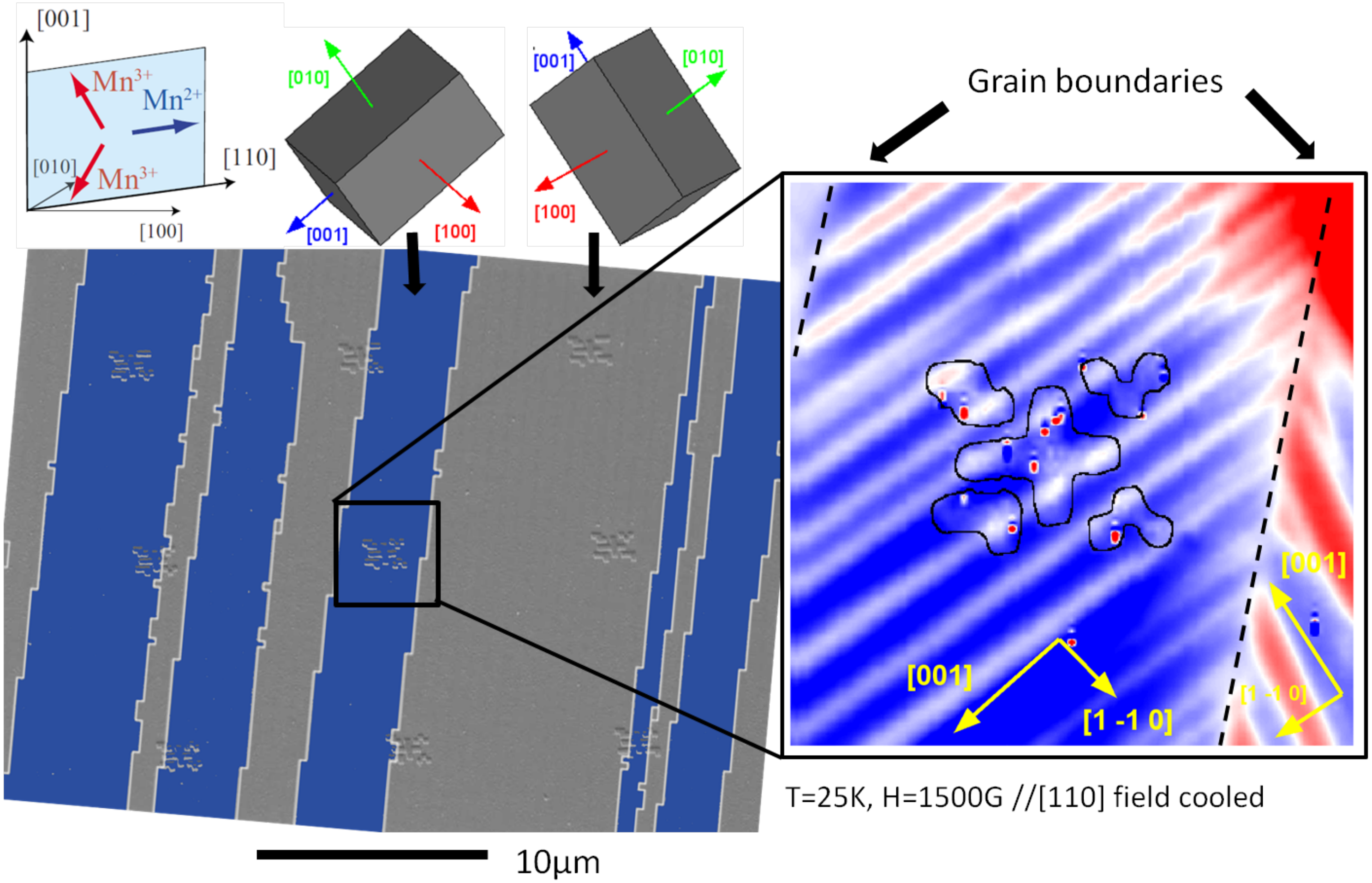

Figure 4.5: Relationship between stripe patterns and the lattice structure in [110] sample. Lattice directions are illustrated in yellow in the MFM image. Grain boundaries in MFM image are highlighed by dashed lines. Unit cell illustration of the lattice orientation is included, as well as the spin orientation in the ferrimagnetic phase [28]. At this temperature and field, the system is in commensurate ordered phase. Mn^{2+} spins align with [110] direction and Mn^{3+} spins are pairwise canted away from -[110] direction, with a net moment antiparallel to the Mn^{2+} spins.

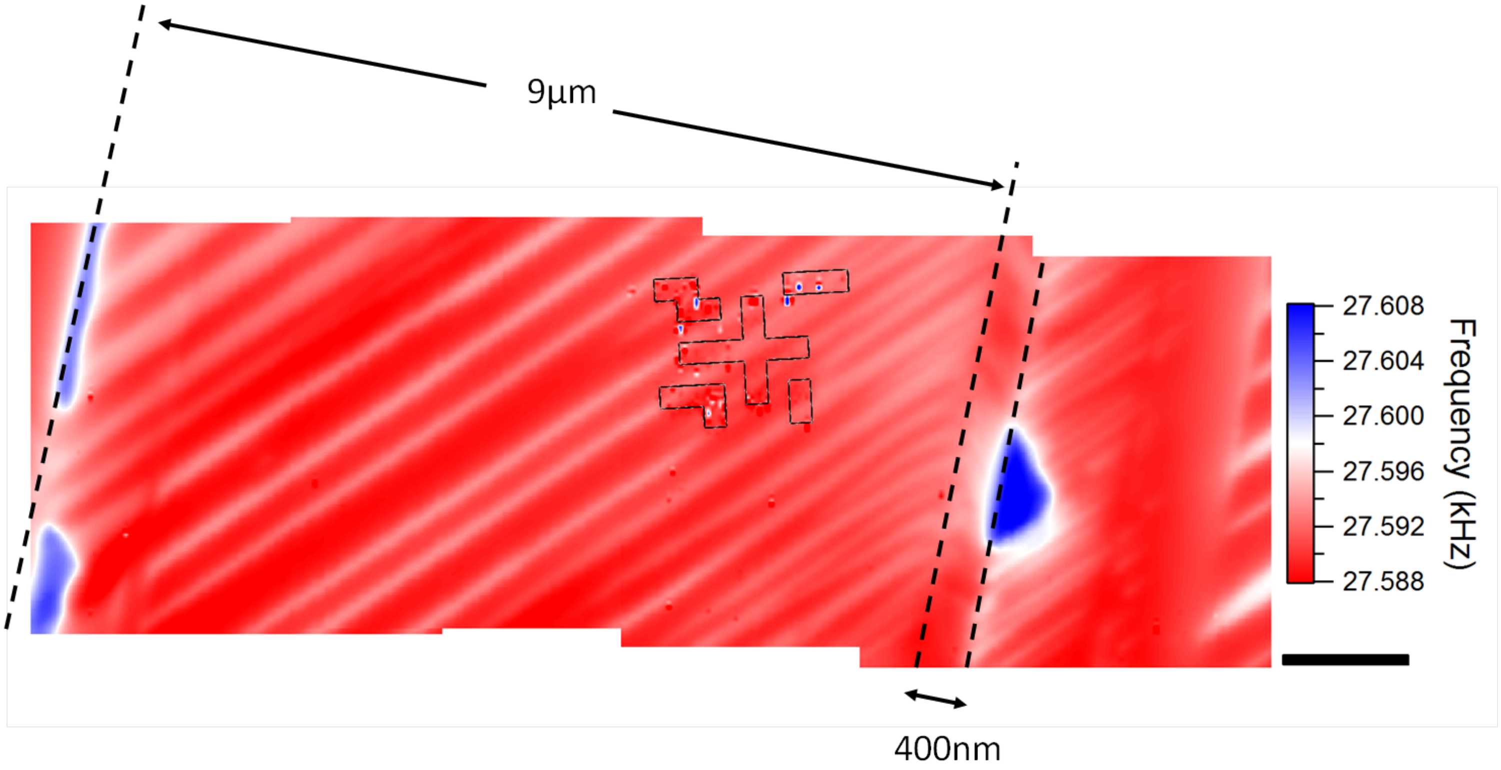

Figure 4.6: An area scan of [110] sample around marker 7521 (marker is outlined in black), after being cooled to 10K in 1000G field along [110] lattice direction. Black scale bar is 1μm. Stripes are present throughout the wide grain. The narrow grain show hints of stripes not resolved due to probe size limitations. The narrowest stripe resolved has a full width half max of 70nm.

4.1.3 Pattern Onset by Field and Variations of Stripe Orientation

It has been shown in [32] that the transition at T_2 between incommensurate and commensurate state can be driven by magnetic field isothermally. It is therefore illustrative to examine whether the stripe pattern is also responsive to field change (Fig. 4.7). Sample is first zero field cooled to 30K, at this temperature no stripes are visible in the scanned area. The stripe pattern is induced by ramping magnetic field up while maintaining temperature at 30K[1]. Onset of significant stripe development is observed between 900G and 1000G field in some grains, while the other grains show very few stripes. At 1500G, the resulting stripe pattern is significantly different from the result in field cooled sequence in the same field (Fig. 4.4).

Interesting effects are observed as the field is ramping down (Fig. 4.8). Stripes remained until 200G (see line profile in Fig. 4.8), indicating significant hysteresis even at this low field. More intriguing is the fact that fresh stripes appears on the down ramp around 1100G, as an apparent division pushed from lower left to the upper right of the field of view. Strikingly, the stripes within the same grain are at different angles (see scan at 1100G) across this division, with a differential angle of ∼5°.

The same effect is observed during field ramp at 18K (Up ramp, Fig. 4.9 and down ramp Fig. 4.9). Magnetic stripes and domains are both present at 18K in zero field. The stripe angle differential (∼6°) is present across domain boundary at 300G as field is ramped up. Although the magnetic domains (plateau frequency shift) were eliminated by 1600G, the stripe angle division (for lack of a better term) remained until 2000G field. On field ramp down from 2000G, angle division wall movement is clearly observed. The angle division wall did not coincide with the domain walls that was present in the up ramp. The entire scan area remained as a single magnetic domain after the ramp down.

---

[1] All subsequent "field ramp" measurement sequences follow this protocol: sample is zero field cooled first, followed by ramping the field in constant temperature.

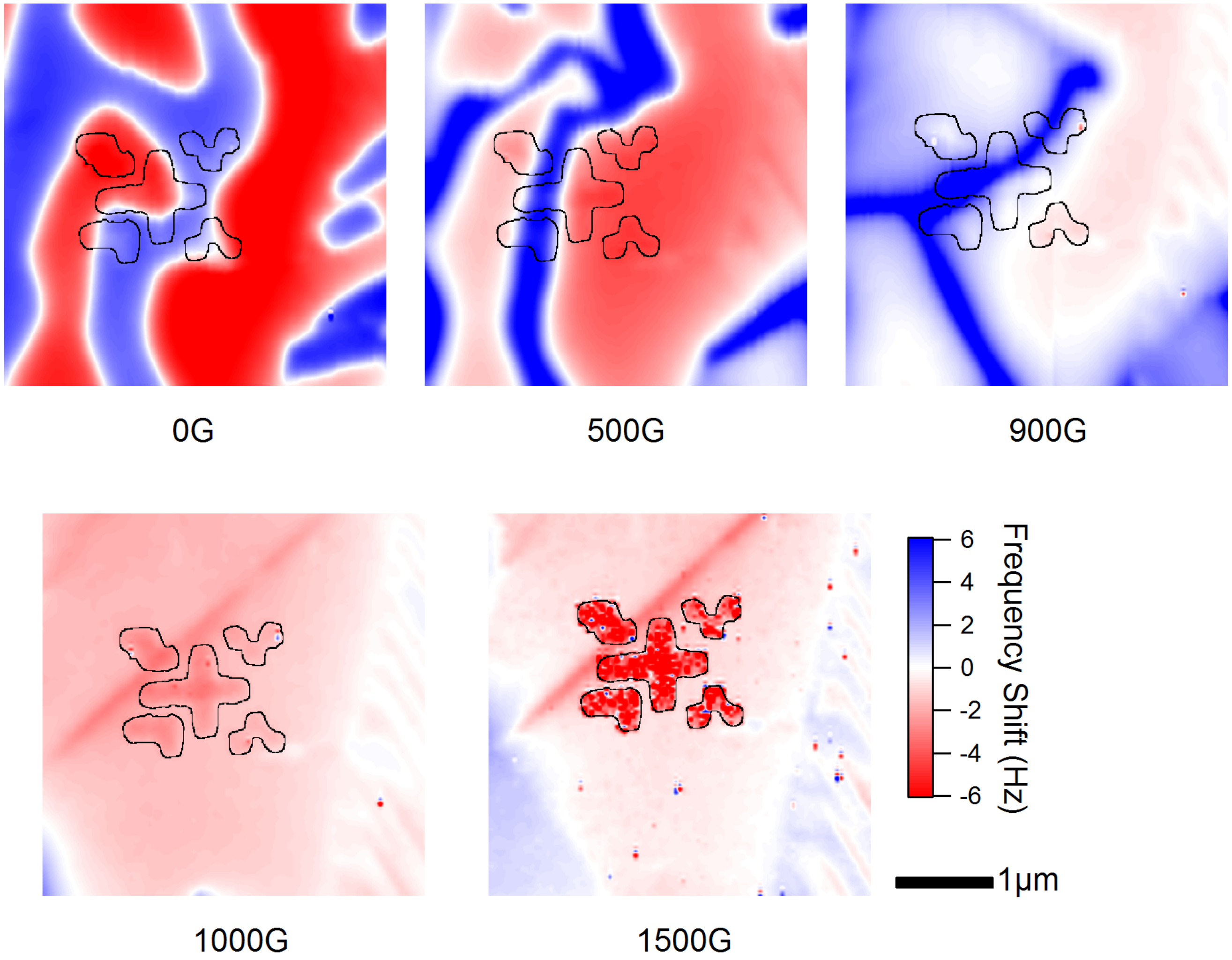

Figure 4.7: Pattern onset driven by magnetic field at 30K in [110] sample. Sample is first zero field cooled to 30K. Then the field is ramped up to 1500G. The grain to the right of the scan area show regularly spaced stripes, while the grain in the middle has only isolated stripes after reaching the final field.

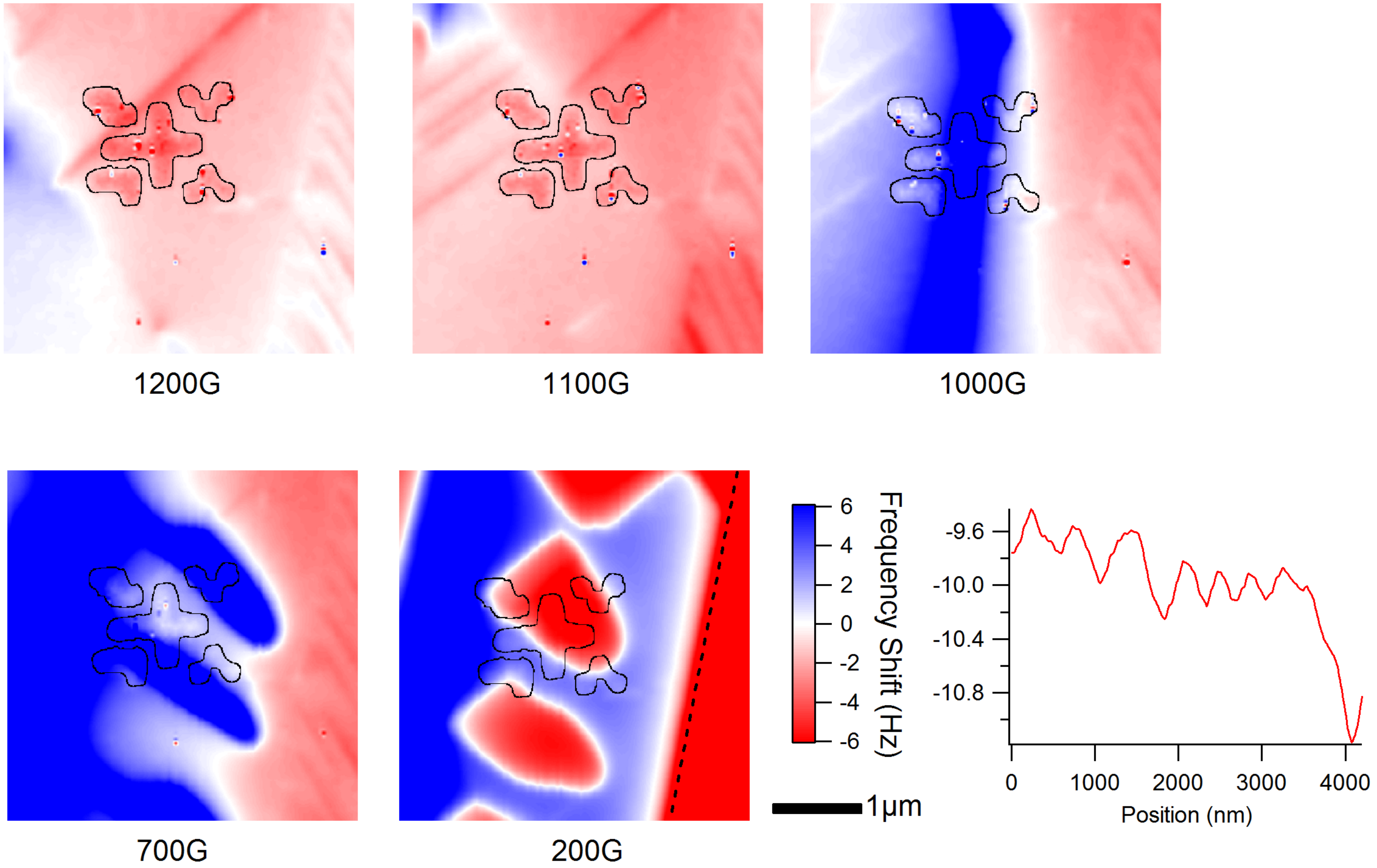

Figure 4.8: Field ramp down from 1500G, in [110] sample at 30K, near marker 7534. Immediately following Fig. 4.7, magnetic field is ramped down to zero slowly at 30K. Interesting formation of isolated stripes around 1100G, accompanied by an apparent boundary of unknown origin running diagonally across from top left to bottom right of the view. A line profile is taken at zero field along the dashed line to show the stripes that, due to high contrast, are hardly visible.

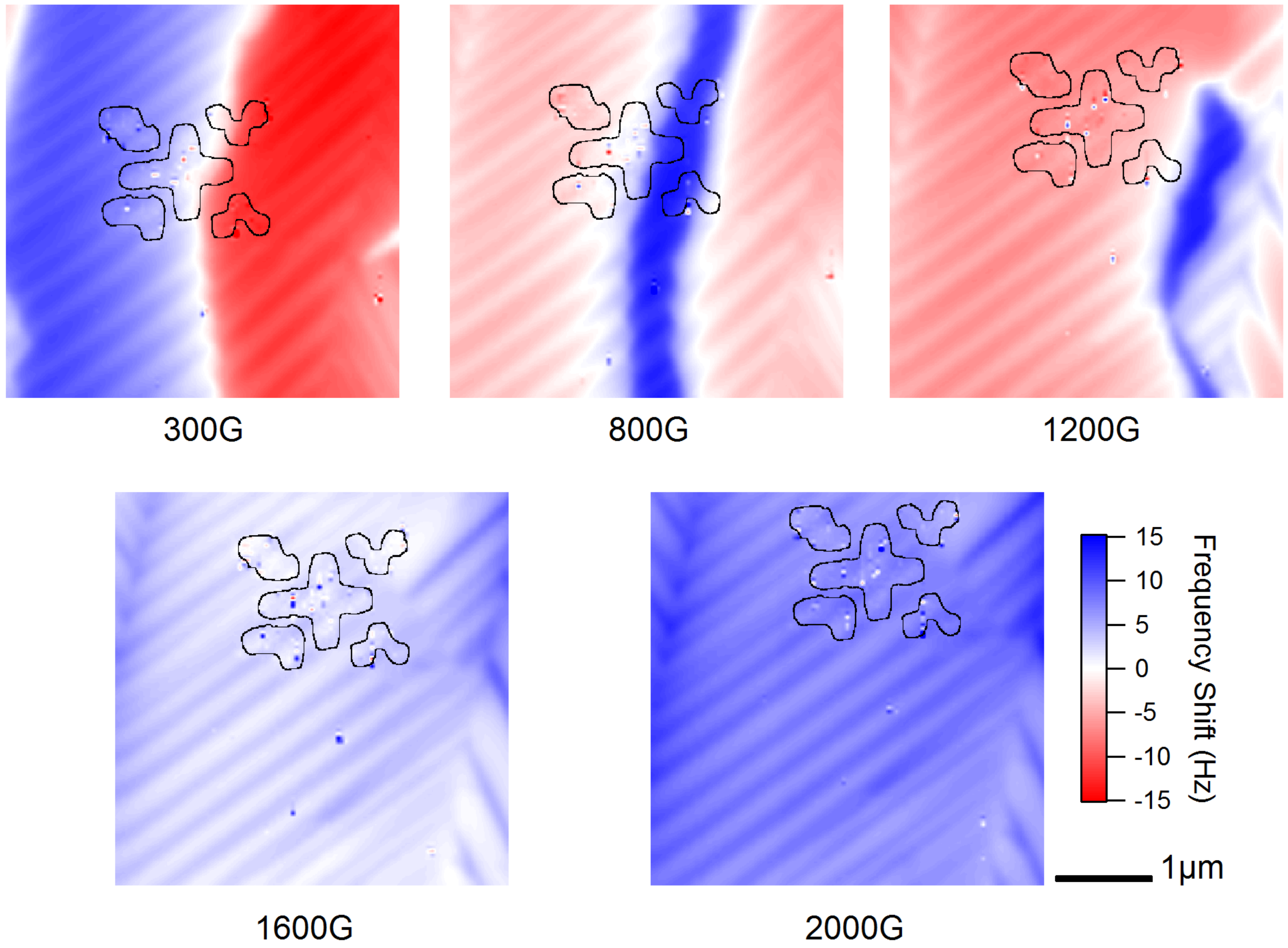

Figure 4.9: Stripe orientation variation driven by magnetic field at 18K in [110] sample, near marker 7534. The high frequency shift domain (blue) in 300G scan shrinks in size as field is ramped up, resulting in the bright band visible in 800G. The middle grain is separated by this bright band. The stripes on the left half of the grain and those on the right half are not at the same angle (~34.5° vs ~39.5°. The two stripe angles remain separate, although the spatial distribution varies as field changes.

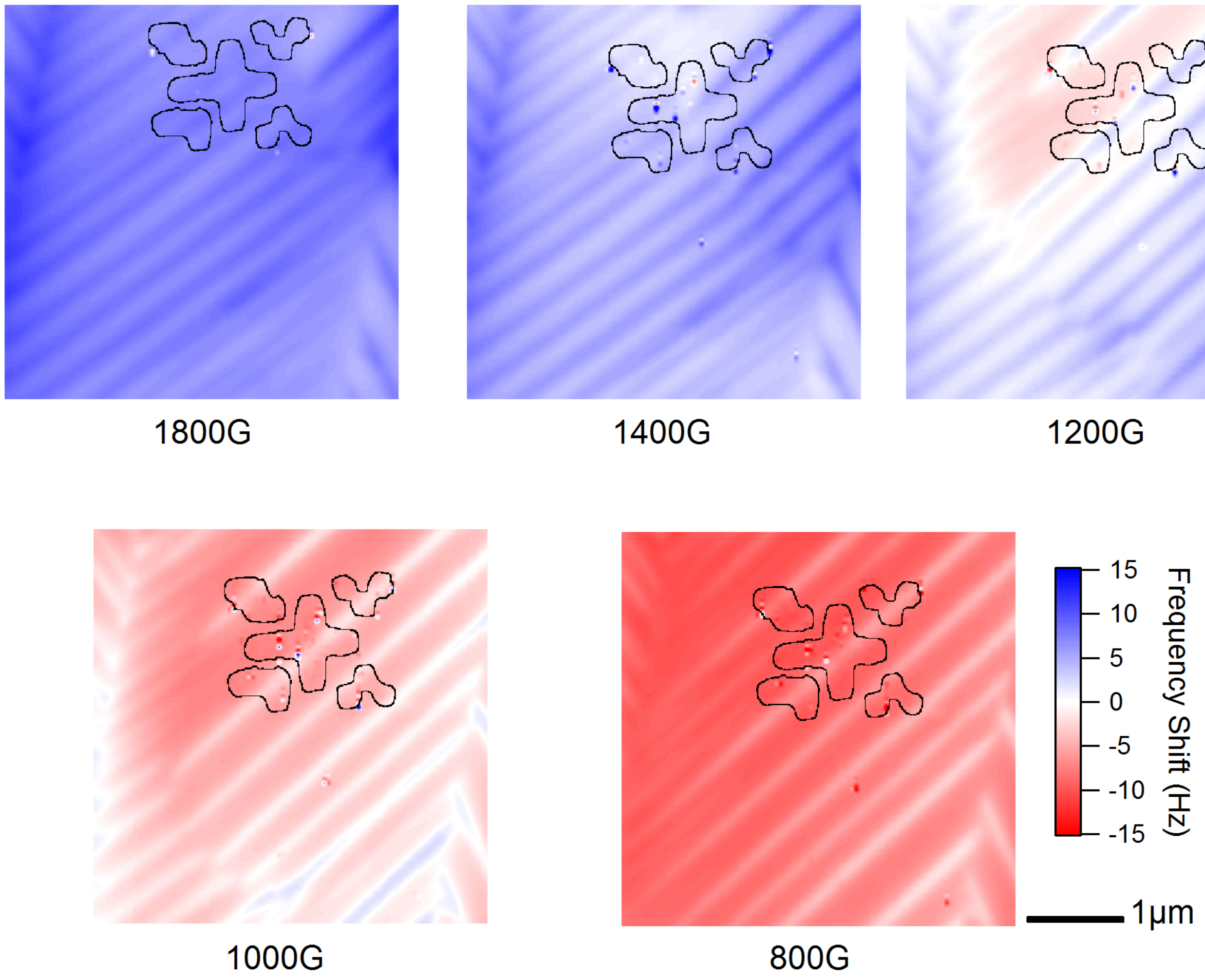

Figure 4.10: Field ramp down from 2000G, in [110] sample at 18K, near marker 7534. Immediately following Fig. 4.9, during field down sweep, the two “angle regions” show distinct boundary within the same grain. Between 1200G and 800G, the entire scan area transformed from overall positive frequency shift to overall negative frequency shift without breaking into magnetic domains. The scan are remained as such from 800G down to zero field.

4.1.4 Pattern Onset and Elimination by Cooling

Stripe onset by ZFC or FC of [110] sample is summarized in Fig. 4.11. The onset occurs right after T_2 with a slight increase at higher fields.

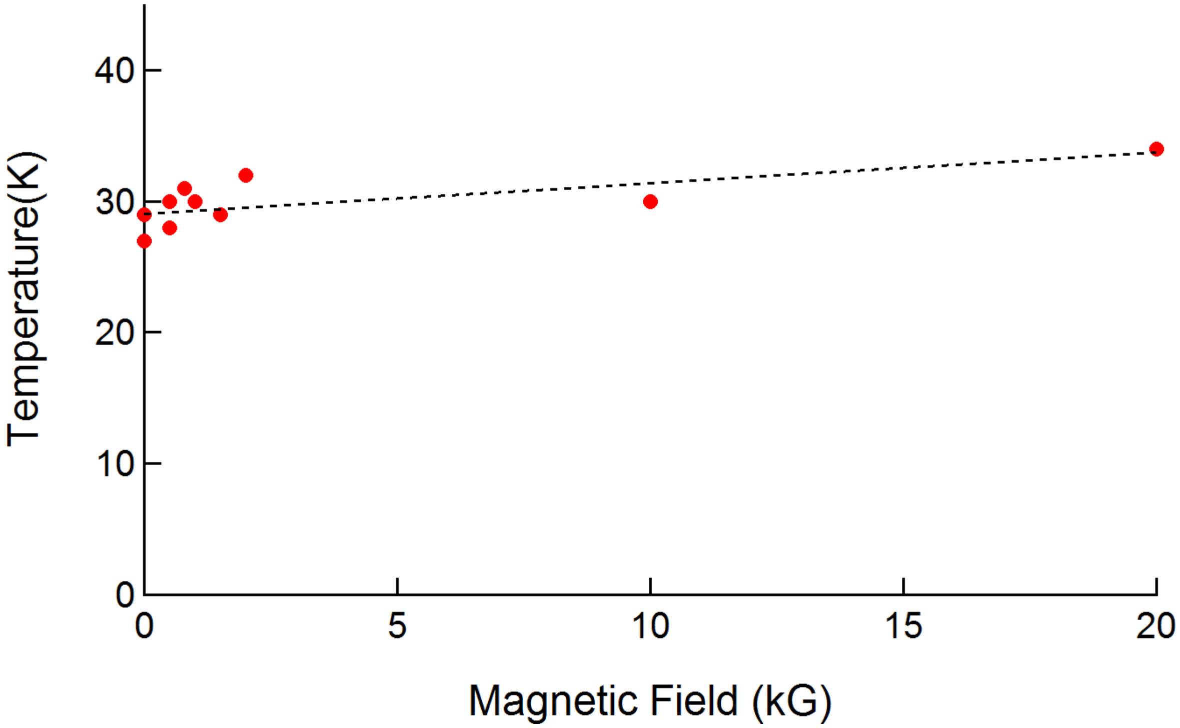

Figure 4.11: Stripe pattern onset temperature, as a function of field, when [110] sample is cooled. Dashed line is the best linear fit.

When the sample is field cooled in small fields, the stripe patterns persist down to base temperature (4K). However, cooling the sample at higher fields reveal that the stripes can be eliminated. In 20kG field cool sequence (Fig. 4.12), stripes appeared briefly near 34K. Stripe signal becomes weaker as temperature decreases below 31K. At 20K, only topographical features are present.

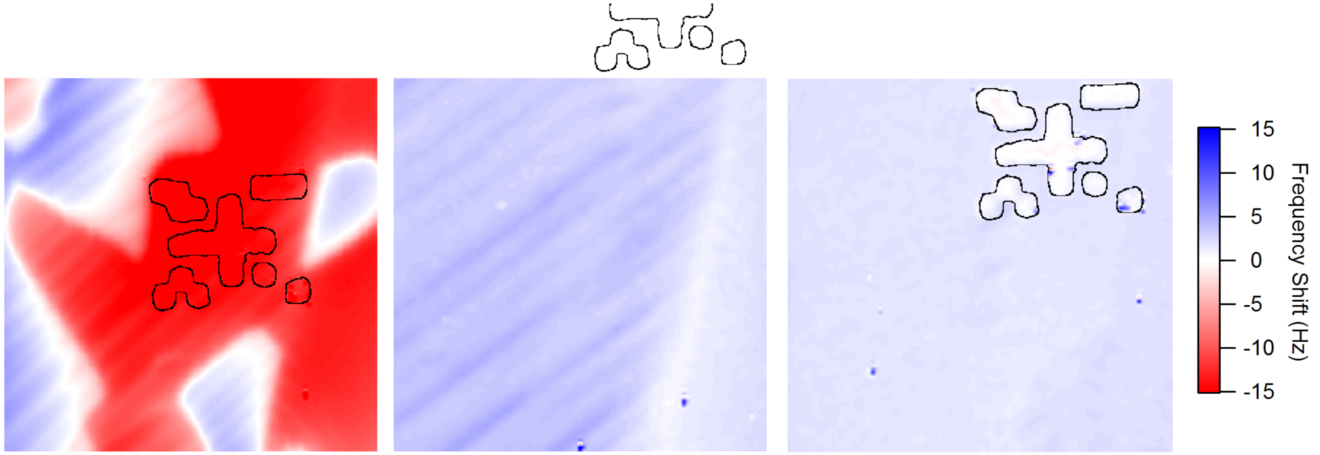

T=21K
Zero field cooled

T=20K
Field cooled in 10kG

T=20K
Field cooled in 20kG

Figure 4.12: Pattern termination in [110] sample by high field along [110] lattice direction. Three scans taken at approximately 20K in three separate field cool sequences are shown. All sequences started from 60K to remove hysteretic effect. Below 20K in 20kG field cool, no stripes were observed. The scan image shows topographical features observed at temperatures above Neel point.

4.2 [001] Samples

The study of [001] sample is divided by grain orientation. The [001] and $[1\bar{1}0]$ grains present in this sample present a very different strain landscape from the [110] sample, as the lattice distortion (the elongation along [110] lattice direction in zero field cool) occurs within the surface plane. External magnetic field is still applied along sample surface normal, i.e. along [001] lattice direction for [001] grains and along $[1\bar{1}0]$ for $[1\bar{1}0]$ grains.

4.2.1 [001] Grain Behavior

Due to symmetry at room temperature, EBSD cannot distinguish between [110] and $[1\bar{1}0]$. Therefore the unit cell axis labeled in this chapter have ± ambiguity. The [001] lattice direction makes 11.5° angle with surface normal. When projected onto the surface plane, the [001] lattice direction is at -172.5° relative to the horizontal scan axis. Almost all of the scan area is in a single [001] grain with no detected defects.

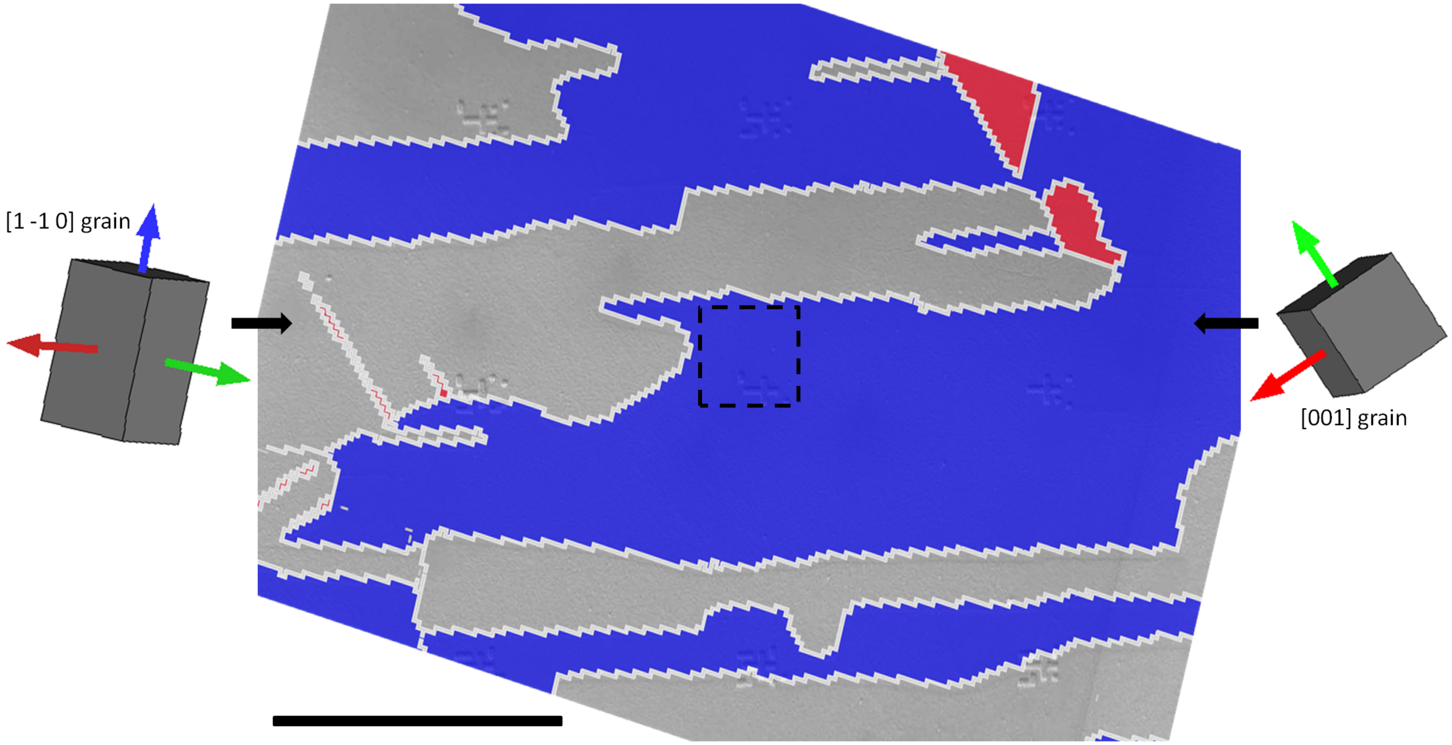

Figure 4.13: EBSD around the location marker 16x9, which reside in a [001] grain. Black scale bar is 10μm. Unit cell illustration is raw from the HKL analysis software. Note that at room temperature, [110] and [$1\bar{1}0$] are identical due to symmetry. Therefore the [$1\bar{1}0$] grain is illustrated as [110]. Approximate scan area is outlined in dashed lines.

Temperature Dependence

Stripe pattern onset in [001] grain is observed around 35K in zero field, above the onset temperature of [110] grains and slightly above T_2. We attribute this temperature difference to the in-plane strain vectors. The striking feature of [001] magnetic patterns is the coexistence of two orientations within the same grain. Fig. 4.13 shows stripes observed in [001] grain near marker 16x9 in two orientations ∼90 degrees apart immediately upon onset. Again, the stripe divisions do not correspond to any as-grown grain boundary. No change in stripe angle or in division boundary is observed as sample is cooled down to base temperature.

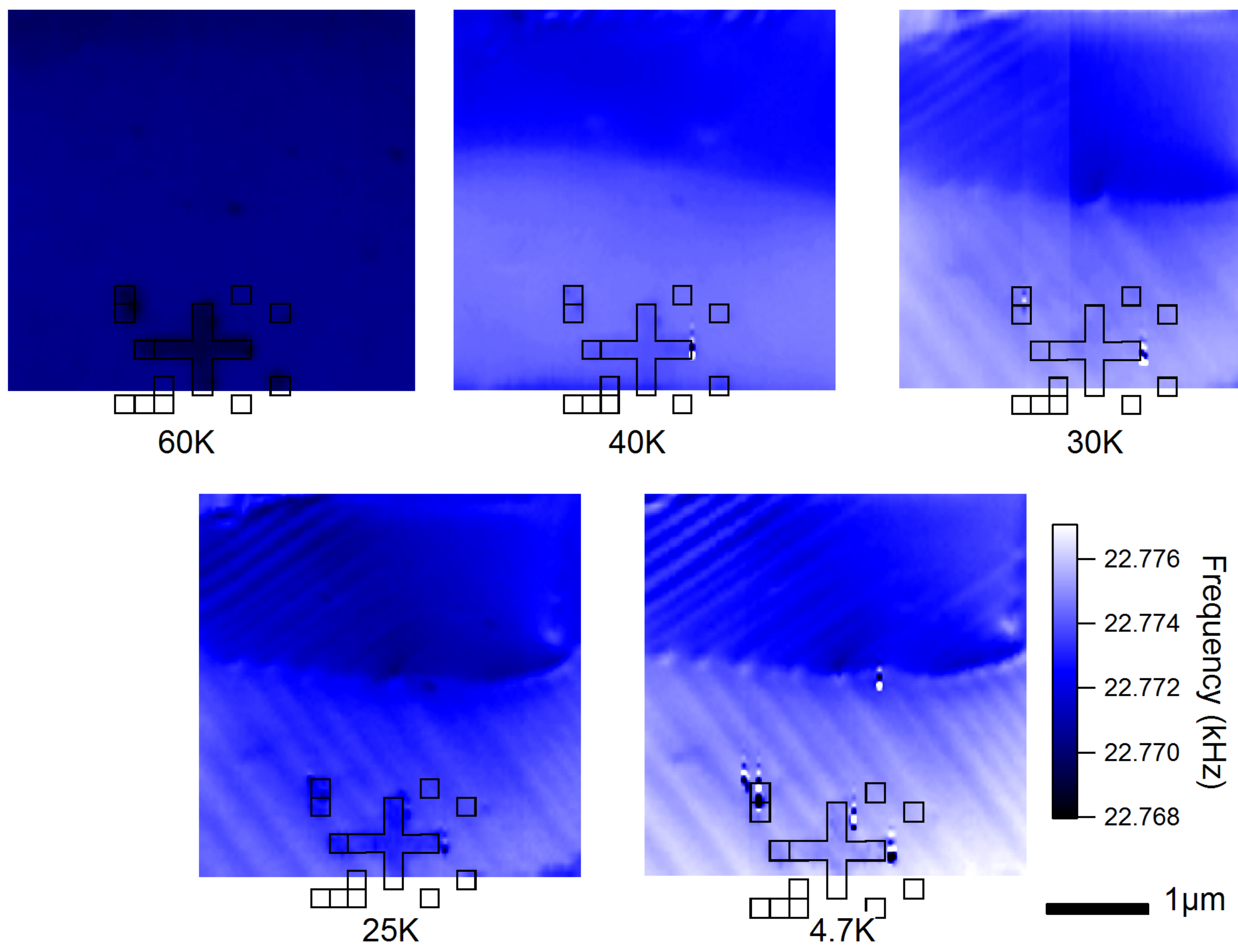

Figure 4.14: Zero Field cool of [001] sample at marker 16x9. Orientation of the stripes divide the (visible) grain into two divisions, each with a unique stripe orientation, approximately 90° from each other. It is remarkable to note the subtle but step-like frequency shift in 40K scan—this step-like boundary eventually developed into the boundary between stripe divisions.

Field Dependence

Applying magnetic field produces interesting stripe division boundary movement (Fig. 4.15). In a field ramp sequence taken at 4K, we observe the smooth, rounded stripe division wall re-positioning and “hardening” into rectilinear shape following re-orientation of part of the stripes. The re-orientation process in 5kG field produced very high frequency shifts. The rectilinear stripe division wall remained in position without change up to 32.5kG. An area scan after field ramp to 27.5kG in 4K (Fig. 4.16) provides better overview of the stripe structure. The [001] grain, which includes the location marker, is broken into two stripe divisions, while the $[1\bar{1}0]$ grain produces a different stripe orientation. The as-grown grain boundary produces highest frequency shifts in the scans.

In fields less than 30kG, the stripe division wall is observed to move, even after hardening into rectilinear form, when field ramp is performed at an elevated temperature (Fig. 4.17). The wall hardening is complete by 5kG. The stripe division wall can be seen to deform beginning at 15G (far left of the 15G scan in Fig. 4.17). Between 15kG and 20kG, the hardened wall is “pushed” further to the top-left of the point of view (Fig. 4.18).

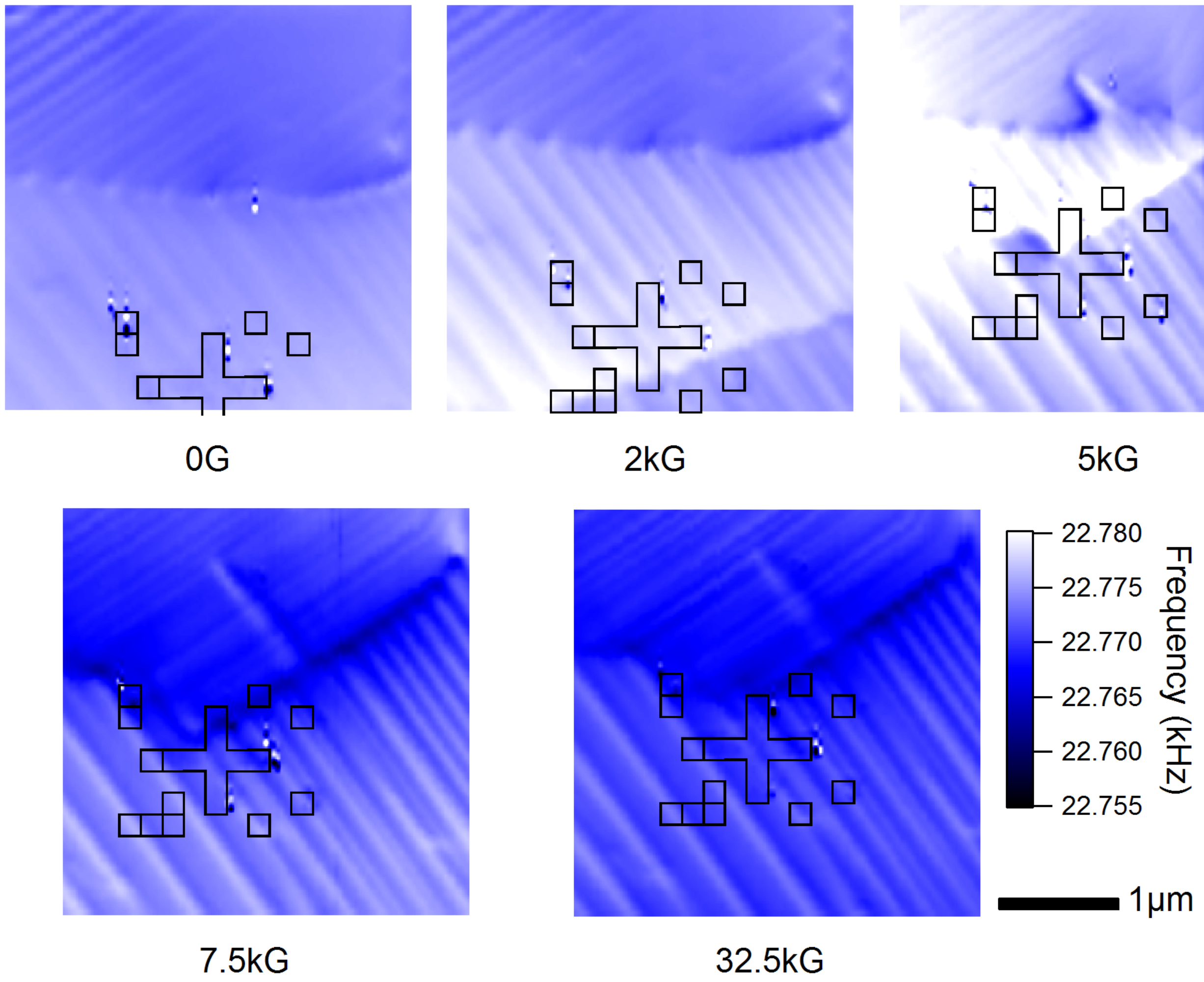

Figure 4.15: Field ramp at 4K in [001] sample, near marker 16x9. Note that the color scale is different from Fig. 4.14. A region of high frequency shift sweeps the lower stripe division (while maintaining stripe structures), terminating at stripe division boundary. The stripe division reconfigures into a recilinear shape after the sweep.

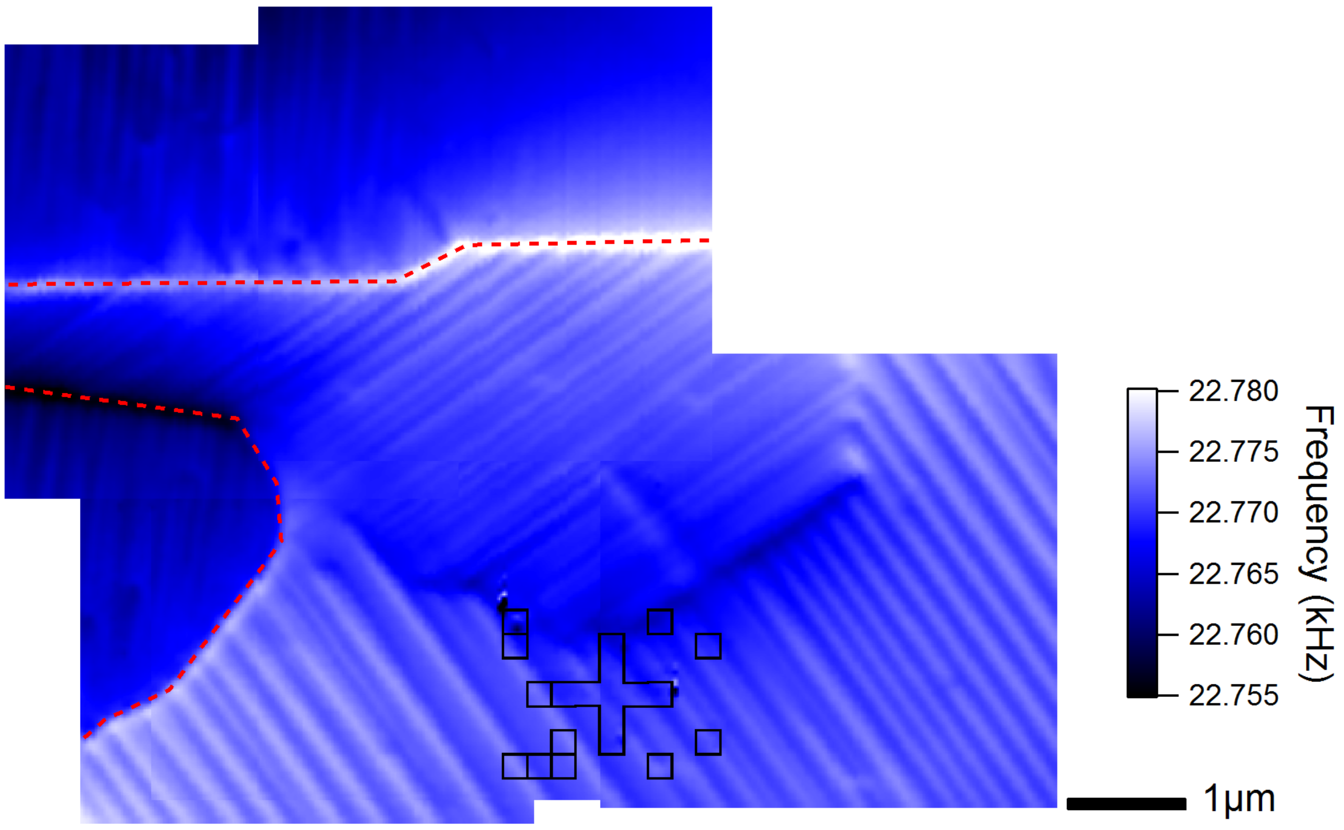

Figure 4.16: Area scan of [001] sample near marker 16x9 after ramping to 27.5kG at 4K, showing the different stripe orientations within the same [001] grain. Grain boundaries are outlined in red dashed lines. The grain containing the marker is [001] while the rest is $[1\bar{1}0]$.

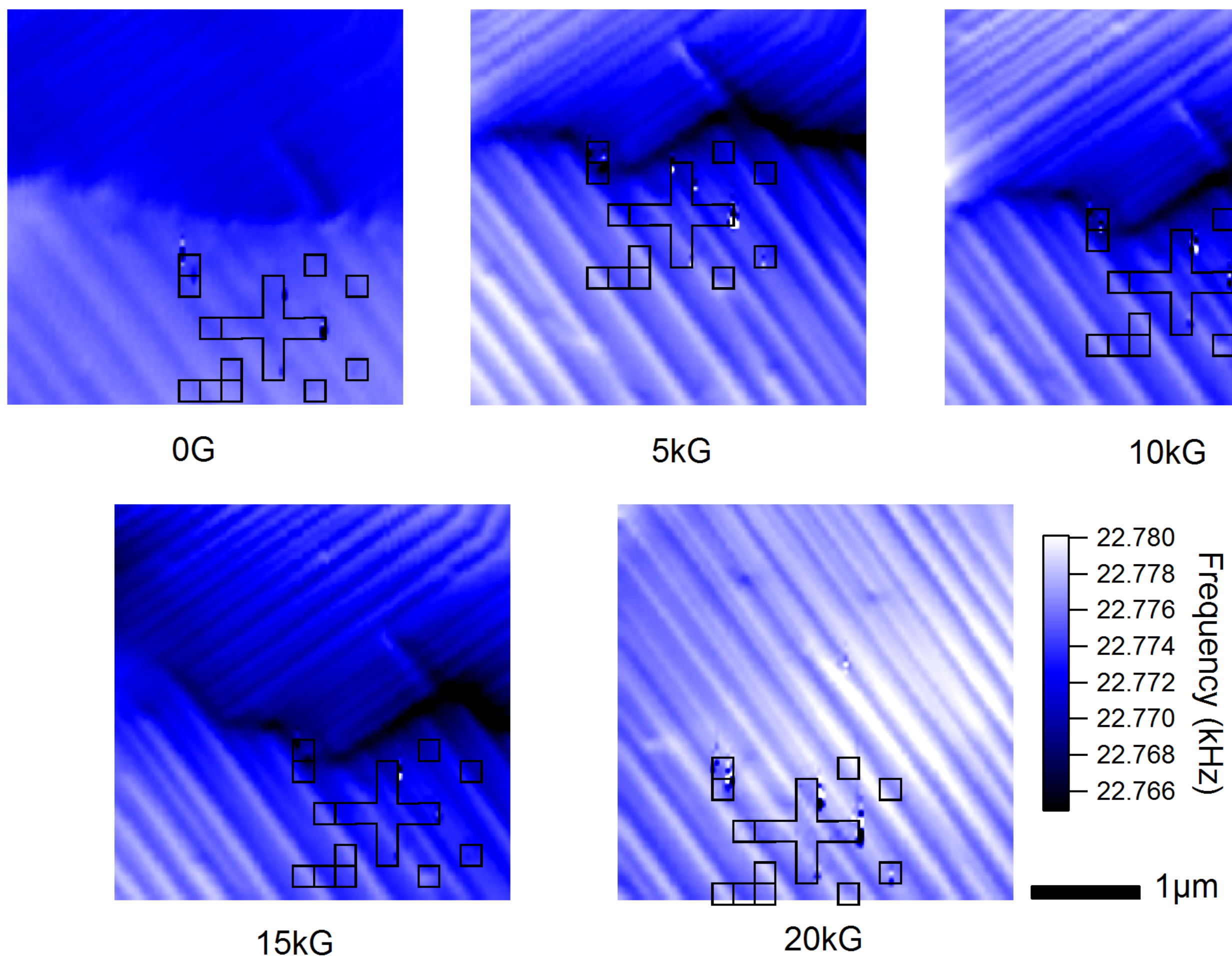

Figure 4.17: Field ramp at 18K in [001] sample, near marker 16x9. Behavior is very similar to 4K field ramp (Fig. 4.15), except at high field when the division wall undergoes another reconfiguration. The sample is very close to a transverse commensurate state at 18K in 20kG (see Fig. 1.6).

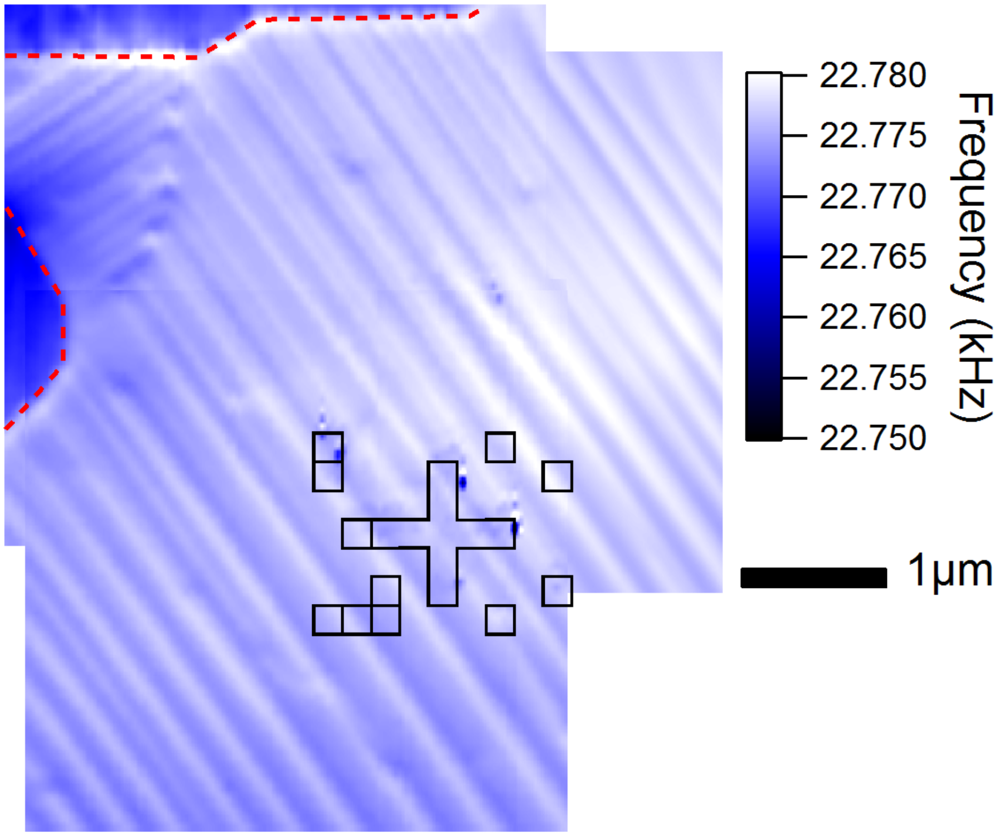

Figure 4.18: Area scan of [001] sample near marker 16x9 after ramping to 20kG at 18K, showing the different stripe orientations within the same [001] grain. Grain boundaries are outlined in red dashed lines. The grain containing the marker is [001] while the rest is $[1\bar{1}0]$.

Stripe Orientation

Cross-referencing EBSD orientation data determined that the stripes in [001] grains are along either [100] or [010] lattice directions (Fig. 4.19). Other than the 90° switch, no other stripe angle variations were observed.

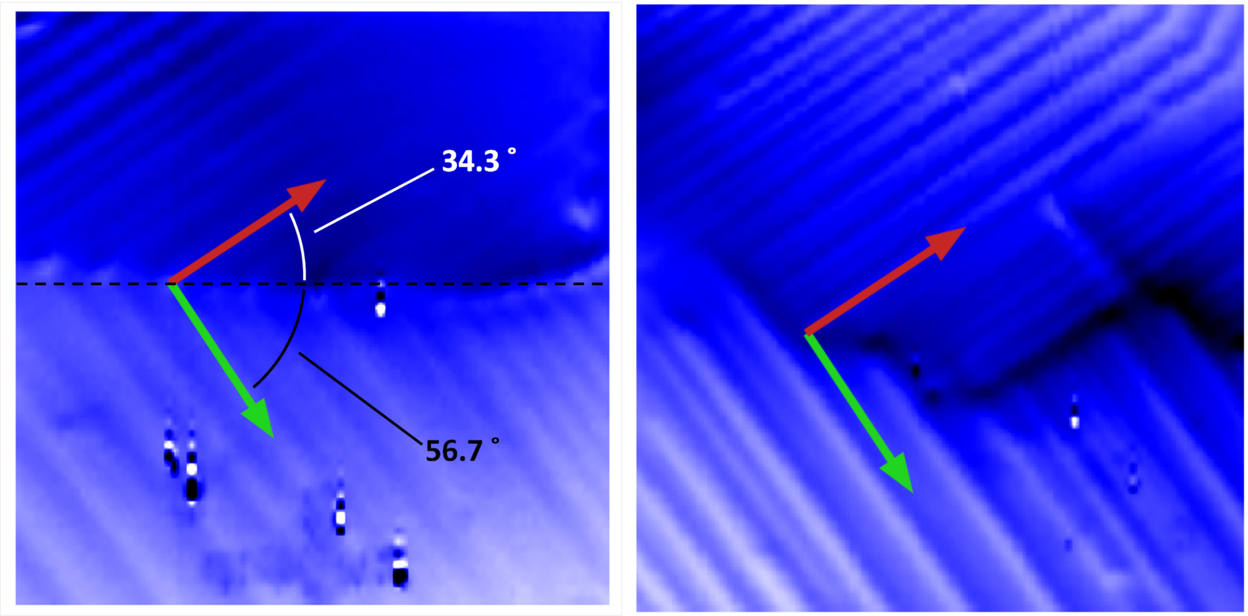

(a) ZFC to 18K

(b) 18K field ramp to 15kG

Figure 4.19: (a) Stripe orientations compared to lattice directions of [001] sample, near marker 16x9 in zero field cool. Red arrow is ±[100] and green arrows represent ±[010]. Angles indicated are those of the lattice axes projected onto the page. The angles do not add up to 90° because [001] lattice direction makes an angle of 11.5° with the surface normal. (b) Stripe orientation after ramping to 15kG at 18K, compared to zero field lattice axes.

4.2.2 [$1\bar{1}0$] Grain Behavior

The [$1\bar{1}0$] grain has [$1\bar{1}0$] lattice direction making an angle of 11.5° with the surface normal. The [001] lattice direction (of [$1\bar{1}0$] grain) is at an angle 77.8° with respect to the horizontal scan axis.

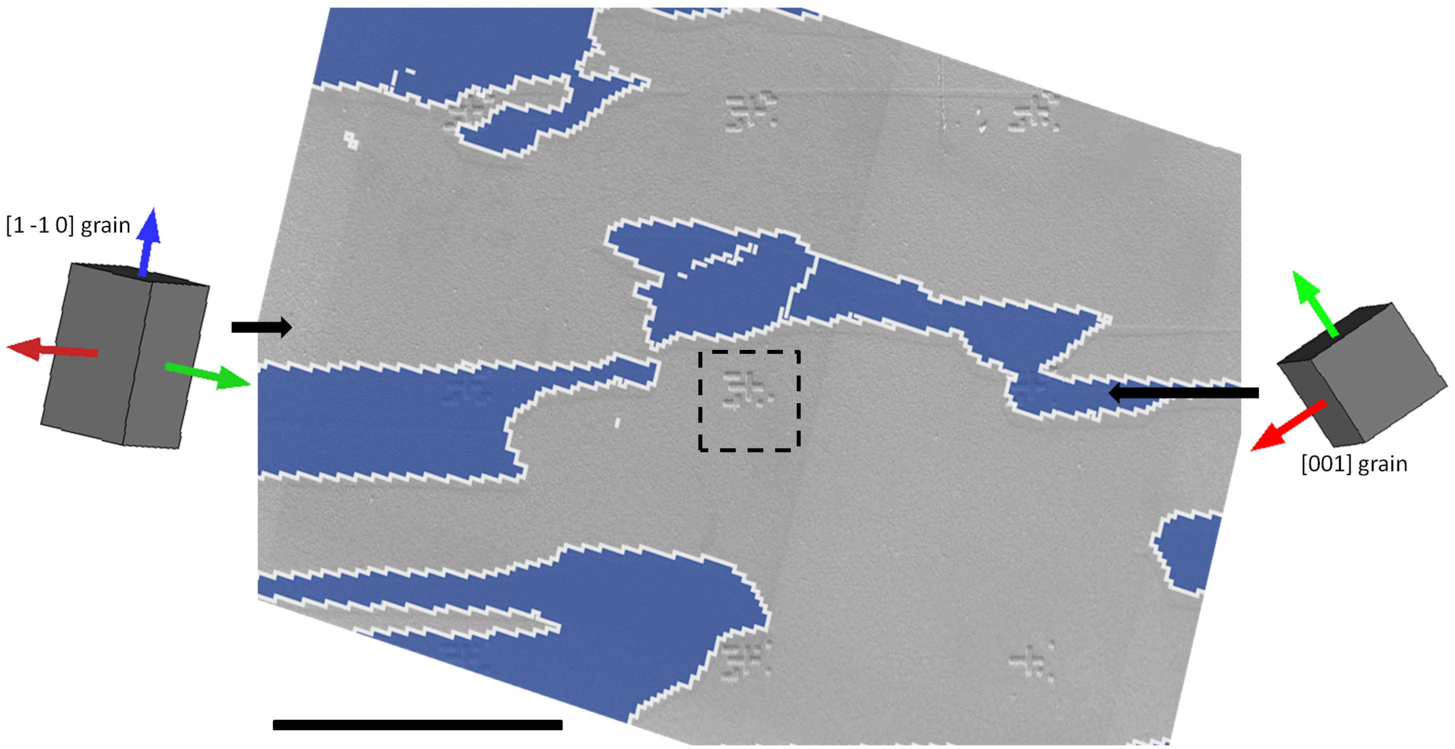

Figure 4.20: EBSD around the location marker 2689, which reside in a $[1\bar{1}0]$ grain. Black scale bar is 10μm. Unit cell illustration is raw from the HKL analysis software. Note that as EBSD is taken at room temperature, [110] and $[1\bar{1}0]$ are identical due to symmetry. Therefore the $[1\bar{1}0]$ grain is illustrated as [110].

Temperature Dependence

Stripes again onset by 35K (Fig. 4.21) in zero field cool, in lieu of features similar to magnetic domains in [110] samples. Stripes are observed to extend over a long range $\geq 4\mu$, with their density increase slightly at lower temperatures. Stripe pitch is approximately 200—400nm. Only one stripe orientation is observed.

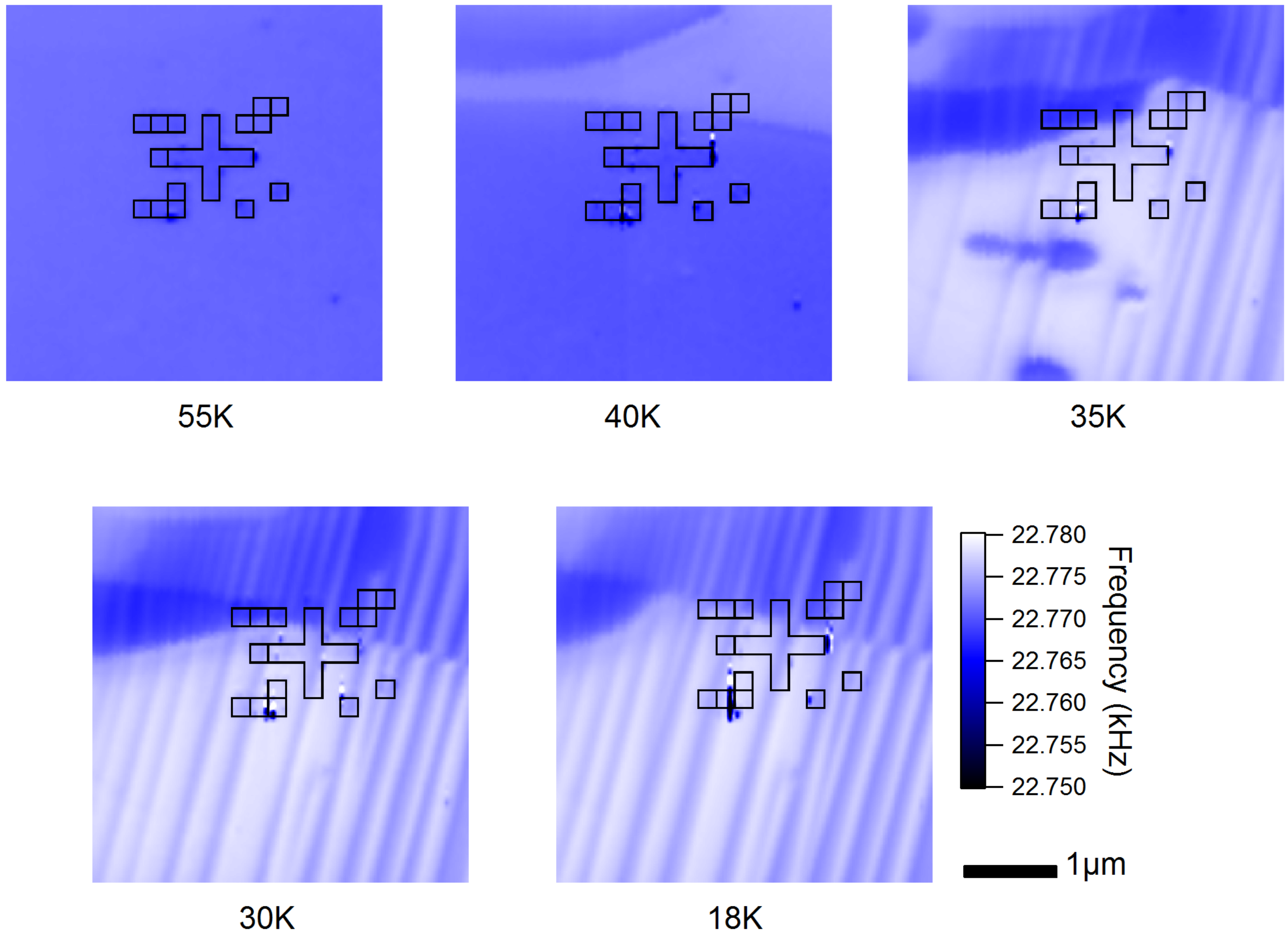

Figure 4.21: ZFC of [1$\bar{1}$0] sample at marker 2689. Both magnetic domain and stripes are observed and persisted until 18K.

Field Dependence

Ramping up the field at 18K (Fig. 4.22) immediately removed any magnetic domain-like feature, as well as inducing a slight change in stripe orientation. Stripes are also more densely packed post-reorientation, with pitches decreasing to 100nm. Increased field results in stripes diminishing as well as becoming more sparse.

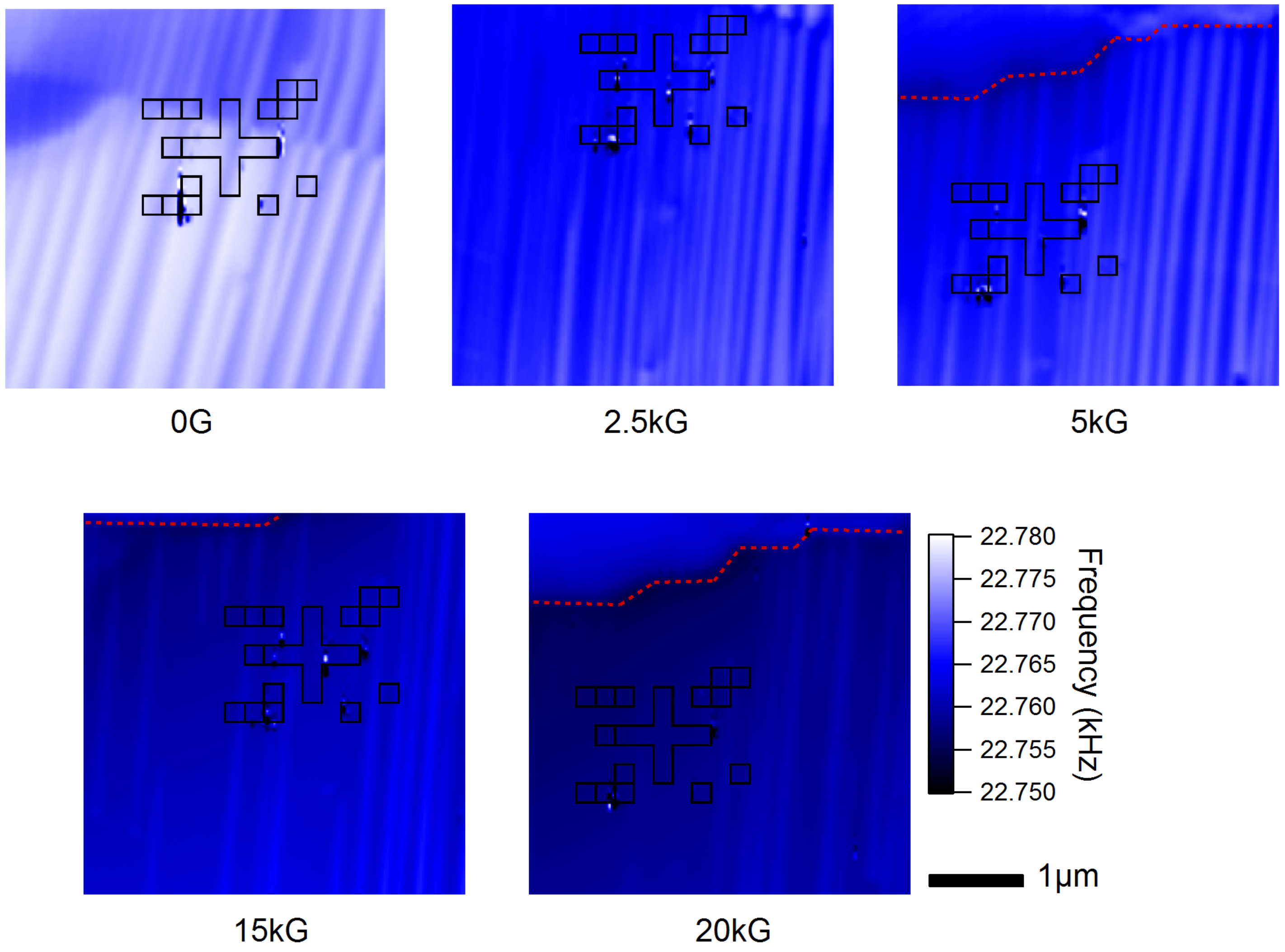

Figure 4.22: Field ramp up of $[1\bar{1}0]$ sample at marker 2689 at 18K. Magnetic domain is removed, and a stripe angle change (of all stripes visible) are observed at 2500G field. Also, we note an increase in stripe density and a decrease in stripe pitch. Some stripes disappeared with increasing field. As-grown grain boundary is outlined in red dashed lines.

Stripe Orientation

Stripes observed in $[1\bar{1}0]$ grain coincides with the [001] lattice direction (Fig. 4.23), similar to the [001] grains. In field, the stripe orientation is tilted 7°—interestingly coinciding with the same tilt observed in [110] sample when subjected to field.

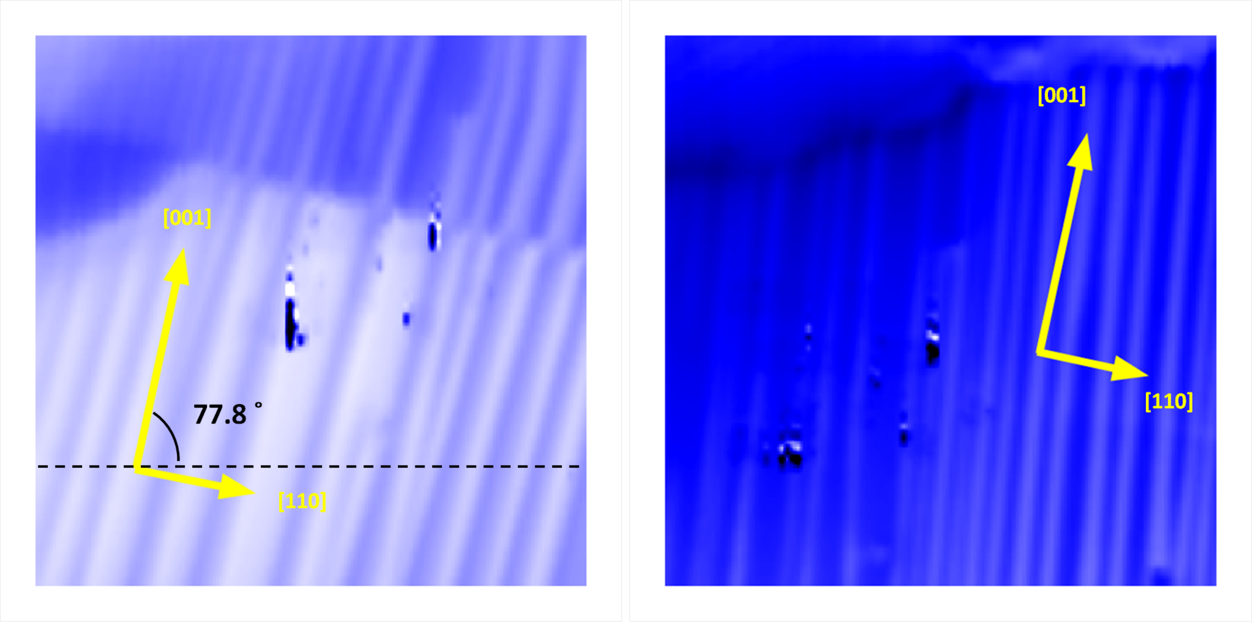

(a) ZFC to 18K

(b) 18K field ramp to 5kG

Figure 4.23: (a) Stripe orientation compared to lattice directions of $[1\bar{1}0]$ sample, near marker 2689. (b) Stripe orientation after field ramping to 5kG in 18K, compared to zero field lattice axes.

4.3 Discussion

The main qualitative questions regarding the stripe features (in [110] and $[1\bar{1}0]$ grains) and tweed pattern (in [001] grains) observed in MFM images are

1. The origin of magnetization difference that produced the magnetic contrast
2. The cause of the particular shape observed—stripes forming a tweed texture
3. The cause or the particular angles of the stripes

Stripe and Tweed Texture

We first examine the second question regarding the pattern shape. This stripe/tweed pattern has been observed in many systems undergoing structural phase transitions or under stain and is particularly prevalent in ferroelastic materials. Ferroelastics are crystalline solids that undergo a shape changing phase transition, usually of first order, to a state of lower symmetry with decreasing temperature [80]. During a structural transition, the formation of structural domains is energetically favorable because it releases stress over the entire lattice in small areas of high deformation [81]. As we will discuss below, structural domains can self-organize into regular patterns. Fig. 4.24 shows examples of tweed pattern formation in iron pnictides [82, 81], $YBa_2Cu_3O_{7-\sigma}$ [83], and $La_{1.99}Sr_{0.01}CuO_4$ [84]. Among the examples, iron pnicitides and $La_{1.99}Sr_{0.01}CuO_4$ both undergo structural transitions from tetragonal to orthorhombic structures similar to Mn_3O_4. Further, the tweed pattern has been observed to extend beyond strictly structural tweeds. Magnetic tweed patterns have been observed in alloy $Co_{0.5}Ni_{0.205}Ga_{0.295}$ [85] as a precursor to the structural transition.

To better understand the tweed patterns observed in Mn_3O_4 in the context of structural phase transitions, we begin by noting that based on stripe orientation information from Fig. 4.5, Fig. 4.19 and Fig. 4.23, a consistent 3D model of the stripe features in zero field cool can be constructed, as shown in Fig. 4.25. In our model, three-dimensional "slabs", oriented normal to either [100] or [010] lattice directions and extend throughout the grain, produce magnetic contrast that comprise the stripe features. Slabs of similar orientation group together into uniform stripe sub-divisions. The sub-divisions are directly visible along [001] lattice direction (see Fig. 4.13). When the sample is polished normal to [110] or $[1\bar{1}0]$ lattice direction, the resulting surface consists of cross-sections of slabs slanted at a 45° angle (Fig. 4.25b and Fig. 4.25d).

During a structural phase transition where atoms are displaced rather than diffused, the crystalline lattice of the parent phase is distorted to produce several possible lattice

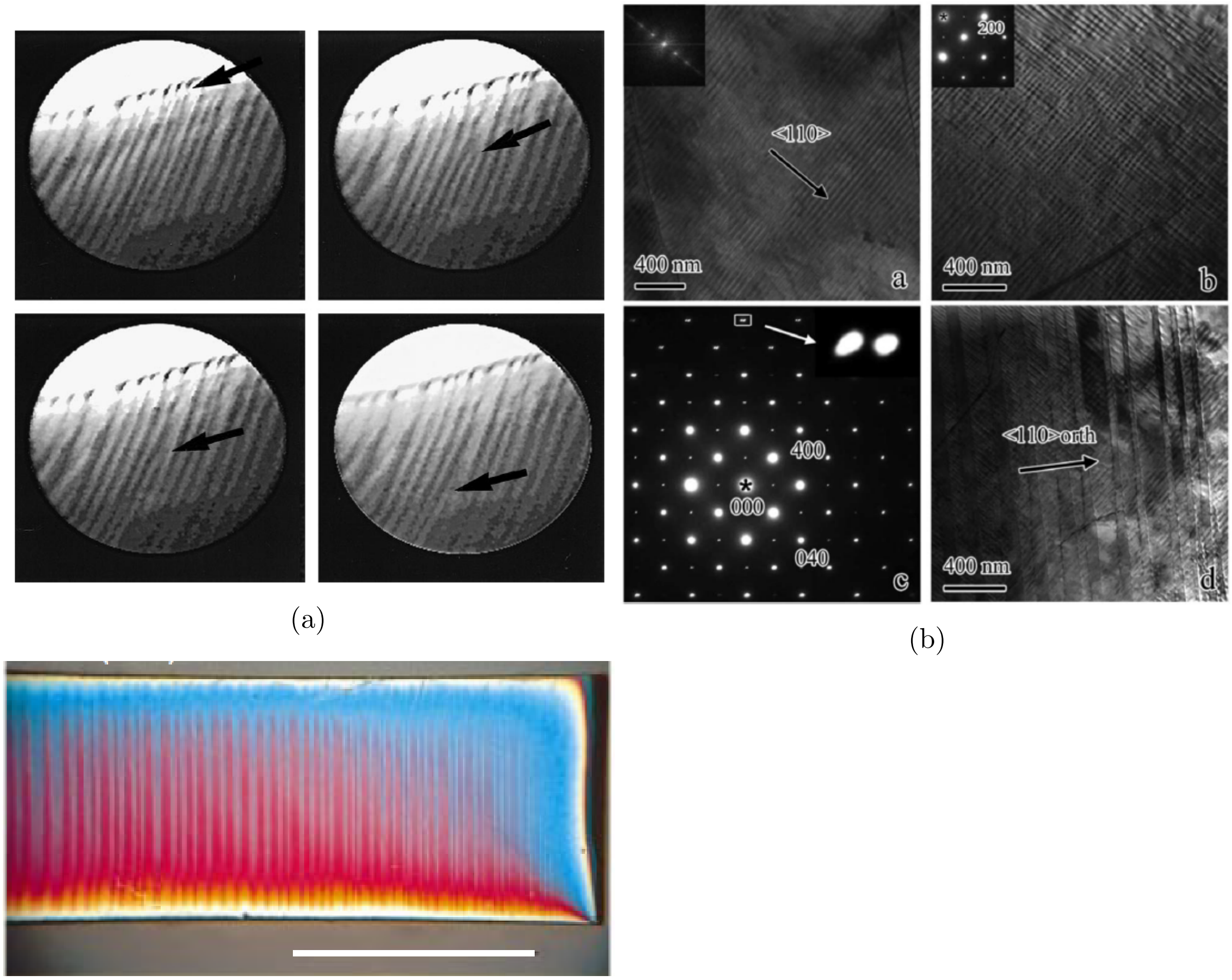

(a)

(b)

(c)

Figure 4.24: Examples of strain-mediated domain formation in various materials. (a) "Needle domain" formed due to strain-induced twinning in $YBa_2Cu_3O_{7-\sigma}$ [83]. (b) Transmission electron microscope images of stripe patterns in $CaFe_2As_2$ [82]. (c) Optical image of stripe domains in magnetic shape memory material $La_{1.99}Sr_{0.01}CuO_4$ (scale bar=0.5mm) [84].

structures of the product phase. Should several lattice structures coexist, the domain walls between these structures must be oriented in such a way to maintain strain compatibility between two adjacent structural domains [86]. The compatibility constraints originate from the symmetry of parent and product structures, and is summarized by Sapriel into [86]:

$$det|e_{ij}^{(1)} - e_{ij}^{(2)}| = 0 \tag{4.1}$$

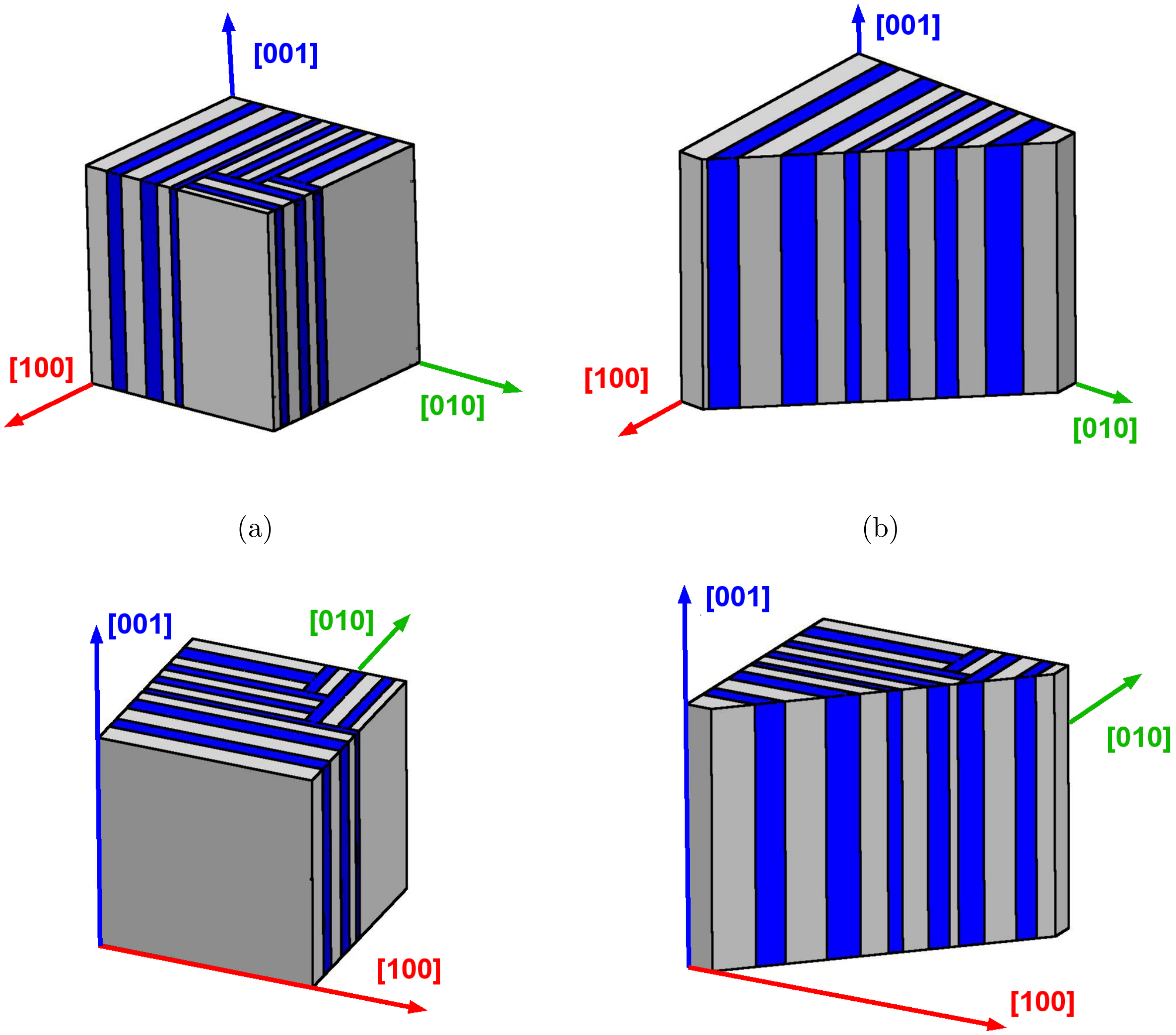

(a) (b) (c) (d)

Figure 4.25: 3D illustration of proposed stripe structure. Lattice directions are labeled using parent (tetragonal) unit vectors. (a) and (b) viewing down [110] lattice direction; (c) and (d) viewing down $[1\bar{1}0]$ lattice direction. Blue and gray slabs represent regions of different magnetic structure that produces magnetic contrast in MFM.

$$Tr(e_{ij}^{(1)} - e_{ij}^{(2)}) = 0 \tag{4.2}$$

where e_{ij} are strain tensors across the structural domain wall.

In the present case of Mn_3O_4, the parent structure is $I41/amd$ (designated T lattice). Calculations performed by FindSym[2] indicate that product structure is an $Fddd$ orthorhom-

---

[2] A component of ISOTROPY software developed by Stokes et al, retrieved from

bic lattice making a 45° angle with the [100] lattice direction of the tetragonal parent state. The two possible product orthorhombic configurations correspond to I (designated O lattice) and III (O' lattice) respectively in Fig. 1.6b. This transformation from the Laue group of $4/mmm$ (tetragonal) to mmm (orthorhombic) satisfies the compatibility constraint under category 4 of Sapriel's classification, and allows coherent domain walls to form normal to [100] and [010] lattice directions of the parent (tetragonal) lattice [86]. In our 3D model of the stripes, Fig. 4.25, these are exactly the planes that the slabs reside in.

The fact that structural domain walls in Mn_3O_4 are allowed by parent-product symmetries does not necessarily mean these walls, and by extension the tweed textures, would exist. We need to establish that Mn_3O_4 indeed satisfies the basic requirements to produce such patterns. The formation of this tweed texture in ferroelastics has been the focus of intensive study (for example, [83, 87, 88, 89, 90, 91, 92, 93, 80, 94]). During the structural phase transitions, strain coupling is the necessary ingredient, regardless of whether the strain coupling is the dominant factor in the Landau functional (a "proper" ferroelastic transition) or a secondary one (an "improper" one) [94]. Spontaneous strain has already been reported in Mn_3O_4 [31] and the building blocks of Mn_3O_4 are structurally rigid units, i.e. AO_4 tetrahedra and BO_6 octahedra. Such rigid units have been theorized to produce the "knock on" effect that propagates initial strain at location R_i to other rigid units R_j around the initial site via cooperative displacement [87, 90]. The strain coupling (taking into consideration the symmetry of parent-product lattices) can be represented by an ordering interaction $J(R_{ij})$, of the form [90]:

$$J(R) \sim \frac{A_2 Y_{2m}(\theta,\varphi) + A_4 Y_{4m}(\theta,\varphi)}{R^3} + J_Z \tag{4.3}$$

$$J_Z = \frac{Z}{N} \tag{4.4}$$

where Y_{lm} represent appropriate spherical harmonic of order 2 and 4, J_Z represent a Zener-Eshelby type of force and N the total number of rigid units in the specimen.

---

http://stokes.byu.edu/iso/isotropy.html on March 30, 2011.

Given this strain coupling, mesoscopic pattern formation mechanism has been described by Landau expansion of the elastic energy in powers of the strains and their gradients [90, 92]. This result is general, regardless of other physical variables, and boils down to three criteria for the particular system to produce tweed-like patterns in a "nucleate and grow" scheme [85]:

- *The material system must be "sensitive" to local symmetry breaking perturbations. That is, there is a softening of the relevant elastic constants or phonons.*
- *There must be long-range interactions caused by elastic compatibility constraints... Such interactions enable connections between the local transformed regions... thereby stabilizing them.*
- *To obtain a specific modulation pattern, one needs anisotropy to select modulations along specific directions.*

The first criteria creates so-called "embryos" for the structural domain formation. In Mn_3O_4, both pressure and magnetic field can produce such softening [33], as well as strain caused by lattice mismatch at grain boundaries. The second criteria provides the stabilizing interaction for regions in which the transition has already been completed, and is fulfilled by the magnetic coupling [85]. Symmetry constraints discussed above provide the necessary anisotropy. As shown in Fig. 4.4, the stripe features do indeed follow a "nucleate and grow" process with embryos starting from grain boundaries.

Taking into consideration that the structural transition in Mn_3O_4 at T_2 is accompanied by a magnetic transition, we believe that the tweed patterns observed in our study are the magnetic manifestation of a structural domain formation during T_2 transition. Consequently, the slabs in our 3D model are spatially separated regions having different magnetic and lattice structures.

Magnetic Contrast

It is important to point out that although the Mn_3O_4 system behaves like a proper T-O transition ferroelastic, there is one significant difference. Usually, the domain walls produced in a proper ferroelastic transition are between two *product lattices*—in systems belonging to Sapriel group 4, they would be orthorhombic to orthorhombic (O-O') walls [86]. In contrast, the Raman scattering result by Kim et al shows that after the T_2 transition in zero field, the Mn^{2+}-O^{2-} spectra show strong intensity in 300-cm^{-1}-split mode and weak 290-cm^{-1}-split mode with light polarized along $[1\bar{1}0]$ (tetragonal) direction (Fig. 4.26) [33]. In other words, one of the two orthorhombic lattices is dominating (the O state), while the 295-cm^{-1}-split mode associated with the tetragonal lattice also persists below T_2.

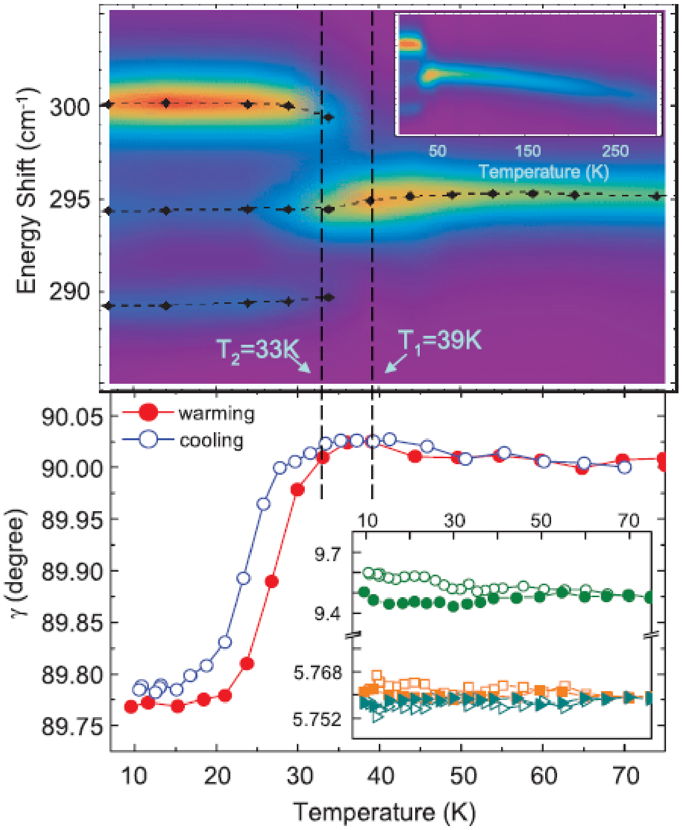

Figure 4.26: Contour plot of Mn^{2+} ion's T_{2g} phonon mode intensity (top) and γ angle (bottom) with respect to temperature, in zero field cooling/warming of a [110] sample [33].

We believe that the two lattices present across the walls are the T and O lattices and the domain walls are predominantly T-O walls (i.e. the parent-product kind, Fig. 4.27), instead of the O-O' walls commonly observed. Our interpretation is that O' distortion is prohibited by magneto-elastic coupling due to the energy cost. This energy cost can be offset by applying magnetic field in the distortion direction ($[1\bar{1}0]$ direction in the tetragonal phase), although a large field is required, as shown in Fig. 1.6 [33]. This is a unique structural domain wall type that was predicted (based on free energy calculations containing strain terms only) to exist only at transition temperature [95]. Under the strain-only analysis, at other temperatures, the energy of T and O states are not equal, resulting in either non-existence of one of the states, or one of them being unstable [95]. In Mn_3O_4, however, the magneto-elastic coupling equalizes the energy across domain wall so that the domain wall persists from T_2 down to 4K in zero field (Fig. 4.2).

In light of the structural phase separation interpretation, the blue and grey slabs in Fig. 4.25 represent spatially separated commensurate and incommensurate phases of Mn_3O_4. The magnetic contrast in [110] samples (see, for example, Fig. 4.5), is a direct result of the different magnetization between the two phases.

The "phase separation" interpretation of the tweed structure in Mn_3O_4 is further supported by past studies of Mn_3O_4 and related spinel systems. Theoretical work by [96], Ivanov et al. explored the mechanism of spinodal decomposition of structural phases due to cooperative Jahn-Teller effect. Although the discussion in Ivanov et al is centered around the cubic to tetragonal transition at higher temperatures, the calculation of the free energy is still applicable to the tetragonal to orthorhombic transition at T_2 as the $t2g$ orbital degeneracy is present in Mn^{2+} ions in the tetragonal phase and is coupled to the lattice strain [32]. Ivanov et al showed that the decomposition of the phases is energetically favorable, pointing toward the possibility of coexisting but spatially separated incommensurate (tetragonal) and commensurate (orthorhombic) phases in Mn_3O_4.

Behaviors of magnetic stripes in Mn_3O_4 are indeed observed to be generally in agreement with this phase separation hypothesis. For example, as shown in Fig. 4.22, stripes become

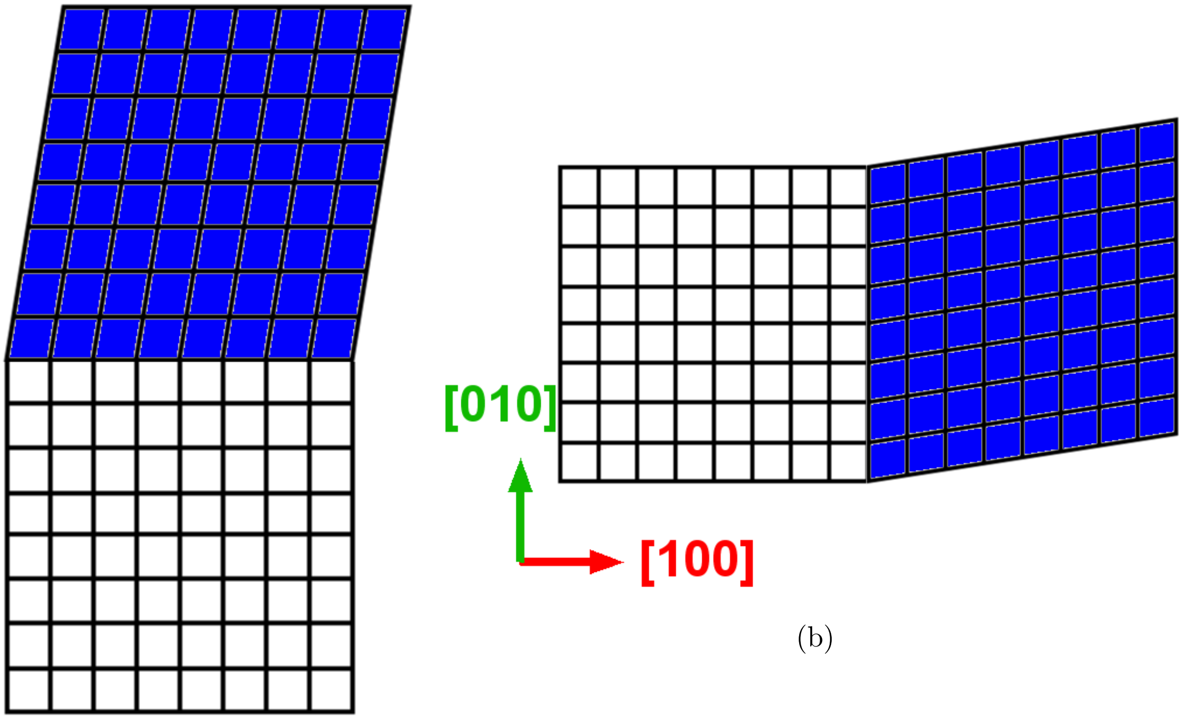

(a)

(b)

Figure 4.27: The two orientations of structural domain boundary between tetragonal lattice (incommensurate magnetic ordering, white) and orthorhombic lattice (commensurate magnetic ordering, blue). Shown as viewed down [001] lattice direction: (a) T-O wall along [100] and (b) T-O wall along [010]. Distortion is exaggerated to show effect. The actual domain wall is possibly spread over a number of unit cells. Magnetic cell-doubling occurs along [010] [36]. All lattice directions are labeled based on the tetragonal phase.

significantly more sparse in response to higher applied magnetic fields along $[1\bar{1}0]$. This is due to the transverse field driving Mn_3O_4 from commensurate (O lattice) into a spin disordered (T lattice) state (Fig. 1.6).

The phase separation can also be eliminated by applying a large field parallel to [110] lattice direction. This large field along magnetic easy axis makes the O lattice energetically favorable, resulting in a homogeneous, commensurate state with O lattice structure, as shown in Fig. 4.12.

The variation of magnetic strips angles in [110] and $[1\bar{1}0]$ images (e.g. Fig. 4.10 and Fig. 4.22) are interesting, as the structural transformation in a ferroelastic is generally resistant to such variations. We do note however, that the magnetic coupling between Mn^{3+} spins (which are responsible for the magnetic ordering [41]) along the [001] direction is an order of magnitude smaller than that in the plane normal to it (i.e. the plane defined by [110] and [$1\bar{1}0$]) [41]. Moreover, the commensurate magnetic ordering has a cell-doubling effect along [110] lattice direction, orthogonal to [001] [36]. We propose that the balance between magnetic coupling and strain coupling is anisotropic in such a way that along [001], the strain coupling dominates, while along [110] and [$1\bar{1}0$], the magnetic coupling dominates. The stripe angle variation within the same grain, as shown in Fig. 4.10 and Fig. 4.22, are the result of the interplay between these two couplings. Applying a magnetic field along [110] or [$1\bar{1}0$] disrupts the existing balance and results in a tilting of the stripes away from the ideal [001] direction favored by strain coupling, toward a direction favored by magnetic coupling (orthogonal to [001], most likely [110]).

An alternative explanation of the stripe angle variation is the effect of anisotropy field H_A. At H_A, the external magnetic field overcomes the spontaneous magnetization set by the magneto-crystalline anisotropy of the material. In fields $H < H_A$, the spin direction is determined by the magneto-crystalline and magnetoelastic effects. In fields $H > H_A$, the external magnetic field dominates the spin-lattice coupling energy, and drives the stripes away from the [001] direction.

The observation of phase separation during the magneto-structural phase transition in Mn_3O_4 indicates that similar behaviors are most likely present in other strongly spin-lattice coupled materials. A prominent example is MnV_2O_4, which shares almost identical spin structure [41] and undergoes a magneto-structural transition from cubic to tetragonal lattice at 58K. Evidence for magneto-structural phase separation has already been observed via electron spin resonance in MnV_2O_4 [97, 31]. The Jahn-Teller effect in MnV_2O_4 distorts along a direction 90° from that of Mn_3O_4 at T_2 [41]. Comparison between Mn_3O_4 and MnV_2O_4 would shed more light into the role of Jahn-Teller distortions in these phase transitions. Fortunately, the low temperature microscope and sample preparation steps developed in this thesis are directly applicable to a wide range of materials like MnV_2O_4 and Mn_3O_4, in which mesoscale magnetic phase separation develops, paving the way for future imaging studies of these scientifically interesting and technologically important materials.

Chapter 5

Conclusions

In this thesis, we develop a magnetic force microscope and preparation procedures to study the magneto-structural phases of Mn_3O_4. The rich interplay between geometric frustration, spin-lattice coupling and magnetic interactions in Mn_3O_4 produces complex phase diagrams. To better understand the transition between an incommensurate-ordered, tetragonal lattice phase to a commensurate-ordered, orthorhmbic phase, we combine magnetic imaging and lattice structure mapping techniques.

Our results show that novel nanometer-scale magnetic patterns in form of interwoven stripes emerge across the transition temperature. These stripes exist in a wide region of temperature-magnetic field parameter space, and are visible under MFM in [110], $[1\bar{1}0]$ and [001] lattice directions. Although the stripes primarily appear in a "nucleate and grow" manner out of the grain boundaries, they maintain long range stability, extending across grains order of magnitude wider than the stripe pitch.

A 3D model of the stripes is constructed, with stripes extending throughout the specimen along [001] into a "slab" shape. The orientation of slabs agrees with well known compatibility constrains for structural domain wall formation. Mn_3O_4 also satisfies other essential criteria for structural phase separation mediated by strain coupling. We therefore conclude that the stripes/slabs are magnetic manifestation of magneto-structural phase separation in Mn_3O_4. We believe the stripes are alternating commensurate-incommensurate phases. The magnetization difference produces magnetic contrast observed in MFM images. The structural walls separating the phases is a unique type that is stabilized by magneto-elastic coupling to exist at temperatures outside transition temperature. The technique developed in this thesis, as well as the evidence for magneto-structural phase separation, opens doors to investigation into other strongly correlated materials such as MnV_2O_4.

References

[1] E. Dagotto, "Complexity in strongly correlated electronic systems," *SCIENCE*, vol. 309, pp. 257–262, JUL 8 2005.

[2] E. Dagotto, T. Hotta, and A. Moreo, "Colossal magnetoresistant materials: The key role of phase separation," *PHYSICS REPORTS-REVIEW SECTION OF PHYSICS LETTERS*, vol. 344, pp. 1–153, APR 2001.

[3] V. Emery, S. Kivelson, and J. Tranquada, "Stripe phases in high-temperature superconductors," *PROCEEDINGS OF THE NATIONAL ACADEMY OF SCIENCES OF THE UNITED STATES OF AMERICA*, vol. 96, pp. 8814–8817, AUG 3 1999.

[4] E. Dagotto and Y. Tokura, "Strongly Correlated Electronic Materials: Present and Future," *MRS BULLETIN*, vol. 33, pp. 1037–1045, NOV 2008.

[5] J. Wei and D. Natelson, "Nanostructure studies of strongly correlated materials," *NANOSCALE*, vol. 3, no. 9, pp. 3509–3521, 2011.

[6] J. P. Perdew, J. A. Chevary, S. H. Vosko, K. A. Jackson, M. R. Pederson, D. J. Singh, and C. Fiolhais, "Atoms, molecules, solids, and surfaces: Applications of the generalized gradient approximation for exchange and correlation," *Phys. Rev. B*, vol. 46, pp. 6671–6687, Sep 1992.

[7] L. F. Feiner, A. M. Oleś, and J. Zaanen, "Quantum melting of magnetic order due to orbital fluctuations," *Phys. Rev. Lett.*, vol. 78, pp. 2799–2802, Apr 1997.

[8] T. Vojta, "Quantum phase transitions in electronic systems," *Annalen der Physik*, vol. 9, no. 6, pp. 403–440, 2000.

[9] X. WEN, "MEAN-FIELD THEORY OF SPIN-LIQUID STATES WITH FINITE-ENERGY GAP AND TOPOLOGICAL ORDERS," *PHYSICAL REVIEW B*, vol. 44, pp. 2664–2672, AUG 1 1991.

[10] Y. Shimizu, K. Miyagawa, K. Kanoda, M. Maesato, and G. Saito, "Spin liquid state in an organic mott insulator with a triangular lattice," *Phys. Rev. Lett.*, vol. 91, p. 107001, Sep 2003.

[11] K. Binder and A. P. Young, "Spin glasses: Experimental facts, theoretical concepts, and open questions," *Rev. Mod. Phys.*, vol. 58, pp. 801–976, Oct 1986.

[12] S. T. Bramwell and M. J. P. Gingras, “Spin ice state in frustrated magnetic pyrochlore materials,” *Science*, vol. 294, no. 5546, pp. 1495–1501, 2001.

[13] U. Chatterjee, D. Ai, J. Zhao, S. Rosenkranz, A. Kaminski, H. Raffy, Z. Li, K. Kadowaki, M. Randeria, M. R. Norman, and J. C. Campuzano, “Electronic phase diagram of high-temperature copper oxide superconductors,” *Proceedings of the National Academy of Sciences*, vol. 108, no. 23, pp. 9346–9349, 2011.

[14] D. K. Singh, A. Thamizhavel, J. W. Lynn, S. Dhar, J. Rodriguez-Rivera, and T. Herman, “Field-induced quantum fluctuations in the heavy fermion superconductor CeCu2Ge2,” *SCIENTIFIC REPORTS*, vol. 1, OCT 13 2011.

[15] H. Pfau, S. Hartmann, U. Stockert, P. Sun, S. Lausberg, M. Brando, S. Friedemann, C. Krellner, C. Geibel, S. Wirth, S. Kirchner, E. Abrahams, Q. Si, and F. Steglich, “Thermal and electrical transport across a magnetic quantum critical point,” *NATURE*, vol. 484, pp. 493–497, APR 26 2012.

[16] T. Park, M. J. Graf, L. Boulaevskii, J. L. Sarrao, and J. D. Thompson, “Electronic duality in strongly correlated matter,” *PROCEEDINGS OF THE NATIONAL ACADEMY OF SCIENCES OF THE UNITED STATES OF AMERICA*, vol. 105, pp. 6825–6828, MAY 13 2008.

[17] E. J. W. Verwey

[18] J. A. Robertson, S. A. Kivelson, E. Fradkin, A. C. Fang, and A. Kapitulnik, “Distinguishing patterns of charge order: Stripes or checkerboards,” *Phys. Rev. B*, vol. 74, p. 134507, Oct 2006.

[19] A. F. Kusmartseva, B. Sipos, H. Berger, L. Forró, and E. Tutis, “Pressure induced superconductivity in pristine $1t-tise_2$,” *Phys. Rev. Lett.*, vol. 103, p. 236401, Nov 2009.

[20] C. H. Chen, S.-W. Cheong, and H. Y. Hwang, “Charge-ordered stripes in $\mathrm{la}_{1-x}\mathrm{ca}_x\mathrm{mno}_3$ with x ¿ 0.5 (invited),” *Journal of Applied Physics*, vol. 81, no. 8, pp. 4326–4330, 1997.

[21] T. Hanaguri, C. Lupien, Y. Kohsaka, D. Lee, M. Azuma, M. Takano, H. Takagi, and J. Davis, “A ‘checkerboard’ electronic crystal state in lightly hole-doped Ca2-xNaxCuO2Cl2,” *NATURE*, vol. 430, pp. 1001–1005, AUG 26 2004.

[22] W. D. Wise, M. C. Boyer, K. Chatterjee, T. Kondo, T. Takeuchi, H. Ikuta, Y. Wang, and E. W. Hudson, “Charge-density-wave origin of cuprate checkerboard visualized by scanning tunnelling microscopy,” *NATURE PHYSICS*, vol. 4, pp. 696–699, SEP 2008.

[23] C. Jooss, L. Wu, T. Beetz, R. F. Klie, M. Beleggia, M. A. Schofield, S. Schramm, J. Hoffmann, and Y. Zhu, “Polaron melting and ordering as key mechanisms for colossal resistance effects in manganites,” *PROCEEDINGS OF THE NATIONAL ACADEMY OF SCIENCES OF THE UNITED STATES OF AMERICA*, vol. 104, pp. 13597–13602, AUG 21 2007.

[24] C. Renner, G. Aeppli, and H. Ronnow, “Charge ordering, stripes and phase separation in manganese perovskite oxides: An STM/STS study,” *MATERIALS SCIENCE & ENGINEERING C-BIOMIMETIC AND SUPRAMOLECULAR SYSTEMS*, vol. 25, pp. 775–778, DEC 2005. Symposium on Current Trends in Nanoscience - From Materials to Applications held at the 2004 EMRS Spring Meeting, Strasbourg, FRANCE, MAY 24-28, 2004.

[25] A. Moreo, S. Yunoki, and E. Dagotto, “Phase separation scenario for manganese oxides and related materials,” *Science*, vol. 283, no. 5410, pp. 2034–2040, 1999.

[26] W. Eerenstein, N. D. Mathur, and J. F. Scott, “Multiferroic and magnetoelectric materials,” *NATURE*, vol. 442, pp. 759–765, AUG 17 2006.

[27] E. R. Callen and H. B. Callen, “Static magnetoelastic coupling in cubic crystals,” *Phys. Rev.*, vol. 129, pp. 578–593, Jan 1963.

[28] R. Tackett, G. Lawes, B. C. Melot, M. Grossman, E. S. Toberer, and R. Seshadri, “Magnetodielectric coupling in mn_3o_4,” *Phys. Rev. B*, vol. 76, p. 024409, Jul 2007.

[29] M. Weiler, M. Althammer, F. D. Czeschka, H. Huebl, M. S. Wagner, M. Opel, I.-M. Imort, G. Reiss, A. Thomas, R. Gross, and S. T. B. Goennenwein, “Local charge and spin currents in magnetothermal landscapes,” *Phys. Rev. Lett.*, vol. 108, p. 106602, Mar 2012.

[30] H. Shinaoka, T. Miyake, and S. Ishibashi, “Noncollinear magnetism and spin-orbit coupling in $5d$ pyrochlore oxide $cd_2os_2\mathbf{o}_7$,” *Phys. Rev. Lett.*, vol. 108, p. 247204, Jun 2012.

[31] T. Suzuki and T. Katsufuji, “Magnetodielectric properties of spin-orbital coupled system mn_3o_4,” *Phys. Rev. B*, vol. 77, p. 220402, Jun 2008.

[32] M. Kim, X. M. Chen, Y. I. Joe, E. Fradkin, P. Abbamonte, and S. L. Cooper, “Mapping the magnetostructural quantum phases of $mn_3\mathbf{o}_4$,” *Phys. Rev. Lett.*, vol. 104, p. 136402, Mar 2010.

[33] M. Kim, X. M. Chen, X. Wang, C. S. Nelson, R. Budakian, P. Abbamonte, and S. L. Cooper, “Pressure and field tuning the magnetostructural phases of mn_3o_4: Raman scattering and x-ray diffraction studies,” *Phys. Rev. B*, vol. 84, p. 174424, Nov 2011.

[34] “Magnetic transitions in mn_3o_4 and an anomaly at 38 k in magnetization and specific heat,” *Physical Review B*, vol. 83, no. 9, p. 094423, 2011.

[35] “Spin state of mn_3o_4 investigated by ^{55}mn nuclear magnetic resonance,” *Physical Review B*, vol. 84, no. 17, p. 174423, 2011.

[36] G. B. Jensen and O. V. Nielsen, “The magnetic structure of mn_3o_4 hausmannite between 4.7k and neel point, 41k,” *Journal of Physics C: Solid State Physics*, vol. 7, no. 2, p. 409, 1974.

[37] M. Kim. private communication, 2011.

[38] E. Pollert, "Tetragonal-to-cubic transformation of hausmannite," *Journal of Solid State Chemistry France*, vol. 33, pp. 305–308, July 1980.

[39] S.-H. Lee, H. Takagi, D. Louca, M. Matsuda, S. Ji, H. Ueda, Y. Ueda, T. Katsufuji, J.-H. Chung, S. Park, S.-W. Cheong, and C. Broholm, "Frustrated Magnetism and Cooperative Phase Transitions in Spinels," *JOURNAL OF THE PHYSICAL SOCIETY OF JAPAN*, vol. 79, JAN 2010.

[40] S. Lee and L. Balents, "Theory of the ordered phase in a-site antiferromagnetic spinels," *Phys. Rev. B*, vol. 78, p. 144417, Oct 2008.

[41] J.-H. Chung, J.-H. Kim, S.-H. Lee, T. J. Sato, T. Suzuki, M. Katsumura, and T. Katsufuji, "Magnetic excitations and orbital physics in the ferrimagnetic spinels $\mathrm{Mn}B_2o_4$ $(b = \mathrm{Mn}, \mathrm{V})$," *Phys. Rev. B*, vol. 77, p. 054412, Feb 2008.

[42] B. Chardon and F. Vigneron, "Mn3o4 commensurate and incommensurate magnetic structures," *Journal of Magnetism and Magnetic Materials*, vol. 58, no. 12, pp. 128 – 134, 1986.

[43] E. POLLERT, "TETRAGONAL-TO-CUBIC TRANSFORMATION OF HAUSMANNITE," *JOURNAL OF SOLID STATE CHEMISTRY*, vol. 33, no. 3, pp. 305–308, 1980.

[44] U. Hartmann, "Magnetic force microscopy," *ANNUAL REVIEW OF MATERIALS SCIENCE*, vol. 29, pp. 53–87, 1999.

[45] M. Jose Martinez-Perez, J. Sese, F. Luis, R. Cordoba, D. Drung, T. Schurig, E. Bellido, R. de Miguel, C. Gomez-Moreno, A. Lostao, and D. Ruiz-Molina, "Ultrasensitive Broad Band SQUID Microsusceptometer for Magnetic Measurements at Very Low Temperatures," *IEEE TRANSACTIONS ON APPLIED SUPERCONDUCTIVITY*, vol. 21, pp. 345–348, JUN 2011.

[46] A. Masseboeuf, C. Gatel, P. Bayle-Guillemaud, A. Marty, and J.-C. Toussaint, "Lorentz microscopy mapping for domain wall structure study in L1(0) FePd thin films," *ULTRAMICROSCOPY*, vol. 110, pp. 20–25, DEC 2009.

[47] V. V. Khotkevych, M. V. Milosevic, and S. J. Bending, "A scanning Hall probe microscope for high resolution magnetic imaging down to 300 mK," *REVIEW OF SCIENTIFIC INSTRUMENTS*, vol. 79, DEC 2008.

[48] M. Takezawa, "Magnetic Domain Observation and Magnetization Process Analysis of Nd-Fe-B Sub-Micron Grain Sized Magnet with High-Resolution Kerr Microscope," *JOURNAL OF THE JAPAN INSTITUTE OF METALS*, vol. 76, pp. 48–51, JAN 2012.

[49] V. Castel, J. Ben Youssef, F. Boust, R. Weil, B. Pigeau, G. de Loubens, V. V. Naletov, O. Klein, and N. Vukadinovic, "Perpendicular ferromagnetic resonance in soft cylindrical elements: Vortex and saturated states," *Phys. Rev. B*, vol. 85, p. 184419, May 2012.

[50] S. Tanaka, Y. Azuma, and Y. Majima, "Secondary resonance magnetic force microscopy," *Journal of Applied Physics*, vol. 111, no. 8, p. 084312, 2012.

[51] D. Rugar and P. Hansma, "Atomic force microscopy. (cover story).," *Physics Today*, vol. 43, no. 10, p. 23, 1990.

[52] G. Binnig, C. F. Quate, and C. Gerber, "Atomic force microscope," *Phys. Rev. Lett.*, vol. 56, pp. 930–933, Mar 1986.

[53] Y. MARTIN and H. WICKRAMASINGHE, "Magnetic imaging by force microscopy with 1000-a resolution," *APPLIED PHYSICS LETTERS*, vol. 50, pp. 1455–1457, MAY 18 1987.

[54] H.-J. Butt, B. Cappella, and M. Kappl, "Force measurements with the atomic force microscope: Technique, interpretation and applications," *Surface Science Reports*, vol. 59, pp. 1–152, Oct. 2005.

[55] L. N. Kantorovich, A. I. Livshits, and M. Stoneham, "Electrostatic energy calculation for the interpretation of scanning probe microscopy experiments," *Journal of Physics: Condensed Matter*, vol. 12, no. 6, p. 795, 2000.

[56] U. Mohideen and A. Roy, "Precision measurement of the casimir force from 0.1 to 0.9um," *Phys. Rev. Lett.*, vol. 81, pp. 4549–4552, Nov 1998.

[57] A. GRUVERMAN, O. KOLOSOV, J. HATANO, K. TAKAHASHI, and H. TOKUMOTO, "Domain-structure and polarization reversal in ferroelectrics studied by atomic-force microscopy," *JOURNAL OF VACUUM SCIENCE & TECHNOLOGY B*, vol. 13, pp. 1095–1099, MAY-JUN 1995. 3rd International Conference on Nanometer-Scale Science and Technology, DENVER, CO, OCT 24-28, 1994.

[58] J. A. Sidles, "Noninductive detection of single-proton magnetic resonance," *Applied Physics Letters*, vol. 58, no. 24, pp. 2854–2856, 1991.

[59] D. Rugar, R. Budakian, H. Mamin, and B. Chui, "Single spin detection by magnetic resonance force microscopy," *NATURE*, vol. 430, pp. 329–332, JUL 15 2004.

[60] R. SMITH and F. WELSH, "Temperature dependence of elastic, piezoelectric, and dielectric constants of lithium tantalate and lithium niobate," *JOURNAL OF APPLIED PHYSICS*, vol. 42, no. 6, pp. 2219–&, 1971.

[61] T. ALBRECHT, P. GRUTTER, D. HORNE, and D. RUGAR, "Frequency-modulation detection using high-q cantilevers for enhanced force microscope sensitivity," *JOURNAL OF APPLIED PHYSICS*, vol. 69, pp. 668–673, JAN 15 1991.

[62] R. W. Stark, T. Drobek, and W. M. Heckl, "Thermomechanical noise of a free v-shaped cantilever for atomic-force microscopy," *Ultramicroscopy*, vol. 86, no. 12, pp. 207 – 215, 2001.

[63] D. Sarid, *Scanning Force Microscopy: With Applications to Electric, Magnetic, and Atomic Forces*. Oxford series on optical sciences, Oxford University Press, 1994.

[64] T. Fukuma, M. Kimura, K. Kobayashi, K. Matsushige, and H. Yamada, "Development of low noise cantilever deflection sensor for multienvironment frequency-modulation atomic force microscopy," *REVIEW OF SCIENTIFIC INSTRUMENTS*, vol. 76, MAY 2005.

[65] J. SANTOS, A. LEITE, and D. JACKSON, "OPTICAL FIBER SENSING WITH A LOW-FINESSE FABRY-PEROT CAVITY," *APPLIED OPTICS*, vol. 31, pp. 7361–7366, DEC 1 1992.

[66] R. Shotwell, *An introduction to fiber optics*. Prentice Hall, 1997.

[67] E. R. Abraham and E. A. Cornell, "Teflon feedthrough for coupling optical fibers into ultrahigh vacuum systems," *Appl. Opt.*, vol. 37, pp. 1762–1763, Apr 1998.

[68] E. Volterra and E. Zachmanoglou, *Dynamics of vibrations*. No. v. 1 in Dynamics of Vibrations, C.E. Merrill Books, 1965.

[69] U. Durig, H. R. Steinauer, and N. Blanc, "Dynamic force microscopy by means of the phase-controlled oscillator method," *Journal of Applied Physics*, vol. 82, no. 8, pp. 3641–3651, 1997.

[70] U. Dürig, J. K. Gimzewski, and D. W. Pohl, "Experimental observation of forces acting during scanning tunneling microscopy," *Phys. Rev. Lett.*, vol. 57, pp. 2403–2406, Nov 1986.

[71] J. Mertz, O. Marti, and J. Mlynek, "Regulation of a microcantilever response by force feedback," *Applied Physics Letters*, vol. 62, no. 19, pp. 2344–2346, 1993.

[72] J. L. Garbini, K. J. Bruland, W. M. Dougherty, and J. A. Sidles, "Optimal control of force microscope cantilevers. i. controller design," *Journal of Applied Physics*, vol. 80, no. 4, pp. 1951–1958, 1996.

[73] U. HARTMANN, "FUNDAMENTALS AND SPECIAL APPLICATIONS OF NON-CONTACT SCANNING FORCE MICROSCOPY," in *ADVANCES IN ELECTRONICS AND ELECTRON PHYSICS, VOL 87* (Hawkes, PW, ed.), vol. 87 of *ADVANCES IN ELECTRONINCS AND ELECTRON PHYSICS*, pp. 49–200, 1994.

[74] D. Rugar, H. J. Mamin, P. Guethner, S. E. Lambert, J. E. Stern, I. McFadyen, and T. Yogi, "Magnetic force microscopy: General principles and application to longitudinal recording media," *Journal of Applied Physics*, vol. 68, no. 3, pp. 1169–1183, 1990.

[75] A. Moser, M. Xiao, P. Kappenberger, K. Takano, W. Weresin, Y. Ikeda, H. Do, and H. Hug, “High-resolution magnetic force microscopy study of high-density transitions in perpendicular recording media,” *Journal of Magnetism and Magnetic Materials*, vol. 287, no. 0, pp. 298 – 302, 2005.

[76] D. Ovchinnikov and A. Bukharaev, “Computer simulation of magnetic force microscopy images with a static model of magnetization distribution and dipole-dipole interaction,” *TECHNICAL PHYSICS*, vol. 46, no. 8, pp. 1014–1019, 2001.

[77] F. Humphreys, “Review - Grain and subgrain characterisation by electron backscatter diffraction,” *JOURNAL OF MATERIALS SCIENCE*, vol. 36, pp. 3833–3854, AUG 2001.

[78] D. Prior, A. Boyle, F. Brenker, M. Cheadle, A. Day, G. Lopez, L. Peruzzo, G. Potts, S. Reddy, R. Spiess, N. Timms, P. Trimby, J. Wheeler, and L. Zetterstrom, “The application of electron backscatter diffraction and orientation contrast imaging in the SEM to textural problems in rocks,” *AMERICAN MINERALOGIST*, vol. 84, pp. 1741–1759, NOV-DEC 1999.

[79] S. Kikuchi, “Diffraction of cathode rays by mica,” *Japan J. Phys.*, vol. 5, pp. 83–96, 1928.

[80] S. H. Curnoe and A. E. Jacobs, “Time evolution of tetragonal-orthorhombic ferroelastics,” *Phys. Rev. B*, vol. 64, p. 064101, Jul 2001.

[81] M. A. Tanatar, A. Kreyssig, S. Nandi, N. Ni, S. L. Bud’ko, P. C. Canfield, A. I. Goldman, and R. Prozorov, “Direct imaging of the structural domains in the iron pnictides afe$_2$as$_2$ (a=ca,sr,ba),” *Phys. Rev. B*, vol. 79, p. 180508, May 2009.

[82] C. Ma, H. X. Yang, H. F. Tian, H. L. Shi, J. B. Lu, Z. W. Wang, L. J. Zeng, G. F. Chen, N. L. Wang, and J. Q. Li, “Microstructure and tetragonal-to-orthorhombic phase transition of afe$_2$as$_2$ (a=sr, ca) as seen via transmission electron microscopy,” *Phys. Rev. B*, vol. 79, p. 060506, Feb 2009.

[83] E. Salje, A. Buckley, G. Van Tendeloo, Y. Ishibashi, and G. Nord, “Needle twins and right-angled twins in minerals: Comparison between experiment and theory,” *AMERICAN MINERALOGIST*, vol. 83, pp. 811–822, JUL-AUG 1998.

[84] A. Lavrov, S. Komiya, and Y. Ando, “Magnetic shape-memory effects in a crystal (vol 418, pg 385, 2002),” *NATURE*, vol. 421, p. 230, JAN 16 2003.

[85] A. Saxena, T. Castán, A. Planes, M. Porta, Y. Kishi, T. A. Lograsso, D. Viehland, M. Wuttig, and M. De Graef, “Origin of magnetic and magnetoelastic tweedlike precursor modulations in ferroic materials,” *Phys. Rev. Lett.*, vol. 92, p. 197203, May 2004.

[86] J. Sapriel, “Domain-wall orientations in ferroelastics,” *Phys. Rev. B*, vol. 12, pp. 5128–5140, Dec 1975.

[87] M. T. Dove, A. P. Giddy, and V. Heine, "On the application of mean-field and landau theory to displacive phase transitions," *Ferroelectrics*, vol. 136, no. 1, pp. 33–49, 1992.

[88] A. M. Bratkovsky, E. K. H. Salje, and V. Heine, "Overview of the origin of tweed texture," *Phase Transitions*, vol. 52, no. 2-3, pp. 77–83, 1994.

[89] A. BRATKOVSKY, E. SALJE, S. MARAIS, and V. HEINE, "THEORY AND COMPUTER-SIMULATION OF TWEED TEXTURE," *PHASE TRANSITIONS*, vol. 48, no. 1-3, Part b, pp. 1–13, 1994.

[90] A. M. Bratkovsky, S. C. Marais, V. Heine, and E. K. H. Salje, "The theory of fluctuations and texture embryos in structural phase transitions mediated by strain," *Journal of Physics: Condensed Matter*, vol. 6, no. 20, p. 3679, 1994.

[91] A. M. Bratkovsky, E. K. Salje, S. C. Marais, and V. Heine, "Strain coupling as the dominant interaction in structural phase transitions," *Phase Transitions*, vol. 55, no. 1-4, pp. 79–126, 1995.

[92] A. E. Jacobs, "Landau theory of a constrained ferroelastic in two dimensions," *Phys. Rev. B*, vol. 52, pp. 6327–6331, Sep 1995.

[93] A. E. Jacobs, "Landau theory of structures in tetragonal-orthorhombic ferroelastics," *Phys. Rev. B*, vol. 61, pp. 6587–6595, Mar 2000.

[94] G. R. Barsch and J. A. Krumhansl, "Twin boundaries in ferroelastic media without interface dislocations," *Phys. Rev. Lett.*, vol. 53, pp. 1069–1072, Sep 1984.

[95] A. E. Jacobs, "Finite-strain solitons of a ferroelastic transformation in two dimensions," *Phys. Rev. B*, vol. 46, pp. 8080–8088, Oct 1992.

[96] M. A. Ivanov, N. K. Tkachev, and A. Y. Fishman, "Phase transformations of the decomposition type in systems with orbital degeneracy," *Low Temperature Physics*, vol. 28, no. 8, pp. 613–620, 2002.

[97] Y. Huang, Z. Qu, and Y. Zhang, "The micromagnetic study of the vanadate spinel mnv_2o_4," *Journal of Magnetism and Magnetic Materials*, vol. 323, pp. 970–974, Apr. 2011.